Quantum measurement and bath engineering for superconducting qubits via multiple parametric couplings

by

Xi Cao

Bachelor of Science, Wuhan University, 2014

Submitted to the Graduate Faculty of

the Dietrich School of Arts and Sciences in partial fulfillment

of the requirements for the degree of

Doctor of Philosophy

University of Pittsburgh

2021

UNIVERSITY OF PITTSBURGH

DIETRICH SCHOOL OF ARTS AND SCIENCES

This dissertation was presented

by

Xi Cao

It was defended on

February 11, 2021

and approved by

Michael Hatridge, Department of Physics and Astronomy, University of Pittsburgh

David Pekker, Department of Physics and Astronomy, University of Pittsburgh

Sergey Frolov, Department of Physics and Astronomy, University of Pittsburgh

Ayres Freitas, Department of Physics and Astronomy, University of Pittsburgh

Daniel Lambrecht, Department of Chemistry and Physics, Florida Gulf Coast University

Dissertation Director: Michael Hatridge, Department of Physics and Astronomy, University of Pittsburgh

Quantum measurement and bath engineering for superconducting qubits via multiple parametric couplings

Xi Cao, PhD

University of Pittsburgh, 2021

Quantum computers have huge potential applications, but do not currently exist. It has already been proven that a quantum computer would outperform the best classical supercomputers in certain problems, some of which have vital connections with our daily lives. For example, quantum computers efficiently solve the prime number factoring problem, which in turn is the foundation of the RSA algorithm behind most online transactions. There is a great deal of current effort to implement quantum computers, and we have seen good progress in platforms including superconducting circuits, ion traps, and photons in cavity QED systems and spins in semiconductors. These machines include up to roughly 50 quantum bits at present, but they are not very useful as quantum errors quickly decohere the computer's state and prevent computation. These errors can be mitigated via quantum error correction at the cost of additional size and complexity.

Progress in the field towards error corrected, large-scale quantum machines requires us to require new tools for controlling, coupling, and reading out qubits. In this thesis, I will focus on such explorations in superconducting circuits. In this thesis, we seek to expand the already flexible toolkit of quantum circuits by exploring the uses of parametric couplings based on third-order nonlinearities. This type of nonlinearities has only been used in quantum-limited amplifiers before, here we try to further explore their applications by creating new methods for controlling and measuring qubits that based on it.

In the first experiment, we address the problem of implementing a highly efficient quantum non-demolition qubit readout. With the use of two-mode squeezed (TMS) light and combined with phase-preserving parametric amplifiers into an interferometer for dispersive qubit readout, we demonstrate a measurement scheme with a 44% improvement in power signal-to-noise ratio. We also investigate the back-action of the measurement scheme.

In the second experiment, we create an effective chemical potential for photons with parametric system-bath coupling. In particular, we use a lossy Superconducting Nonlinear

Asymmetric Inductive eLement (SNAIL) as both the bath and coupler. The bath engineering is realized by combining the multiple parametric drives and the dissipation together.

Table of contents

List of figures

Acknowledgements

At this finishing stage of my Ph.D, I want to take the opportunity to thank all the people who helped me along the road. I would like to begin by thanking my advisor, Prof. Michael Hatridge for both for the chance to work in his group, and for all that he has taught me. Michael is always enthusiastic and dedicated in both research and educating his students. Under Michael's supervision , I have learned so much about how to not only analyze problems and perform experiments but also how to communicate and practice science.

I would also like to thank my committee members, Sergey Frolov, David Pekker, Ayres Freitas and Daniel Lambrecht for all of the help and support over the years, and for being willing to read my thesis. Especially Prof. Frolov, all those extensive comments are really helpful to me. I also want to thank Nick Bronn for being a wonderful mentor during my internship at IBM. It was a great experience for me to learn how the industry in this field works.

For most of my Ph.D, I had the auspicious opportunity to work with three people: Gangqiang Liu, Tzu-Chiao Chien and Olivia Lanes. Thank you for always being patient with my questions. Gang, I learnt lots of useful experiment tricks from you and I could always receive precious advice from you both about science and life. Tzu-Chiao, thank you for teaching me all the fab tricks and always be there whenever I need your help. Most importantly, thanks for teaching me how to drive, a skill that makes my life here at U.S much better. Olivia, for showing me so much American culture and drawing most of Michael's attention during the lunch.

To Chao Zhou and Maria Mucci, it is always nice to talk to you guys about science and my chemical potential project could never work withou your help. To Ryan Kaufman, Param Patel and Mingkang Xia, for being responsible and helpful when I need extra hands and willing to discussing science with me.

I am also fortunate to have plenty of great friends that have also helped me along the way. Jun Chen and Azarin Zarassi taught me plenty of fabrication tricks. Chenxu Liu patiently taught me many theoretical tricks. Erick Brindock gave me a lot of coding knowledge and helped me get the frist car in my life. Edan Alpern and Sarah Motz are cheerful all the time

and bring joy to the lab. Especially for Edan, that Thanksgiving dinner I had with your family will also be an unforgettable memory for me. Kang Huang, Rui Wen and Wenyuan Liu, thanks for all those happy time on weekends. Although I really hope we can at least finish one good Civilization game with a better internet connection. Of course, I will never forget the delicious we had at Hatridge family from Cate. Also, my buddy Hank, your occasional presence in the lab can always make my day.

I am also thankful to my family, especially my parents and my girl friend Liya Zhu. You are always there with me when I am sad and desperate, offering my emotional support. Without you, I can never reach this finishing line of the PhD.

I. Introduction

A. Background of quantum computation

Quantum mechanics has been a vital branch of modern physics since the early 1900s. It is both essential to explaining fundamental concepts such as structure of atoms, and underlies much of modern technology including such daily-use objects as lasers and transistors. However, the idea to use quantum mechanics as a basis for computation did not receive much attention until Feynman proposed the concept of simulating physics problems with a quantum computer [1] in the early 1980s. He argued that by taking advantage of the unique properties of quantum systems, a new type of computer could be developed, which will be fundamentally different than the Turing machines described by classical computation science. This new 'quantum computer' would provide a possibly more efficient way of tackling problems involving simulations of quantum mechanics, as it integrates the complicated calculations into the intrinsic evolution of a quantum system: the answer is naturally developed rather than explicitly calculated. More precisely speaking, in a quantum simulator, we can create a realization of the specific systems of interest that allows us to observe the system's properties rather than numerically solving Schrodinger's equation directly, which can be difficult for classical computers when the problem Hilbert space is large.

Not long after Feynman's proposal, the concept of the Quantum Turing machine was developed by Deutsch [2]. By the end of the century, algorithms that demonstrate 'quantum speed up' in searches of databases by Grover [3] and integer factorization by Shor [4] were developed. This latter algorithm continues to drive much of the interest in quantum computation, as the exponential speed-up in Shor's algorithm diminishes the reliability of the RSA cryptosystem, on which the security of almost every online transaction is based.

A few decades ago, we began to see the first examples of qubit-like quantum behavior in various platforms, including nuclear spins [5], ion traps [6], photons in cavity QED systems [7] and superconducting circuits [8]. The field of quantum computation is currently undergoing a phase of rapid growth, with a recent National Quantum Initiative injecting $\sim$

one billion dollars into research in this area in the U.S. More, we are also seeing a transformation from a long-range vision and challenge led primarily by academic researchers to a potentially realizable (but still very challenging) disruptive technology being actively developed by industrial researchers at established companies like Google, IBM, Honeywell, Intel (and others) and startups such as IonQ, Quantum Circuits, and many more.

One important goal for the field of quantum computation is to realize a physical device that solves *useful* problems that a classical computer is not able to solve in a reasonable time, that is, to demonstrate a 'quantum advantage'. Although recent results from Google [9] seems to show the quantum advantage in a random quantum circuits sampling problem, there is still a long way to go before the realization of a universal quantum computer that can implement various algorithms. Different experimental platforms, such as spins in semiconductors [10, 11], trapped ions [12–14], photonic system [15, 16] and superconducting circuits [17, 18] have shown their potential as candidates for future quantum computers. Despite this progress, the presence of noise and decoherence still prevents the realization of a practical large-scale quantum machine. Theories to create quantum computers which function even in the presence of errors, namely quantum error correction and fault-tolerant quantum computation, have been developed to address this issue. However, these techniques still seem to be some distance away from practical implementation, thus people believe it would be realistic to implement Noisy Intermediate-Scale Quantum (NISQ) technology in the near future [19]. Here, noisy indicates the existence of noise in the system and also that qubit gate control is not perfect, which will put a limitation on the performance of the device. Intermediate-scale refers to a quantum machines with at least $50 \sim 100$ qubits. Such machines will not be able to be simulated with current classical supercomputers by brute force, and have already been built by researchers from Google and IBM [9,20],but are not big enough to perform truly useful computations, such as factoring large numbers. Although it is not the ultimate form of a quantum computer, NISQ technology will bring us new insights about large-scale quantum machines and can also be used as a tool for exploring the physics of many entangled particles. Given the rapid development of the field, we remain optimistic and hope for practical applications of a quantum computer in our lifetimes that will assist in the discovery of new materials and medicines.

Our lab, and thus this thesis, is focusing on the superconducting Josephson-junction based quantum circuits, which have been rapidly improving in terms of vital benchmarks such as qubit lifetime, gate and readout fidelity in the recent years, making it one of the leading platforms for implementing quantum computers. However, despite these promising developments, there is still a long way to go before we see a useful universal quantum computer. To bring us to next stage, both the technical improvements and new understanding of physics are in need. A mixture of these two has been the focus of this PhD, building parts that can be used as a component of the future quantum computer but also tools that help people to explore exciting new physics.

B. History and challenges for superconducting quantum computation

The main feature that makes the quantum computer different than a classical one is how it stores and manipulates data. The basic element that handles the information in a quantum computer is the qubit.There are two major differences between a qubit and classical bit: superposition and entanglement. These are the sources of the computational power for a quantum computer.

Superposition is a counter intuitive property from a classical point of view. A classical bit which can only be in the state of 0 or 1, while a qubit can simultaneously exist in a configuration that has multiple states. In other words, it can be both the state of 0 and 1, or, more precisely, any possible state in the linear space generated by coherent combinations of states $|0\rangle$ and $|1\rangle$. (here $|\ \rangle$ is the Dirac notation to represent a quantum state). Although the state can remain in such a superposition state during computation, a measurement will destroy this superposition and collapse the superposition onto the basis states with a probability given by the amplitude of the coefficients in the superposition, squared. While it is not obvious from the single qubit example, one of the most important features of quantum states is that the number of states the system can assume grows exponentially (as 2^N, where N is the number of qubits). Thus, a system with 50 qubits can be in a coherent superposition of $2^{50} = 1125899906842624$ states, each described by an $analog, continuous, complex$ number.

This huge amount of data must be tracked, which even for a modest quantum system (or computer) is why simulating quantum mechanics on digital classical computers is so very hard and inefficient.

Quantum entanglement is a physical state involving a pair or a group of states in which the state of single qubit cannot be described independently without referring to other qubits. A measurement of one qubit will simultaneously collapse other qubits to a state determined by the correlation relation given by the nature of the states' entanglement. Take a Bell state $|\psi\rangle = (|00\rangle + |11\rangle)/\sqrt{2}$ as an example. If we only measure one of the qubits of a Bell pair, say the first qubit, then we will get an equal distribution between the $|0\rangle$ and $|1\rangle$ state, that is, 50% percent of the time we get $|0\rangle$ and 50% percent of the time we get $|1\rangle$ with a random outcome of $|0\rangle$ and $|1\rangle$ on each particular measurement. However, if we try to measure both of the qubits at the same time and look at the correlation between the two measurement outcomes, we find that we will always get the same result. The measurement results of the states of the two qubits are tightly correlated. That is, if the first qubit is in the $|0\rangle$ state, then we will automatically know the state of the second qubit is also $|0\rangle$ (and vice versa), no matter how far away they are apart from each other. This property of an entangled state, which was called 'spooky' by Einstein, has been proven in experiment [21]. Note that each qubit examined alone looks random, but pairs of answers for measurement of both qubits are perfectly correlated *in certain bases*. In a quantum algorithm, we manipulate the qubits with carefully designed quantum operations that enhance the probability of the correct solution state while suppress the probability of other states. Then, by applying a measurement at the end of the computation, the chance of getting the right answer is maximized.

In this thesis, we will focus on the superconducting qubits. The superconducting qubit is made of superconducting circuits consist of inductors, capacitors and Josephson junctions. A simple L-C circuit can form a harmonic oscillator, but it will not be sufficient to be used as a qubit, as its energy levels are equally spaced, no individual transitions can be independently addressed to form the computational basis for quantum algorithms. Therefore, certain non-linearity needs to be introduced in a superconducting circuits, which is implemented with the help of Josephson junctions (See Ch. II for detailed discussion). The first demonstration of the superconducting qubit in 1999 [8] with coherent times on the order of about 1 ns. This

is a perfect prove of concept result for showing the existence of such qubit but it is still far from enought to be used for any practical quantum algorithms. Since then, various designs of the superconducting qubit have been proposed and realized in different groups across the world, such as: transmon qubit [22–24], phase qubit [25, 26], flux qubit [27, 28], fluxonium qubit [29, 30], $0 - \pi$ qubit [31]. With these efforts, we have seen qubits with coherent time that is close to the order of ms recently [32], which means a factor of almost one million improvement in just two decades.

Currently, lost of the researches, and my PhD also, are focusing on the transmon qubit in the so-called circuit Quantum ElectroDynamics (cQED) architecture [33]. Similar to the field of cavity Quantum ElectroDynamics (cavity QED), this architecture provides a frame for people to study the interaction between the artificial atoms (superconducting qubits) and microwave light. In contrast to cavity QED, in cQED the atoms and light can have a larger coupling strength between them, which makes it easier to engineer the system Hamiltonian. Within this frame, the single-qubit gates are implemented by sending microwave drives to the system. And with the help of the Derivative Removal by Adiabatic Gate (DRAG) technique [34], now the single qubit gate can be implemented with fidelity ≥ 0.999 [24,35,36]. As for two-qubit gates, there are three different ways of realizing them. The first is to use frequency tunable transmon qubits and move the qubits onto resonance when applying the gate, and we have seen high fidelity two-qubit gates from this scheme [24]. The second idea is to use fixed frequency qubits and control them with microwave drives, typically driving one qubit at the frequency of the other to implement a high-fidelity two-qubit gate. This method is also known as s 'cross resonance gate' [37]. The third idea is to drive a coupling element (or sometimes the qubit itself) between the two qubits to create a parametric coupling between the qubits to realize a two-qubit gate [38].

Much recent effort towards large-scale machines focuses along three lines: improving the coherence, optimizing qubit readout and to scaling up system size. To demonstrate the power of quantum algorithms over their classical counterparts requires a large enough quantum system that connects multiple qubits (preferably in a readily scalable manner, so that the device can be easily extended to potentially address harder problems) while being able to manipulate and maintain coherence and entanglement. We must also be

able to initialize a known initial state of the computer, and read out each qubit with high fidelity. These requirements are summarized as DiVincenzo's criteria [39]. The coherence times of qubits suffer from the non-zero connection between the qubit and external noise in the surrounding environment. Progress has been made to improve the coherence of qubits with better circuit designs that suppress the sensitivity to noise [22, 29, 40], better filtering on wiring that removes fluctuations in the environment seen by the qubit [41], and better fabrication processes that reduce the internal loss of the qubit [32].

However, despite the efforts mentioned above, there is always a trade-off between maximizing a qubit's coherence and isolating it from environmental noise, as a perfectly isolated qubit is no longer able to be manipulated and measured. This conflict represents an ongoing challenge for the foreseeable future, that is, to build a quantum computer with necessarily flawed components. Some sort of quantum error correction (QEC) which can largely suppress the error rates is required. The first QEC scheme was proposed by Shor in 1995 [42] where he showed how the information can be protected by encoding the state of one qubit into an entanglement of nine qubits in a decoherence-resistant way. This result demonstrates the basic idea of QEC: to assemble several noisy qubits into one logical qubit in a larger Hilbert space and make it less vulnerable to errors. We have seen several plans of QEC based on the extension of this idea [43–45]. Recently a different class of schemes based on superconducting circuits has been put forward which have approached or slightly exceeded the break-even point [46–48], breaking even meaning the schemes corrected at least as many errors as the additional hardware and control overhead created.

Although progress in QEC is promising, we also note that there are other types of errors that any particular QEC code cannot address, such as the state preparation and measurement errors, a qubit leaving the computational manifold as its physical implementation is not strictly a two-level system, or two- and multi-qubit errors. The method to protect the quantum information against these errors involves the concept of fault-tolerant quantum computation (FTQC). The first step of FTQC is to operate the logical qubit with fault-tolerant operations which are designed such that a failure of a single qubit will only result in a correctable error on the system. Then, another layer of QEC will be applied to these logical qubits and fault-tolerant operations. If the error rate of this process is below some threshold

value, then a concatenation of multiple levels of the same process will lead to better and better results [49].

QEC and FTQC require both advances in engineering and in further understanding of the underlying coherent and incoherent physical processes in our quantum computers. Two such explorations to expand our ability to understand and control quantum circuits are at the heart of my thesis. In Ch. III, we introduce a new qubit measurement scheme using two-mode squeezed light. In the scheme, we work on demonstrating a new measurement technique that shows a high measurement fidelity and investigating a physics behind quantum measurement using entangled quantum light. In Ch. IV and Ch. VI, we realize a controllable bath for a transmon qubit with the bath engineering technique. In this project, we create a chemical potential for a photonic system, which does not exist in a natural setting. It can be used as a tool for discovery by coupling it to other systems.

C. Quantum measurement and two-mode squeezed qubit readout

A qubit-specific measurement capability is one of the Divincenzo's criteria and also one of the research fronts for superconducting computation. Originally, DiVincenzo did not require this measurement to be quantum non-demolition (QND) [50], imagining measurement as only taking place after the computation has ended. A QND measurement is the type of measurement of a quantum system that the measurement itself will not destroy the state of the qubit and thus a consecutive measurement will always yield the same result as the previous one. High fidelity QND measurements, which project the qubit into an eigenstate of the measurement operation (which is also accurately reported to the experimenter controlling the system) is vital in QEC codes based on real time feedback.

A commonly used measurement method in superconducting circuits is the dispersive measurement as shown in Fig. 1. A qubit is dispersively coupled to a microwave cavity (see Ch. II for details), such that the frequency of the cavity will have a qubit-state-dependent shift. Therefore, the state of the qubit can be inferred by measuring the frequency of the cavity as shown in Fig. 1(a). As in this measurement scheme the probe signal does not interact

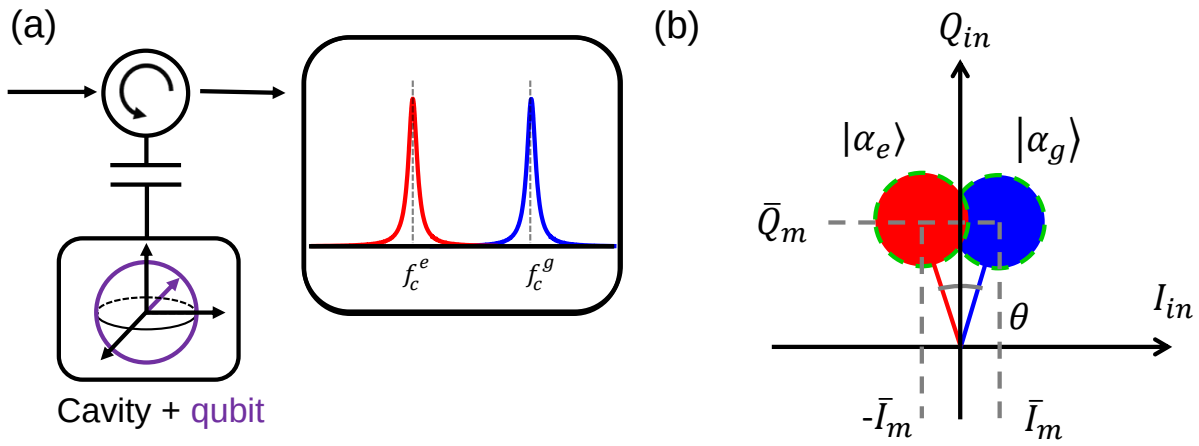

Figure 1: **Dispersive measurement.** (a) A system consists of a two-level quantum system (qubit) placed in a microwave cavity. The qubit and cavity are dispersively coupled to each other. The frequency of the cavity will thus get a qubit-state dependent shift. This shift can be measured via a phase shift of a coherent light that reflects on the cavity. (b) The coherent light can be visualized in the phase space. It is represented as a 2D Gaussian distribution with a standard deviation $\sigma_I = \sigma_Q = 1/2$ and a displacement from the origin set by the average number of photon in the pulse. Both $|g\rangle$ and $|e\rangle$ give similar result, only with a phase difference determined by the dispersive shift.

directly with the qubit, it is also known for its QND nature, in contrast to destructive measurement, for example [51]. The most commonly used probe light in superconducting qubit measurement is the coherent state of microwave light. Coherent states are the eigenstate of the annihilation operator [52]. Although counterintuitive, this definition gives a quantum state which is the direct analog of the state of a driven, dampged classical oscillator. Coherent states can be visualized in phase space, which plots the in-phase (I) and quadrature (Q) components of the propagating light . A typical result of dispersive measurement with coherent light is shown in Fig. 1(b). In phase space, a coherent state is represented by a 2D-Gaussian distribution with standard deviation $\sigma_I = \sigma_Q = 1/2$. The I and Q components do not commute (just as momentum and position do not commute for a physical pendulum),

and so cannot be precisely measured at the same time due to the uncertainty principle.

We will get a similar result (a 2D Guassian distribution) for qubit in $|g\rangle$ and $|e\rangle$, which corresponds to 0 and 1 microwave photon number in the circuit (it is the same as the $|0\rangle$ and $|1\rangle$ but a more commonly used language for experimentalists), only with a phase difference θ that comes from the frequency shift due the dispersive coupling. The distance between the center of the two distributions versus their widths sets the measurement strength. The state of a qubit can be determined from an individual measurement result (I_m, Q_m) by looking at which distribution the point falls into. A measurement error happens when a $|g\rangle$ state result is recognized as an $|e\rangle$ state (and vice versa). This is most likely to happen in the area where the two distributions overlap. In order to increase the fidelity of a measurement (at least for the Z-projective measurement), we need to separate the two distributions for the $|g\rangle$ and $|e\rangle$ states, or in other words, increase the measurement strength, or the signal-to-noise ratio (SNR) of the measurement. The SNR is defined as the ratio between the separation of the distributions over their deviation: $\frac{(I_c^g-I_c^e)^2+(Q_c^g-Q_c^e)^2}{\sigma_g^2+\sigma_e^2}$. In experiments, a quantum limited amplifier is also needed to overwhelm the noise from the latter parts of the measurement chain so that we can perform a good single shot readout of the qubit state at room temperature. Typically, there are two types of quantum limited amplifiers. For a phase preserving amplifier, both quadratures of the incoming microwave signal are amplified, with a half-photon 'noise' added to the signal [53], which will in principle decrease the SNR of the measurement, but we can learn (albeit imperfectly) the information present in both quadratures. For a phase sensitive amplifier, we 'squeeze' away one quadrature to learn the information with perfectly the information in the other quadrature. The price we pay in this mode of operation is that all the information in the quadrature that is squeezed away (and no longer accessible to any observer).

There is another side to look at these quantum limited amplifiers. As they are all quantum devices, it is worth studying what kind of quantum light they produce. When there is no amplification/squeezing involved, the input and output states are both coherent light. And as we mentioned above, coherent light forms a 2D Gaussian distribution in phase-space. The finite radius of the distribution comes from the uncertainty principle from the quantum mechanics as shown in Fig. 2(a). Coherent states have the same uncertainty for

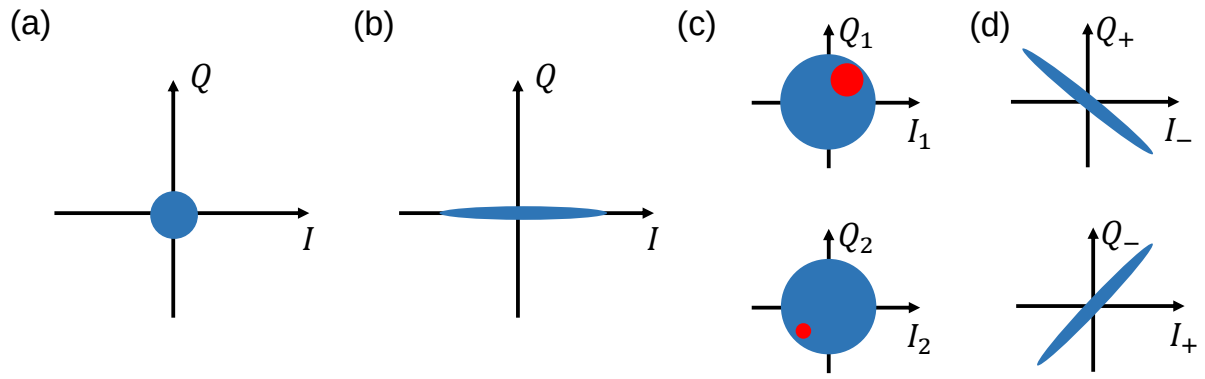

Figure 2: **Schematics of squeezing states.** (a) Phase space representation of a (coherent) vacuum state. The radius of the distribution corresponds to a half-photon noise, which comes from the Heisenberg uncertainty principle. (b) Phase space representation of a single mode squeezed vacuum. The fluctuation on one quadrature is squeezed at the cost of creating more fluctuation on the other. (c) Phase space representation of each mode of a two-mode squeezed vacuum. When measuring independently, each mode behaves as a thermal state with an extra half photon noise added by squeezed state generator (e.g. JPC). (d) The correlation relation between the two modes in a two-mode squeezed vacuum.

both quadratures, so they appear as an isotropic state in phase space. One-mode squeezed states, as shown in Fig. 2(b), will modify this isotropic state by 'squeezing' one quadrature and 'antisqueezing' the other by an equal and opposite amount. This is naturally attached to the act of phase-sensitive amplification that amplifies (anti-squeezes) one quadrature and squeezes away the other. The situation for a phase preserving amplifier is a little more complicated, as it produces 'two-mode squeezed' light. A phase preserving amplifier always has two ports, with each port having reflection gain of its input, and will also receive added noise from the other port. The fact that both of the output signals are related to both of the input signals turns out to be a quantum mechanical requirement from that the output mode should preserve the commutation relation between its two quadratures. This gives the interesting property of two-mode squeezed light: when measured independently, each

mode of a two-mode squeezed vacuum behaves as a thermal state, as shown in Fig. 2(c). The squeezing effect does not show up for each single mode, but instead appears in the correlation relation ($I_\pm = I_1 \pm I_2$ and $Q_\pm = Q_1 \pm Q_2$) between the modes, as shown in Fig. 2(c). (A detailed discuss about how a phase persevering amplifier works can be found in Sec. II.E). This effect of the phase preserving amplifier turns out to the import resource we use in the two-mode squeezed light readout project in Ch. III.

Another important dimension to assess the quality of a measurement is the measurement efficiency. In a QND measurement, the qubit state evolves during the measurement process until it reaches an eigenstate of the measurement operator. The effect that the measurement has on the qubit is known as the back-action of the measurement. For an 'efficient' measurement, the back-action should be perfectly trackable, or in other words, the measurement will have maximum SNR for the amount of light we sent in, provided the 'noise' (deviation of the distribution) is due to inherent quantum fluctuations in the input state and the quantum action of the amplifier [54].

In this picture the 'noise' from these sources is not an actual noise (i.e. something that hides the signal), as we can perfectly learn how the qubit evolves from the measurement result. Instead, these fluctuations are what cause the back-action to be unpredictable in advance (but trackable for a given measurement record). We can the define the efficiency of the measurement:

$$\eta = \frac{\sigma_{Heis}^2}{\sigma_{Heis}^2 + \sigma_{add}^2} \tag{I.1}$$

where $\sigma_{Heis} = 1/2$ comes from the fundamental non-commutativity of the variables I and Q and thus are representative of Heisenberg back-action and σ_{add} is the non-Heisenberg added noise from the measurement chain. Compare to the SNR, the measurement efficiency can better describe the trackability of the qubit state under measurement. This idea that to qualify a measurement by how much we can track the qubit evolution under the measurement process is rather useful in practical experiment, and gives a unity efficiency for the ideal phase-preserving amplifier instead of one-half as in Caves' theorem [53]. There is no contradiction here, as Caves was concerned with tracking the information present in the microwave readout tone, which is obscured by being entangled with the amplifier's added fluctuations. However, we are only interested in knowing the qubit's state, which is influenced by both

noise sources.

In Ch. III, we address this issue of measurement and efficiency for both coherent light and two-mode squeezed light measurement with a study of the back-action of the measurement for each type of microwave light. We demonstrate that using two-mode squeezed light instead of the conventional coherent light can result in a 44% improvement in the power SNR of the measurement.

D. A chemical potential for transmon qubits

The idea of bath engineering is to take advantage of the non-unitary evolution or the dissipation in a system to generate desired quantum coherent states and useful quantum processes. To put it in another way, if you have a target state for your quantum system, or a potential kind of evolution, bath engineering creates a strange 'noise' or 'relaxation' for your system which will push the system to your desired condition. Typically, this could also be done with a coherent quantum drives on the system, but bath engineering has the advantage that it can be 'set and forget' and acts without the need for real-time monitoring and control.

The concept of bath engineering and its application to quantum computation was first formulated in [55,56] and then developed in [57,58]. Since then bath engineering has been an important tool in multiple applications for qubit state preparation/reset [59–61], generation of multi-qubit entangled states [62, 63] and autonomous quantum error correction [64, 65]. Preparing/stabilizing a state using the engineered dissipation has several advantages over conventional methods using measurement and coherent unitary operations. For example, in the case of active measurement based feed back, a decision needs to be made after receiving the result of the measurement which typically takes 0.5 - 1 μs. A dissipation engineering based feedback protocol will thus be simpler and faster and could potentially yield a result with higher fidelity, see [66] for a comparison. In some many-body simulation problems [67–69], bath engineering can prepare and stabilize states which are needed for the project that is difficult to generate using coherent drives.

In Ch. IV and Ch. VI, we implement a bath engineering project for a transmon qubit through a three-wave parametric coupling in the system. The three-wave bath-engineering circuits were realized in two ways: with a Josephson ring modulator and lossy SNAIL-based resonators (see Ch. II). By combining parametric drives and the SNAIL's dissipation, we create a controllable bath for a photonic system with a tunable chemical potential. A photonic system such as the transmon will not have a chemical potential in the natural setting, and thus the results of this project provides an interesting and valuable tool for the investigation of the physics and creation of exotic states, particular in multi-mode simulators [67, 68].

E. Organization of this thesis

This thesis is organized as follows: in Ch. II, we start with the introduction of the tools we need for our experiments. A quick review of superconducting qubits with a focus on the transmon qubit and the dispersive measurement is given in Sec. II.B. Next we discuss the basic idea of parametric couplings in Sec. II.C. As an example of the use of parametric couplings to create amplifiers, we give an introduction to the Josephson parametric converter (JPC) in Sec. II.D and demonstrate how we can use it to generate two-mode squeezed light in Sec. II.E. We also talk about the Superconducting Nonlinear Asymmetric Inductive eLement (SNAIL) device as a dipole element with a third order term and how it could be used in the bath engineering project in Sec. II.F.

In Ch. III, we move to the first experimental project: to demonstrate a new qubit measurement scheme with two-mode squeezed light. We first introduce the setup and the basic parameters for the experiment in Sec. III.B and Sec. III.C. We then demonstrate the interference of the two-mode squeezed light in Sec. III.D and show the noise performance and the SNR improvement in our setup in Sec. III.E. Next we move to the investigation of the measurement efficiency with the weak measurement protocol in Sec. III.G.

In Ch. IV, we discuss the theory for the project that creates a tunable chemical potential for a photonic system. We start with the original theory proposal of the project from Hafezi *et al.* [70] in Sec. IV.B. Then we give a detailed introduction of our design that

directly implement Hafezi's proposal in Sec. IV.C and an alternative design we used in the experiment which consists of a qubit and lossy SNAIL resonator parametricaly coupled with each other in Sec. IV.D.

In Ch. VI, we talk about the experimental realization of the chemical potential project. Start in Sec. VI.B, we introduce how to directly implement the original theory proposal via a low frequency JPC and also discuss the practical issues which hampered this implementation. Next in Sec. VI.C, we demonstrate bath engineering by instead parametrically coupling a qubit to a lossy SNAIL mode. In Sec. VI.D, we discuss the significance of this experimental platform and its potential application in other projects.

The thesis concludes with a review of my results and a discussion of future directions which I believe may prove fruitful in Ch. VII.

II. Hamiltonian engineering tool box

A. Overview

In this chapter, we will introduce a Hamiltonian engineering toolbox for superconducting quantum computation. Starting in Sec. II.B, we introduce the key nonlinear element powering all of circuit QED: the Josephson junction (JJ). We then show how to model and quantize the system using the technique of circuit QED, and discuss how to use JJs to construct simple transmon qubits. Next, we demonstrate how to extract the information in the qubit using dispersive measurement by coupling the transmon to a microwave cavity.

In Sec. II.C, we discuss how we can extend this tool box with parametric drives. With a proper choice of drives on a system containing the right nonlinearities, certain processes can be selected under the rotating wave approximation. In Sec. II.D, we demonstrate the use of the parametric drives with the example of the Josephson Parametric Converter's parametric gain and conversion. Next in Sec.II.E we show how two port, phase-preserving amplifiers such as the JPC naturally produce two-mode squeezed light, which we will use as a quantum resource for quantum measurement in Ch. III. Finally in Sec. II.F, we discuss the Superconducting Nonlinear Asymmetric Inductive eLement (SNAIL), an alternate circuit element for generating third-order nonlinearities, and how it can be used for a bath engineering project discussed in Ch. IV and Ch. VI.

B. Superconducting qubits and dispersive measurement

Any quantum information is encoded in a quantum degree of freedom of a quantum-bit (qubit). This could be the proper energy levels in a atomic or ionic qubit [12–14], spins of the electrons in semiconductor [10, 11], the polarization of the photons [15, 16], or in our case for superconducting qubit, a degree of freedom of an electrical circuit [17, 18]. Despite the various realization platform, a system needs to have a pair of energy levels that

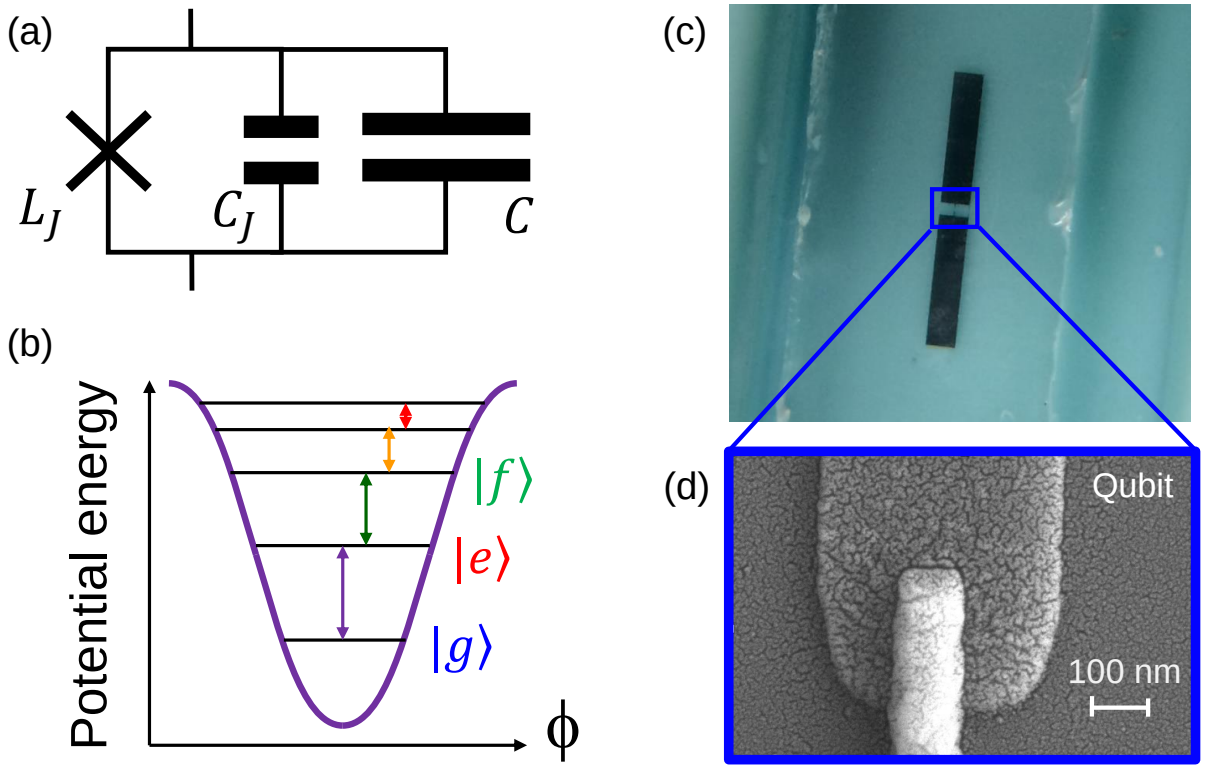

Figure 3: **Summary of transmon qubit.** (a) Circuit schematic for the transmon qubit. A transmon qubit is made by taking a Josephson junction and have it shunted with a large capacitor. To stay in the transmon regime, the ratio between the Josephson energy E_J and the charging energy E_C needs to be large enough $E_J/E_C \sim 100$ to make it insensitive to the charge noise. L_J represents the nonlinear inductance of the junction and C_J is the self capacitance of the junction while C_S is the shunting capacitance. (b) Energy diagram of a transmon qubit. It behaves as an anharmonic oscillator due the nonlinear inductance from the junction. Unlike a linear oscillator, the transmon has unequally spaced energy level. The energy level difference decrease by the anharmonicity of the qubit, allowing the transitions between energy levels to be individually driven. (c) Optical image of the transmon qubit on the sapphire chip. The large pad is used as the dipole antenna that couples the qubit to the cavity mode and also acts as the shunting capacitor for the junction. (d) An SEM image of the Josephson junction at the center of a transmon. The junction is fabricated by the Dolan bridge technique.

can be selectively addressed for it to be used as a qubit. This requires a certain amount of nonlinearity in the system. For superconducting qubits, this requirement is fulfilled by the use of Josephson junctions, a nonlinear, dissipationless circuit element, which is the most fundamental building block of superconducting quantum circuits [71]. There are many different implementation of Josephson junction [72], but the vast majority of junctions used for superconducting qubit are the S-I-S type, that is, the junction is made with one $\sim$ nm thick insulating layer sandwiched by two superconducting electrodes. Typically (and in all experiments shown in this thesis), the junction is made with aluminum electrodes and an amorphous aluminum oxide tunnel barrier. The nonlinear features of a junction can be seen from the Josephson relations [73]:

$$I(t) = I_0 \sin(\varphi(t)) \tag{II.1}$$

$$\frac{\partial \varphi}{\partial t} = \frac{V(t)}{\varphi_0} \tag{II.2}$$

where $\varphi(t)$, $I(t)$ and $V(t)$ are the superconducting phase difference across the junction, the current, and the voltage across the junction respectively, I_0 is the critical current of the junction and $\varphi_0 = \Phi_0/2\pi = \hbar/2\pi$ is the reduced magnetic flux quantum. Then, after re-writing the voltage-current relation of a junction using these two equations, we get:

$$V = \frac{\varphi_0}{I_0 \cos(\varphi)} \dot{I} = \frac{\varphi_0}{\sqrt{I_0^2 - I^2}} \dot{I}. \tag{II.3}$$

Comparing this to the usual voltage-current relation of an inductor $V = L\dot{I}$, we notice that the Josephson junction behaves like a non-linear inductor with a current dependent inductance

$$L(I) = \frac{\varphi_0}{\sqrt{I_0^2 - I^2}}. \tag{II.4}$$

The linear component of the inductance is given by $L_j = \frac{\varphi_0}{I_0}$, which described the inductance when $I \ll I_0$. We also note that, despite the inductive feature of the junctions, it also has a small capacitance which comes from the parallel plate capacitor formed by the two superconducting electrodes. Even without a shunting capacitor, a junction itself can already be considered as an anharmonic oscillator with a plasma frequency of the order of tens of gigahertz is fabricated from aluminum with a typical aluminum oxide barrier (as are all

junctions in this thesis). This frequency can be calculated by writing down its Hamiltonian and treated it the same way as we discuss below for the transmon. Based on this element, various quantum circuits have been created. There is a zoo of qubits [18], with so-called charge qubits and flux qubits arising from circuits where those quantum degrees of freedom are good bases for describing the qubit state.

In my thesis I will focus on the transmon qubit. The transmon differs from its predecessors, particularly the Cooper Pair Box [8], in that the transmon is a Josephson junction shunted by a large capacitor (see Fig. 3). The capacitor suppresses the qubit's sensitivity to the charge noise/variation and thus removes one of the major sources of dephasing. Due to the strong diluting effect of the large shunt capacitor, a transmon qubit can be modeled as a weakly anharmonic oscillator [22].This can be seen more clearly if we write down the Hamiltonian for the circuit in Fig. 3(a):

$$H = \frac{Q^2}{2C} - E_J \cos(\frac{\Phi}{\varphi_0}) \tag{II.5}$$

where $C = C_J + C_S$ is the total capacitance of the circuit, Q is the charge on the capacitor, $E_J = \varphi_0 I_0$ is the Josephson energy of the junction and $\Phi = \varphi\varphi_0$ is the flux across the junction. Then by expanding the qubit energy term, we get:

$$H = \frac{Q^2}{2C} - E_J(1 - \frac{1}{2}(\frac{\Phi}{\varphi_0})^2 + \frac{1}{24}(\frac{\Phi}{\varphi_0})^4 + O((\frac{\Phi}{\varphi_0})^4). \tag{II.6}$$

If we assume that the phase across the junction and its fluctuations remain small, we can eliminate terms past the fourth order, and get:

$$H = \frac{Q^2}{2C} + \frac{1}{2}L_j\Phi^2 - \frac{1}{24}(\frac{I_0}{\varphi_0^3})\Phi^4 \tag{II.7}$$

The linear part (first two terms) of this Hamiltonian is very similar to that of a harmonic oscillator, so it could be quantized in the same canonical way [74]. We can write Q and Φ in terms of the creation ($a^\dagger$) and annihilation (a) operators of the mode:

$$\begin{aligned} \Phi &= \sqrt{\frac{\hbar Z}{2}}(a + a^\dagger) \\ Q &= \sqrt{\frac{\hbar}{2Z}}\frac{(a - a^\dagger)}{i} \end{aligned} \tag{II.8}$$

where $Z = \sqrt{L/C}$ is the characteristic impedance of the oscillator. Then take these equations and substitute in Eq. II.7, we get:

$$H = \omega_a a^\dagger a - \frac{I_0}{24\varphi_0^3}(\sqrt{\frac{\hbar Z}{2}})^4(a + a^\dagger)^4 \tag{II.9}$$

where $\omega_a = \sqrt{1/LC}$ is the mode frequency. To simplify this Hamiltonian, we use the rotating wave approximation to drop all the fast rotating terms like $aaaa$, $aaaa^\dagger$, $aa^\dagger a^\dagger a^\dagger$... in the expansion of the fourth order term in Eq. II.9 (see next section for details about the rotating wave approximation). So we are left with:

$$H = \omega_a a^\dagger a - \frac{I_0}{16\varphi_0^3}(\hbar Z)^2 a^\dagger a a^\dagger a = \omega_a a^\dagger a - \chi_{aa} a^\dagger a a^\dagger a. \tag{II.10}$$

Now it is clear that a transmon can be viewed as an anharmonic oscillator with the anharmonicity $\chi_{aa} = \frac{I_0}{16\varphi_0^3}(\hbar Z)^2$. This form of anharmonicity is also known as a Kerr term [75,76]. The energy levels of the transmon are no longer equally spaced, as shown in Fig. 3(b), which provides the necessary frequency selectivity for it to be used as a qubit. The lowest two enegry levels $|g\rangle$ and $|e\rangle$ can be used to encode the quantum information and manipulated by microwave pulses with a bandwidth smaller than the anharmonicity. The notation for anharmoncities/Kerr terms in our circuits can be a bit tricky. Since we'll shortly need to describe cross-Kerr terms we adopt the notation χ_{ij} which would be the coefficient of a term $a_i^\dagger a_i a_j^\dagger a_j$ (a cross-Kerr), and so the anharmonicity above is given the label χ_{aa}, which we'll also refer to as a self-Kerr.

The optical image of a transmon qubit is shown in Fig. 3(c). The qubit is fabricated on a sapphire chip using E-beam lithography. The large pad serves both as the shunting capacitor and and antenna to couple the transmon to other modes (usually a linear cavity), which we will discuss in detail below. A SEM image of a transmon JJ is shown in Fig. 3(d), where the junction is made using the Dolan bridge technique [77].

However, there is not much one could do with only a bare qubit in vacuum. To make it a useful component for a quantum algorithm, it needs to be controlled and measured in a certain way. In the case of cavity QED, people have an atom interact with a cavity. The atom is isolated in this cavity with highly reflecting walls, like a box separating it from the external world. The field of this box can be quantized into a set of harmonic modes, one of

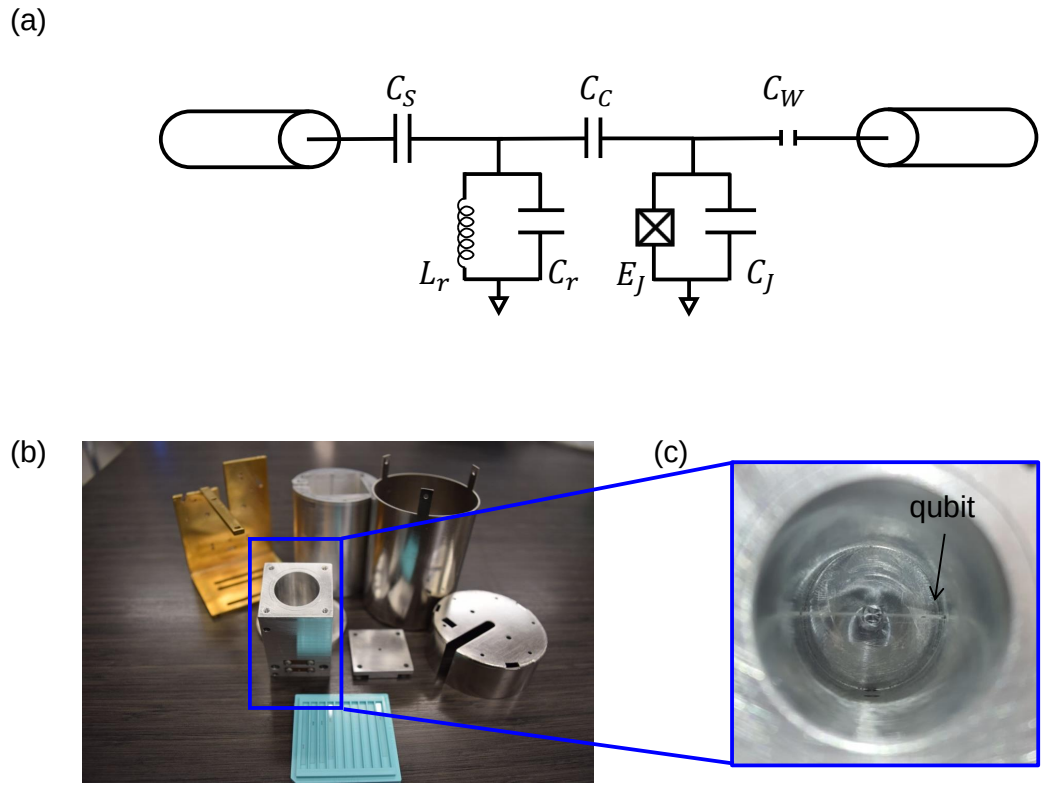

Figure 4: **Summary of dispersive measurement.** (a) Schematic of the dispersive measurement. A transmon is capacitively coupled to a microwave resonator. The cavity mode is represented as an LC-resonator. The qubit-cavity system is coupled to the external environment through two ports, a weak port that is used to drive the qubit and a strong port that is used to perform measurement. (b) Picture of all the components for a qubit-cavity system. The qubit chip with transmon qubit fabricated on it is inserted in a 3D aluminum cavity. The cavity is then placed in an aluminum shield that is inside another cryoperm shield made with high μ metal to prevent external flux fluctuations. The whole system is wrapped in mylar (not shown) and mounted at the base of a dilution fridge with a copper sample holder. (c) Qubit chip inside the 3D cavity.

which will be on resonance with the transition between two levels of the atom and thus the atom can be manipulate with a laser beam at proper frequency while we can also measure

the state of the atom by observing its spontaneous emission. Similarly in the circuit QED, we have an artificial superconducting atom (qubit) couple to a microwave cavity as shown in Fig. 4(a). Compare to the cavity QED, our system can benefit from a way stronger qubit-cavity coupling as it is easy to integrate a coupling antenna for the superconducting qubit. Now the qubit is weakly coupled to a microwave cavity with a large detuning in frequencies between them (thus in the dispersive regime with $g \ll \Delta$). Here g is the coupling strength between the qubit and cavity, whose expression will be clear in below and Δ is the frequency difference between the qubit and cavity. The cavity then couples to the transmission line strong enough to enable the readout, but now the life time of a qubit is protected by the Purcell effect since $\kappa_q = (g/\Delta)^2\kappa_c$, where κ_q and κ_c are the bandwidths of the qubit and cavity mode respectively that relate to the life time of the mode by: $T_{q,c} = 1/\kappa_{q,c}$. The control of the qubit is realized with another weak port of the system that is so weakly coupled to the transmission line that barely allows the control pulses to be sent to the qubit while not causing too much damage to its lifetime. To see how a dispersive measurement works, we can write down the Hamiltonian in terms of flux and charge, as:

$$\begin{aligned} H = &(\frac{Q_1^2}{2}\frac{1}{C_J + (C_J||C_R)} - E_J\cos(\frac{\Phi_1}{\varphi_0})) + (\frac{Q_2^2}{2}\frac{1}{C_R + (C_c||C_R)} + \frac{\Phi_2^2}{2L_R}) \\ &+ Q_1Q_2\frac{C_c}{C_RC_J + C_JC_c + C_cC_R} \end{aligned} \tag{II.11}$$

where C_J, C_R and C_c are the capacitance for the shunting capacitor of the junction, capacitor of the readout resonator and the coupling capacitor, respectively, L_J is inductance of the resonator inductor, $\Phi_{1,2}$ are the fluxes across the junction and linear inductor respectively, $Q_{1,2}$ are the charges on the shunting capacitor and resonator capacitor respectively and the symbol $||$ means to add in parallel. Based on this expression, we can further write down the Hamiltonian using the creation and annihilation operators using the same quantization technique as before and get (following in part a derivation in [59]:

$$H = \omega_a a^\dagger a - \frac{E_C}{12}(a + a^\dagger)^4 + \omega_b b^\dagger b + g_{ab}(a^\dagger b + ab^\dagger) + g_{ab}(ab + a^\dagger b^\dagger) \tag{II.12}$$

with

$$g = \frac{1}{2}\sqrt{\omega_a \omega_q}\frac{C_c}{\sqrt{(C_R + C_c)(C_J + C_c)}} \tag{II.13}$$

$$E_c = \frac{e^2}{2(C_J + (C_c||C_R))} \tag{II.14}$$

where $a(a^\dagger)$ and $b(b^\dagger)$ are the annihilation (creation) operators of the qubit and cavity mode respectively, $\omega_{a,b}$ are the bare mode frequencies for and g_{ab} is the coupling strength between the two modes. We again use the rotating wave approximation to simplify the Hamiltonian by eliminating the fast rotating term $g_{ab}(ab + a^\dagger b^\dagger)$. The remaining coupling term introduces a dressing that will redefine the two bard resonant modes. Set aside the anharmonic term and we can diagonalize the linear part of the Hamiltonian: $H = \omega_a a^\dagger a + \omega_b b^\dagger b + g_{ab}(a^\dagger b + a b^\dagger)$. This will give us the two dressed modes, with creation and annihilation operators given by:

$$\begin{pmatrix} a \\ b \end{pmatrix} = \begin{pmatrix} \lambda_a & \mu_a \\ \lambda_b & \mu_b \end{pmatrix} \begin{pmatrix} A \\ B \end{pmatrix} \tag{II.15}$$

with

$$\begin{pmatrix} \lambda_a & \mu_a \\ \lambda_b & \mu_b \end{pmatrix} = \begin{pmatrix} -g_{ab}\sqrt{\frac{1+\frac{1}{4g_{ab}^2}(\Delta+\sqrt{4g^2+\Delta})^2}{4g^2+\Delta^2}} & -\frac{\Delta-\sqrt{4g^2+\Delta^2}}{2}\sqrt{\frac{1+\frac{1}{4g_{ab}^2}(\Delta+\sqrt{4g^2+\Delta})^2}{4g^2+\Delta^2}} \\ g_{ab}\sqrt{\frac{1+\frac{1}{4g_{ab}^2}(\Delta-\sqrt{4g^2+\Delta})^2}{4g^2+\Delta^2}} & \frac{\Delta+\sqrt{4g^2+\Delta^2}}{2}\sqrt{\frac{1+\frac{1}{4g_{ab}^2}(\Delta-\sqrt{4g^2+\Delta})^2}{4g^2+\Delta^2}} \end{pmatrix} \tag{II.16}$$

where $\Delta = \omega_b - \omega_a$ is the difference between the bare resonator frequencies and $A(A^\dagger)$ and $B(B^\dagger)$ are the annihilation (creation) operators for the new dressed mode. Then the linear part of the Hamiltonian can be written in the new dressed basis as:

$$H = \omega_A A^\dagger A + \omega_B B^\dagger B \tag{II.17}$$

with

$$\omega_A = \frac{1}{2}(\omega_a + \omega_b - \sqrt{4g^2 + \Delta^2}) \tag{II.18}$$

$$\omega_B = \frac{1}{2}(\omega_a + \omega_b + \sqrt{4g^2 + \Delta^2}) \tag{II.19}$$

where ω_A and ω_B are new dressed frequencies. The we can return to the anharmonic term $\chi_{aa}a^\dagger a a^\dagger a$ where now a and $a^\dagger$ need to be replaced with the new dressed operators. So the new Hamiltonian will be:

$$H = \omega_A A^\dagger A - \chi_{AA} A^\dagger A A^\dagger A + \omega_B B^\dagger B - \chi_{BB} B^\dagger B B^\dagger B + \chi_{AB} A^\dagger A B^\dagger B \tag{II.20}$$

with

$$\chi_{AA} = -\frac{E_c}{2}\lambda_b^4 \tag{II.21}$$

$$\chi_{BB} = -\frac{E_C}{2}\mu_b^4 \tag{II.22}$$

$$\chi_{AB} = -\frac{E_C}{2}(4\lambda_b^2\mu_b^2) \tag{II.23}$$

where χ_{AA} and χ_{BB} are the new anharmonicities for the new dressed mode and χ_{AB} is the dispersive shift between the two modes. These three non-linear coefficients are connected by $\chi_{AB} = -2\sqrt{\chi_{AA}\chi_{BB}}$. A typical choice of qubit frequency is $\omega_A/2\pi = 4 \sim 10$ GHz with anharmonity $\chi_{AA}/2\pi = 160 \sim 200$ MHz, for cavity frequency is $\omega_B/2\pi = 5 \sim 10$ GHz (but is detuned by many gigahertz from the qubit frequency to stay in the dispersive regime) with a small self Kerr $\chi_{BB} \sim 1$ KHz and finally for the dispersive shift $\chi_{AB} = 0.1 \sim 10$ MHz depends on the experimental requirements. To see how the dispersive measurement works, we can re-arrange the terms in Eq. II.20 and get:

$$H = \omega_A A^\dagger A - \chi_{AA} A^\dagger A A^\dagger A + (\omega_B - \chi_{AB} A^\dagger A) B^\dagger B. \tag{II.24}$$

We neglect the small Kerr term for the cavity mode. The above derivation shows that for a qubit-cavity system with a dipole-dipole coupling, it can be reduced to a dispersively coupled system in a new dressed basis under the RWA, provided the coupling strength is much weaker than the detuning between the mode frequencies ($g \ll \Delta$). In the new dressed system, both eigenstates have mixed with the bare qubit mode and bare cavity mode due to the mode hybridization, but one is more 'qubit' like (with an almost undiminished anharmonicity) and the other is more 'cavity' like (inheriting only a small anharmonicity) due to the weak coupling strength. And by absorbing the dispersive term into the coefficient of $B^\dagger B$, we can see the effect of this coupling, that is, that state of the qubit will change the frequency of

the cavity as shown in Fig. 4(a). Thus by monitoring the frequency change of the cavity, we could then infer the state of the qubit.

In circuit QED, we engineer the system with the help of hybridization of modes and the nonlinearity of Josephson junctions. In the dispersive Hamiltonian considered above, the capacitive coupling between the qubit and cavity provides the mode hybridization. The new basis in the dressed system after the hybridization contains both the bare qubit and cavity modes which then spreads the anharmonicity of the qubit to the coupling between the new dressed modes. As we will see later in the SNAIL example in Ch. II, we can apply the same technique to create third order couplings between modes of the system.

C. Rotating wave approximation and parametric coupling

In the derivation of the qubit and the dispersive Hamiltonian, we drop the terms that will not survive the rotating wave approximation. Taking the case of the qubit as an example, where we start with Eq. II.9 and discard terms to arrive at Eq. II.10. That is, the term $(a + a^\dagger)^4$ is simplified to $a^\dagger a a^\dagger a$ using the rotating wave approximation (RWA). The usual argument given is that terms which do not conserve energy, e.g. aa which removes a pair of photons from the a mode, don't act, or, put another way, oscillate at frequencies far from the frame of the qubit and so average out. This effect can be seen clearly by moving the system to a rotating frame with the rotation operator $R = \exp(-i\omega_a a^\dagger a t)$ chosen to oscillate at the negative of the qubit frequency. The transformation of the Hamiltonian with a unitary operator is given by:

$$H' = UHU^\dagger + i\hbar\dot{U}U^\dagger. \tag{II.25}$$

The nonlinear part of the qubit Hamiltonian ($(a + a^\dagger)^4$) under this transformation becomes:

$$\begin{aligned} R(a + a^\dagger)^4 R^\dagger &= (ae^{-i\omega_a t} + a^\dagger e^{i\omega_a t})^4 \\ &= \Sigma_{n+m=4}\ c_{ij}(a)^n (a^\dagger)^m e^{i\omega t(m-n)} \end{aligned} \tag{II.26}$$

where c_{ij} are the coefficients for the corresponding term in the expansion of the fourth term. Note that when $(m \neq n)$, the term will carry a coefficient that rotates with a frequency at the

order of gigahertz ($\sim \omega_a$), whereas the qubit state itself now evolves with a center frequency of zero. Picking which terms are far enough in frequency/whose effect will be averaged away is the essence of the RWA (and a major source of peril in complicated systems where there are terms that are safe, not so safe, and absolutely a bad idea but still probably discarded by an incautious experimenter). In the example given, after applying the RWA we are left with the term with $n = m = 2$, which is the non-linear term in Eq. II.10.

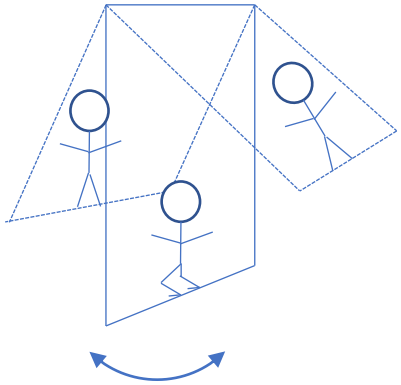

Figure 5: **A child on a swing.** The child is parametrically driving the swing by periodically standing and squatting to vary the moment of inertia of the swing as a pendulum. When the swing is driven at twice of the frequency of its oscillations, a 'gain' process is triggered, that is the amplitude of the swing's oscillation is increased.

This example inspires a thinking that if we want to look at which terms can survive in the RWA, they are basically the terms of products of number operators, as the case in the Kerr terms.

In another way, this means that an odd order term in the Hamiltonian seems to be doomed in the RWA as there will always be a single operator left behind after we factor out the number operators.

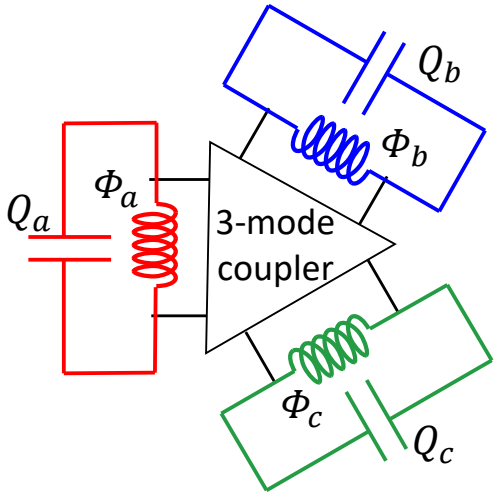

Figure 6: **Schematic of three-wave coupling.** Three linear modes (demonstrated as LC resonators) are hybridized via a three-mode coupler. With the hybridization, non-linearity distributes among the three modes, creating the desired third-order coupling term.

However, when we add drives to the system, we can utilize these non-rotating terms to produce important controls on our system which *will* survive the rotating wave approximation. We refer to these drives and the Hamiltonian terms they produce as 'parametric'. This term has real meaning for some cases, such as for a child on a swing as shown in Fig. 5. In this example, we think of the child + swing as a pendulum system and as the child changes their body position and/or swings their legs they are changing a physical parameter of the system, namely its length (the distance from the pivot point to the center of mass) [78]. For electrical circuits, one can also make a physical analogy to, for instance, parametrically varying a mutual inductance between two modes [79].

To better explain a standard parametric process in our laboratory, we can start with a simple but useful example shown in Fig. 6. Imagine we have three simple harmonic modes, although we demonstrate them as simple LC circuit in the figure, they could also be the modes in other platforms like ion trap, optical photons or electric spins. Then, consider a three-mode coupler that couples these modes together, again, we are using the junction

based device for the coupler, but there are implementations using diodes, opto-mechanics couplers and optical fibers. In terms of the Hamiltonian, the purpose of the coupler is to provide an three-wave mixing interaction Hamiltonian term:

$$H_{int} = \hbar g_3 \Phi_a \Phi_b \Phi_c \tag{II.27}$$

where g_3 is the coupling strength between the modes. If we rewrite them in terms of creation and annihilation operators using the similar quantization technique in Eq. II.8, we get:

$$H_{int} = \hbar g_{abc}(a + a^\dagger)(b + b^\dagger)(c + c^\dagger) \tag{II.28}$$

where $g_{abc} = g_3\sqrt{\frac{\hbar Z_a}{2}}\sqrt{\frac{\hbar Z_b}{2}}\sqrt{\frac{\hbar Z_c}{2}}$ is the new coupling strength with the correction from the quantization coefficients. As we see in the case of fourth order terms, if none of the combinations of mode frequencies $\pm\omega_a$, $\pm\omega_b$ and $\pm\omega_c$ is zero (which is the case for most of the mode frequency choices), then Eq. II.28 will not survive the RWA. However, if we can parametrically pump one of the modes, say, mode c at a special frequency that is also far detuned from its eigenfrequency ω_c. Then this pump can be considered as 'stiff', meaning that we can replace the operator by its classical average [80]:

$$c \to \langle c \rangle e^{-i(\omega_p t + \phi_p)} \tag{II.29}$$

where ω_p is the pump frequency and ϕ_p is the phase of the pump. If we substitute this into the interaction Hamiltonian in the rotating frame, we get:

$$H'_{int} = \hbar g_{abc}(ae^{-i\omega_a t} + a^\dagger e^{i\omega_a t})(be^{-i\omega_b t} + b^\dagger e^{i\omega_b t})(\langle c \rangle e^{-i(\omega_p t + \phi_p)} + \langle c \rangle e^{i(\omega_p t + \phi_p)}). \tag{II.30}$$

shows that it takes one pump photon and creates a pair of photons in a and b modes.

Then by carefully choosing the pump frequency ω_p we can select the desired parametric process to survive the RWA.

Here we consider two single pump cases, the 'gain' and 'conversion' processes, where we applied the pump at the frequency $\omega_p = \omega_a + \omega_b$ and $\omega_p = \omega_a - \omega_b$, respectively. Under the RWA, the Hamiltonian in Eq. II.30 can be reduced to the effective two-body Hamiltonian:

$$H_G = \hbar g_{abc}\langle c \rangle (abe^{i\phi_p} + a^\dagger b^\dagger e^{-i\phi_p}) \tag{II.31}$$

$$H_C = \hbar g_{abc}\langle c \rangle (ab^\dagger e^{i\phi_p} + a^\dagger b e^{-i\phi_p}) \tag{II.32}$$

In the gain process, the term $(a^\dagger b^\dagger \langle c \rangle e^{-i\phi_p})$ that comes from $a^\dagger b^\dagger c$ shows that pump photons are destroyed to create photon pairs in mode a and b and therefore leads to an amplification in the two modes. Similarly for the conversion process, $(ab^\dagger + a^\dagger b)$ gives a photon swapping term between the two modes, thus converting (or swapping) the photon from one mode to another, and vice versa. This heuristic argument shows that the parametric pumps can select out parametric processes.

Although parametric drives give us the access to the desired parametric processes, we also need to pay attention to not activating other undesired parametric processes by accident. Those terms usually come from the higher order terms in the system that will also survive the RWA with the presence of the parametric drives. One example is the effect of the fifth order term, such as $g_{abccc} c^\dagger c (abc^\dagger + a^\dagger b^\dagger c)$, now with the drive we are effectively adding a change to the coupling strength for the third order term through $g_{abccc} |\langle c \rangle|^2$. These higher order terms are natural in our Josephson Ring Modulator (JRM) and Superconducting Nonlinear Asymmetric Inductive eLement (SNAIL) circuits, and can limit the performance of the device. We are working to understand their effects and eliminate them with better Hamiltonian engineering [81, 82].

A related issue is the effect of dispersive terms in the system due to large numbers of pump photons. For simplicity, let us consider a cross Kerr term between the pump mode c and mode a: $g_{aacc} a^\dagger a c^\dagger c$. This term becomes $g_{aacc} |\langle c \rangle|^2 a^\dagger a$ with the drive, by combining this to the linear part of this mode $\omega_a a^\dagger a$, we note the effect of the drive is to create a pump dependent frequency shift in mode a. This creates extra difficulties when we try to implement multi-parametric pump protocols (see Ch. IV and Ch. VI).

D. The Josephson Parametric Converter

In this section, we introduce how to use the parametric coupling technique with actual device: Josephson Parametric Converter (JPC). A JPC is a three-wave mixing device, that can be operated both as an amplifier and a coherent converter. The three-wave mixing coupling is provided by the Josephson ring modulator (JRM), the core part of the JPC. The

JRM is formed by four identical junctions in a loop and is then placed at the center of two $\lambda/2$ resonators as shown in Fig. 7(a). These resonators are capacitively coupled to external transmission line to allow the control and pump of the device. There are three accessible modes of a JRM that we label as a, b and c, as shown in Fig. 7(b). For a detailed analysis of the eigenmode of a JRM, please see reference [80, 83]. The Hamiltonian for a JRM is given by:

$$\begin{aligned} H_{JRM} = &-4E_J(\cos(\frac{\varphi_a}{2})\cos(\frac{\varphi_b}{2})\cos(\varphi_c)\cos(\frac{\varphi_{ext}}{4})) \\ &- 4E_J\sin(\frac{\varphi_a}{2})\sin(\frac{\varphi_b}{2})\sin(\varphi_c)\sin(\frac{\varphi_{ext}}{4}) \end{aligned} \tag{II.33}$$

where the E_J is the Josephson energy of each junction, φ_i is the reduced flux of each mode and φ_{ext} is the reduced external flux that goes through the JRM. For small fluxes, $\varphi_{a,b,c} \ll 1$, we can expand this Hamiltonian and get:

$$\begin{aligned} H_{JRM} = &E_J\cos(\frac{\varphi_{ext}}{4})(\frac{\varphi_a^2}{2} + \frac{\varphi_b^2}{2} + 2\varphi_c^2 - 4) \\ &- E_J\sin(\frac{\varphi_{ext}}{4})\varphi_a\varphi_b\varphi_c \end{aligned} \tag{II.34}$$

where the first term on the left represent the linear inductance energy of the JRM and will be absorbed into the linear part of the JPC's full Hamiltonian. The second term on the left provides the desired the three-wave mixing term as in the Eq. II.27.

As discussed previously, two simple parametric processes involving two coupled modes are phase-preserving gain and conversion. To understand theses processes in the JPC (first described in Ref. [84, 85], we need to start with the full Langevin equations of motion for the system (use mode a as an example):

$$\frac{da(t)}{dt} = \frac{i}{\hbar}[H, a(t)] - \frac{\kappa_a}{2}a(t) + \sqrt{\kappa_a}a_{in}(t) \tag{II.35}$$

where κ_a is the bandwidth of mode and a_{in} is the incoming waves in the external transmission line that couples to the JPC. It is related to the outgoing waves a_{out} and the JPC's internal mode a via the input/output relation [86]:

$$\sqrt{\kappa_a}a(t) = a_{in}(t) + a_{out}(t) \tag{II.36}$$

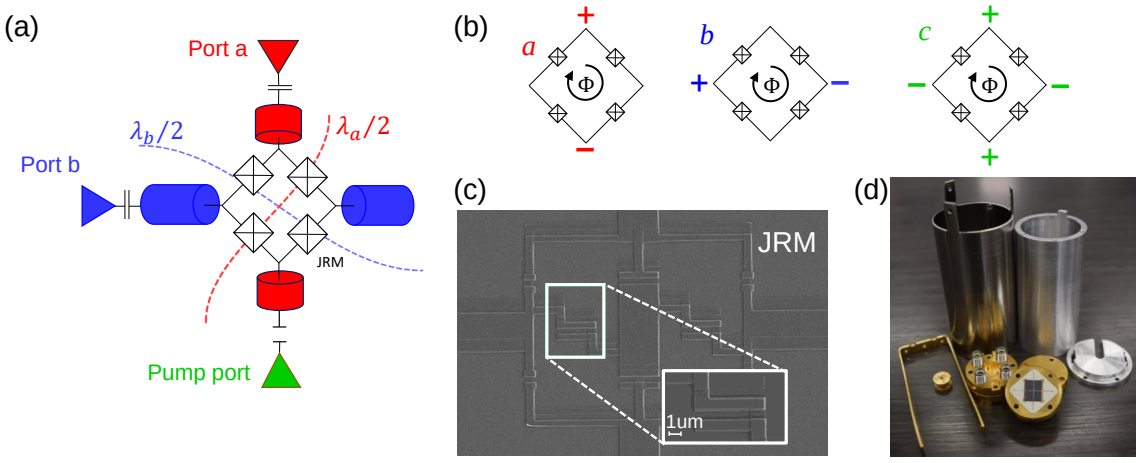

Figure 7: **Summary of the Josephson Parametric Converter.** The Josephson Parametric Converter (JPC) is made with a Josephson Ring Modulator (JRM), a ring consisting of four identical junctions, placing in the middle of two $\lambda/2$ microstrip resonators. The device is capactively coupled to the external transmission lines to allow the measurement and pump of the modes. (b) Eigenmodes of a JRM. A JRM can support three accessible modes with different voltage configuration. (c) An SEM picture of the JRM used in the JPC. Like the junction in the qubit, JRM is also fabricated using Dolan bridge technique. (d) Picture of all the components for a JPC. The silicon chip with JPC is placed in a copper sample box which is mounted on a copper sample holder with a magnetic coil attached to it. The sample box is then placed in an aluminum shield that is inside another cryoperm shield made with high μ metal to prevent the external flux fluctuations.

Now let us start with the gain process, with the interaction Hamiltonian given in Eq. II.31, we get the Langevin equation:

$$\frac{da(t)}{dt} = -i\omega_a a(t) - ig_{abc}b^\dagger(t)\langle c\rangle e^{-i\phi_p} - \frac{\kappa_a}{2}a(t) + \sqrt{\kappa_a}a_{in}(t) \tag{II.37}$$

$$\frac{db(t)}{dt} = -i\omega_b b(t) - ig_{abc}a^\dagger(t)\langle c\rangle e^{-i\phi_p} - \frac{\kappa_b}{2}b(t) + \sqrt{\kappa_b}b_{in}(t) \tag{II.38}$$

To solve this equation, we can take a Fourier transform on both side and substitute in the

input/output relation, we get:

$$(i\omega_1 - i\omega_a - \frac{\kappa_a}{2})a_{out}[\omega_1] - ig_{abc}\langle c\rangle\sqrt{\frac{\kappa_a}{\kappa_b}}\langle c\rangle e^{-i\phi_p}b^\dagger_{out}[-\omega_2] =$$
$$(i\omega_a - i\omega_1 - \frac{\kappa_a}{2})a_{in}[\omega_1] + ig_{abc}\langle c\rangle\sqrt{\frac{\kappa_a}{\kappa_b}}e^{-i\phi_p}b^\dagger_{in}[-\omega_2] \quad \text{(II.39)}$$
$$(-i\omega_2 + i\omega_b - \frac{\kappa_b}{2})b^\dagger_{out}[-\omega_2] + ig_{abc}\langle c\rangle\sqrt{\frac{\kappa_b}{\kappa_a}}\langle c\rangle e^{i\phi_p}a_{out}[\omega_1] =$$
$$(-i\omega_b + i\omega_2 - \frac{\kappa_b}{2})b^\dagger_{in}[-\omega_2] - ig_{abc}\langle c\rangle\sqrt{\frac{\kappa_b}{\kappa_a}}e^{i\phi_p}a_{in}[\omega_1] \quad \text{(II.40)}$$

where we use ω_1 and ω_2 as the frequency variables in the Fourier transform for mode a and b, respectively. By solving this linear equation group, we are able to get the scattering matrix for the system:

$$\begin{pmatrix} a_{out}[\omega_1] \\ b^\dagger_{out}[-\omega_2] \end{pmatrix} = \begin{pmatrix} S_{11} & S_{21}e^{-i\phi_p} \\ S^*_{21}e^{i\phi_p} & S_{22} \end{pmatrix} \begin{pmatrix} a_{in}[\omega_1] \\ b^\dagger_{in}[-\omega_2] \end{pmatrix}. \quad \text{(II.41)}$$

If we consider the on resonance case, where $\omega_1 = \omega_a$ and $\omega_2 = \omega_b$, we can get a relative simple expression for the scattering matrix elements:

$$\begin{pmatrix} a_{out}[\omega_1] \\ b^\dagger_{out}[-\omega_2] \end{pmatrix} = \begin{pmatrix} \sqrt{G} & -i\sqrt{G_T}e^{-i\phi_p} \\ i\sqrt{G_T}e^{i\phi_p} & \sqrt{G} \end{pmatrix} \begin{pmatrix} a_{in}[\omega_1] \\ b^\dagger_{in}[-\omega_2] \end{pmatrix} \quad \text{(II.42)}$$

with a reflection gain

$$G = \frac{1+\rho^2}{1-\rho^2} \quad \text{(II.43)}$$

and a trans-gain

$$G_T = \frac{2\rho^2}{1-\rho^2} = G - 1 \quad \text{(II.44)}$$

where ρ is the dimensionless pump parameter:

$$\rho = \frac{g_{abc}\langle c\rangle}{\sqrt{\kappa_a\kappa_b}} \quad \text{(II.45)}$$

for the detailed expression of $G(\omega)$ and $G_T(\omega)$ for the off resonance case, see reference [87].

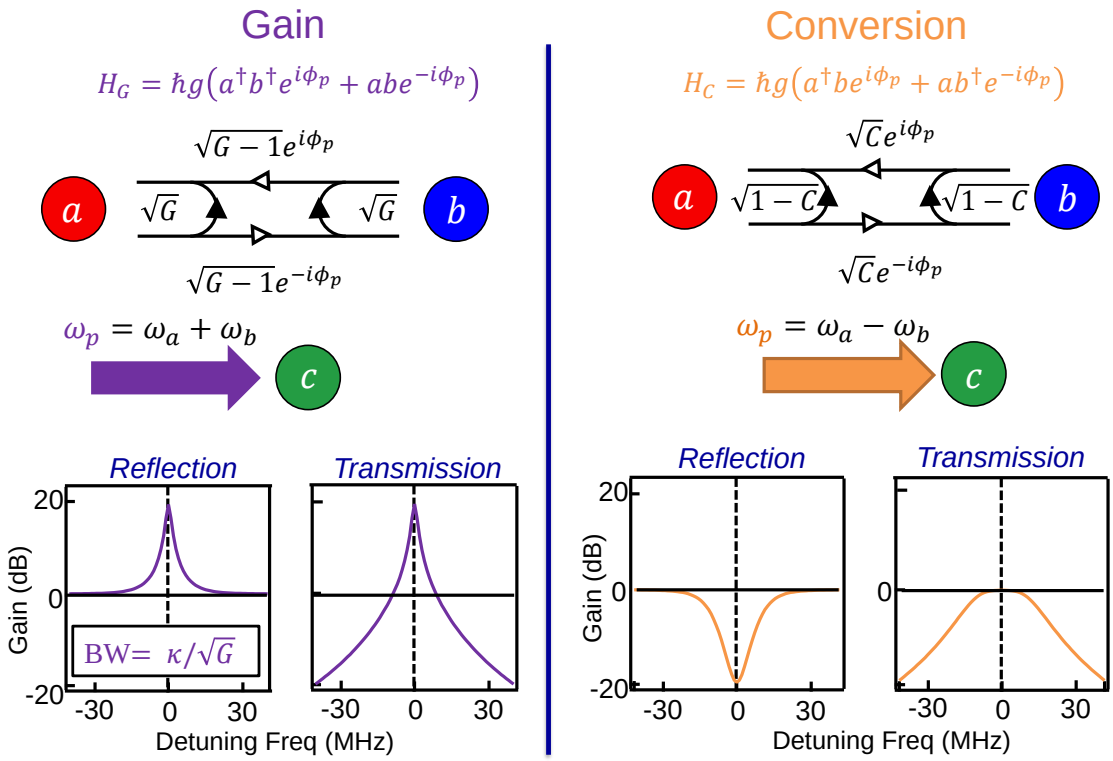

Figure 8: **Gain and conversion process of a JPC.** Two single-pump parametric processes in a JPC. The JPC can be operated in the amplification mode and converter mode with the pump frequency of $\omega_p = \omega_a + \omega_b$ and $\omega_p = \omega_a + \omega_b$ respectively. In the amplification mode, on resonance signal receives a reflection power gain of G and a transmission power gain of $G - 1$. In the converter mode, on resonance signal receives a unit conversion from one mode to another.

The scattering matrix for the conversion process can be obtained with the same method using the interaction Hamiltonian in Eq. II.32. The on resonance scattering matrix for this process is:

$$\begin{pmatrix} a_{out}[\omega_1] \\ b_{out}[\omega_2] \end{pmatrix} = \begin{pmatrix} \sqrt{1-C} & i\sqrt{C}e^{-i\phi_p} \\ -i\sqrt{C}e^{i\phi_p} & \sqrt{1-C} \end{pmatrix} \begin{pmatrix} a_{in}[\omega_1] \\ b_{in}[\omega_2] \end{pmatrix} \tag{II.46}$$

with conversion coefficient:

$$C = \frac{4g_{abc}^2\langle c\rangle^2/(\kappa_a\kappa_b)}{(1+g_{abc}^2\langle c\rangle^2/(\kappa_a\kappa_b))^2}. \tag{II.47}$$

A summary of the gain and conversion processes is shown in Fig. 8. Note that one important difference between conversion and gain is that conversion does not conjugate the transmitted signal, and the gain process does. This is seen by the output scattering component for trans gain being at $b_{out}^\dagger[-\omega_2]$. This has several consequences. First, when driving a JPC mode off-resonance, let us assume on mode a, at detuning $+\Delta$, the second (idler) tone produced by the gain process in mode b will be at $-\Delta$, whereas the conversion process produces converted photons at $+\Delta$ in mode b. More, the phase of the input signal will be reversed in the gain process (the dagger operator acting like a complex conjugate only for semiclassical fields). For simple reflection gain (the most common use of a JPC), these details can be ignored, but in the following discussion of two-mode squeezed light and the interferometric qubit measurement detailed in Chapter III.

E. Two-mode squeezed light generated from a JPC

For the parametric amplifiers like the JPC, there are a few key metrics, such as a large amplification bandwidth, a high saturation power and a good measurement efficiency. A large amplification bandwidth is useful when the experiment needs to multiplex multiple channels in the measurement. This requirement can be lifted if the experiment only involves one measurement channel. The saturation power means the highest the power the amplifier can handle before the gain starts to drop and the signal begins to distorted. This has been an ongoing challenge since the higher order terms will shift the mode frequencies and modulating the effective coupling strength, as we discussed above (also see in references [82, 88, 89]).

The efficiency of an amplifier is limited by its added noise, which ideally should be one half-photon for phase-preserving amplifiers and zero for phase-sensitive amplifiers on resonance [53, 90].We can see from Eq. II.39 that there is a creation of b mode photons in the equation of motion for the a mode (and vice versa), which comes from the three-wave mixing

term in the JPC Hamiltonian. So, vacuum fluctuation from the b mode will always be added to the amplified signal in a mode, even if there is no input on the b mode. This added noise, as Caves pointed out [53], is a fundamental requirement from quantum mechanics for all the phase persevering amplifiers like JPC and thus puts a limit on the signal-to-noise ratio (SNR) for a certain measurement strength. The presence of internal losses in the amplifier will effectively send part of the quantum information in the signal to an un-monitored channel (and allow fluctuations in that channel to couple back into the amplified signal), and thus cause a decrease in the total measurement efficiency. This issue can be potentially improved with better fabrication process that yields higher internal quality factor. It is also possible that unwanted parametric couplings and nonlinearity can result in overproduction of noise in our amplifiers, though we do not have direct evidence that this is an issue.

This concept, that amplifiers 'add noise' makes perfect sense if the concept of measurement is to gain knowledge of an input signal. In particular, if we view a phase-preserving amplifier as allowing us to view the quadratures, (I, Q), of a propagating microwave field, the fact that $[I, Q] \neq 0$ prevents us from gaining perfect knowledge of both quadratures simultaneously, and Cave's quantum limit can be thought of as the minimum added fluctations to these quantities to satisfy the commutation relation.

However, we can instead ask 'what kind of light does an amplifier produce'. In that case, we are not simply interested in the signal output of the amplifier, but in the total state of both outputs. From that viewpoint, we discover that the output of an undriven phase-preserving amplifier with two explicit ports such as the JPC is two-mode squeezed (TMS) light [91–93].When operating in the gain mode, the Hamiltonian of a JPC is:

$$\frac{H_{JPC}}{\hbar} = \omega_a a^\dagger a + \omega_b b^\dagger b + \omega_c c^\dagger c + g_3(a^\dagger b^\dagger c + abc^\dagger), \tag{II.48}$$

As we discussed above, the phase-preserving amplification is achieved by applying a strong microwave drive to the common mode at frequency $\omega_p \simeq \omega_a + \omega_b$. The Hamiltonian will reduce the three-wave mixing term to an effective two-wave coupling term between the signal and idler mode: $g_3 \langle c \rangle (e^{i\phi_p} a^\dagger b^\dagger + e^{-i\phi_p} ab)$. This two-mode Hamiltonian can also be described by the two-mode squeezing operator [92, 93]: $S = \exp(re^{-i\phi_p} ab - re^{i\phi_p} a^\dagger b^\dagger)$, where $re^{i\phi_p}$ is the complex squeezing parameter with the squeezing strength $r = \cosh^{-1}\sqrt{G}$ [94, 95] as

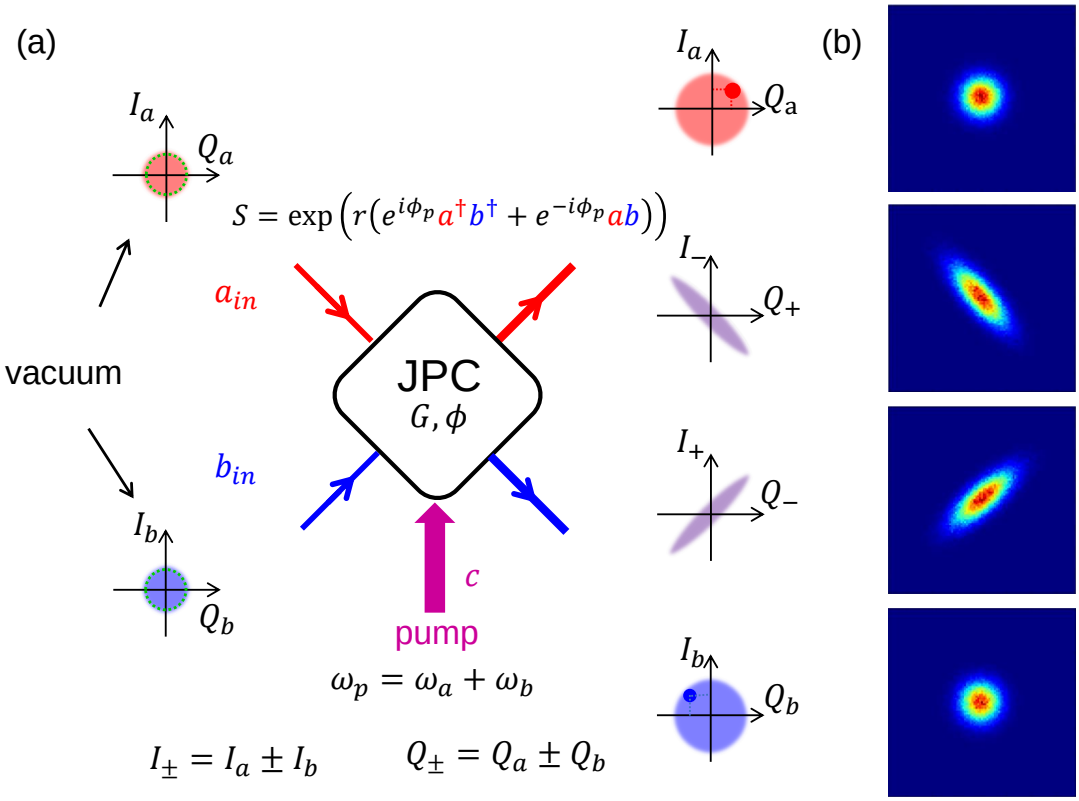

Figure 9: **Generation of two-mode squeezed light with JPC.** (a) Schematics of the generation of TMS light with JPC. By applying a stiff drive to the JPC's common mode at summation frequency of signal and idler mode, the independent vacuum fluctuations on the input ports will be turned into a tightly correlated quantum state: two-mode squeezed state. When measuring each mode separately, it behaves like the thermal state, see plot of (I_a, Q_a) and (I_b, Q_b). What is actually squeezed is the correlation relations between the two modes, see plot of (I_+, Q_-) and (I_-, Q_+). (b) The hist plots of data for $I_a, Q_a, I_b, Q_b, I_\pm$ and $Q_\pm$, corresponds to the theoretical plots in (a), respectively.

shown in Fig. 9(a). For TMS light, each mode behaves like a thermal state when observed separately; what is actually squeezed is their correlation relation. That is, if we measure mode a and get a result of I_{a0}, Q_{a0} (the red dot in Fig. 9(a)), since now the correlation between I_a, Q_a, I_b and Q_b is set up to the limit given by the squeezing strength, we will

be able to predict the result of the measurement for mode b to be a gaussian distribution centered at I_{b0}, Q_{b0} (the blue dot in Fig. 9(b)) with a characteristic width corresponding to 1/2 photon. Put another way, the signal and idler output modes of the JPC produce light which is random in time but correlated to the last half photon [96]. We can perform a such measurement on our JPC, a typical data set is shown in Fig. 9(b). Note that the cross-correlations are not as fine as the ultimate limit of a half-photon as this correlation is *after* the amplifier. Observing this fully would require yet another quantum limited amplifier to lift these correlations above the added noise of the rest of the amplification chain, in practice we don't do this and so the ultimate limit in observed fluctuations is dominated by the noise of the HEMT amplifier at 4 K. Nevertheless, the good agreement between the experiment and the theoretical result shows that the JPC, or any other non-degenerate phase-preserving amplifier, can also serve as a generator of two-mode squeezed light with both spectral and spacial non-degeneracy [97, 98].

The central question about TMS I pursue in this thesis is to determine whether it can be used as a tool for measurement. Perhaps alternately, if we perform a quantum measurement using TMS light as a resource, what can we learn about the light our amplifiers produce? As our TMS light necessarily involves two modes, the measurement apparatus takes the form of an interferometer using two JPCs, the first to produce TMS light, and the second to recombine and further the two halves of the squeezed light to produce the measurement output. This is the focus of Chapter III, where we follow a modified version of a proposal by Barzanjeh *et al.* [99].

F. The Superconducting Nonlinear Asymmetric Inductive eLement

The Superconducting Nonlinear Asymmetric Inductive eLement(SNAIL) was recently introduced by Devoret group at Yale University [100]. It is designed to be a dipole circuit element with third order nonlinearity and little or no fourther order nonlinearity. As shown in Fig. 10, the SNAIL is a superconducting loop of n Josephson junctions (here $n = 3$ in our case) and a single smaller junction. The whole loop is threaded with magnetic flux Φ_{ext}.

The Hamiltonian for the SNAIL is:

$$H_{SNAIL} = -\alpha E_J \cos(\varphi) - 3E_J \cos(\frac{\varphi_{ext} - \varphi}{3}) \tag{II.49}$$

where E_J and αE_J are the Josephson energies for the large and small junctions, respectively, φ is the reduced the flux across the small junction and $\varphi_{ext} = \Phi_{ext}/\varphi$ is the reduced external flux. Note here we assume the flux across each large junction is the same. Then, by numerically minimizing the energy in Eq. II.49, we can Taylor expand this Hamiltonian near the minimum φ_{min}:

$$H = E_J(c_2(\varphi - \varphi_{min})^2 + c_3(\varphi - \varphi_{min})^3 + c_4(\varphi - \varphi_{min})^4 + ...) \tag{II.50}$$

where the coefficients for each order are functions of α and φ_{ext}: $c_i = c_i(\alpha, \varphi_{ext})$. Then, with a proper choice of α and φ_{ext} [100, 101], we can find an optimal bias point, where $c_3 \neq 0$ while $c_4 = 0$ at which the SNAIL provides a close to ideal third order mixing element.

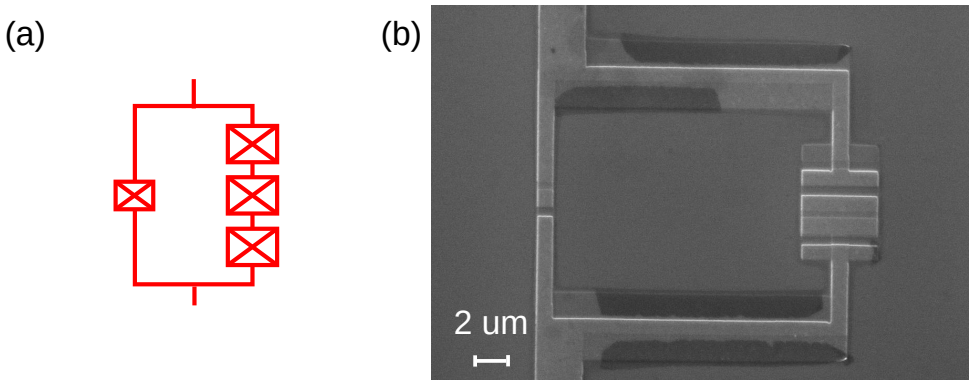

Figure 10: **The SNAIL.** (a) Circuit schematic of a SNAIL. The SNAIL is a loop of three large junctions and a single small junction. The whole loop is threaded with magnetic flux. (b) A SEM image of a SNAIL. The small junction is on the left (central bright overlapping region), and the three junctions are on the write (middle 3 of the 5 visible rectangles). Note that we couple the leads as close as possible to the small junction to avoid the effects of stray inductance.

This behavior is also available in linearly shunted JRMs [81, 102], which have the further advantage of three orthogonal modes to the SNAILs one. However, the SNAILs single mode is actually a tremendous advantage in practice, as we can simply print a snail in a given mode of whatever form to gain third order couplings. To couple multiple modes together to create trans-third order couplings (e.g. g_{sas}, where a is some linear mode and s the SNAIL mode), we make use of hybridization (see method in Ch. V.B). This produces necessarily weaker terms, and more than are typically wanted (the above example also produces g_{saa} and g_{aaa}), but we are finding in our experiments that this is less of a problem than finding ways to connect three modes to the 4 ports of JRMs.

The SNAIL device have a large range of applications. In other recent work in the lab, the SNAIL has been used to replace the JRM in the JPC so that we can form new amplifiers with an arbitrary number of modes, see Fig. 11(a) (for example four which is not readily achievable wit ha single JRM), while still being operated at a fourth order suppression point. This creates a device very suitable to work with multi-pump protocols that could lead to a directional amplifiers [103, 104]. My colleague T.-C. Chien has christened this design the SHARC amplifier (like the SNAIL the acronym is primarily chosen to produce a neat animal name, so I won't bother naming it here) based on this idea and promising data has been observed [81].

Another possible application for the SNAIL is to add a shunting capacitor to make it a 'SNAILmon' like we did for the transmon qubit. Then the SNAILmon is self can be used as a non-linear Kerr resonator to generate Schrödinger cat state [105] or to have it couple to other qubit/resonator systems, to implement a two-qubit gate [38] by driving the third order term, see Fig. 11(b). We could also use the SNAIL to couple a few high-Q cavity modes together, see Fig. 11(c). Then by driving the conversion processes between these mode, we could transfer the information around these modes and thus create a quantum signal router. This router could be an important part for future modular quantum computers.

In this thesis, in Ch. IV and Ch. VI we will introduce a bath engineering project realized by coupling a transmon qubit to a SNAILmon, see Fig. 11(d). The idea of bath engineering is to design a certain coupling between the system and a dissipative bath to engineer an unusual effective qubit dissipation which can be used to perform a useful task. Using the

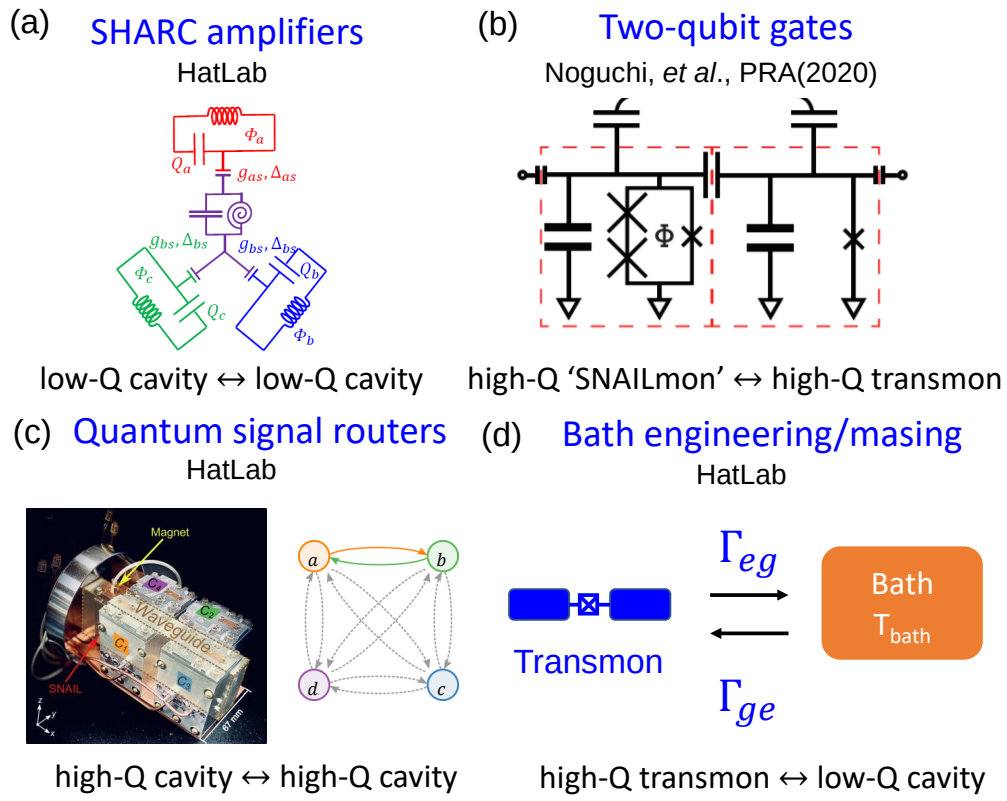

Figure 11: **Applications of SNAILs** (a) A Superconducting Hybridized ARbitrary Cavity-based (SHARC) amplifier. The amplifier is based on the SNAIL induced three-wave coupling between three low-Q linear modes. (b) An implementation of a two-qubit gate by couling a 'SNAILmon' to a transmon and parametrically drive the third order term in the system [38]. (c) Use the SNAIL to couple several high-Q cavity mode and drive the conversion process from the SNAIL can create a quantum signal routers which could be an important part in a modular quantum computer. (d) Engineering the system-bath interaction by having the high-Q transmon qubit couple to a lossy bath mode through a SNAIL. This will be the focus of my second project in Ch. IV and Ch. VI.

SNAIL as a dissipative bath, we introduce a three-wave parametric coupling between the system and the bath. As in the case of JPC, we can drive the 'gain' and 'conversion' process to tune the rate that the system thermalizes to the bath. As we are using the transmon

qubit as the system, we are in fact controlling the thermalization process of a microwave photons. Then, the ability of setting the thermal state distribution of such system is as if we have effective created a chemical potential for the system, which does not exist for a natural photonic system. This theory is worked out in great detail in Chapter IV, and experimental data are shown in Chapter VI.

G. Measurement back-action and weak measurement protocol

A quantum measurement will perturb the state of the qubit. This perturbation is known as the back-action of the measurement. For a measurement performed with ideal quantum hardware, the qubit will still be in pure state after the measurement, as the evolution of the state can be perfectly tracked from the measurement record. As we introduced in Sec. I.C, in order to measure a qubit in the state $|\psi\rangle = c_g |g\rangle + c_e |e\rangle$, we send a coherent light probe signal to the qubit-cavity system. After the probe signal traverses the cavity, the coherent light and the qubit form a new entangled state together: $|\Psi\rangle = c_g |g\rangle |\alpha_g\rangle + c_e |e\rangle |\alpha_e\rangle$. Here $|\alpha_{g,e}\rangle$ is the transmitted coherent state when the qubit is the ground or excited state, respectively. This new entangled state will serve as the pointer state of the system and will be sent through a quantum-limited amplifier so the signal can be received and processed at room temperature. Typically, in our lab a phase-preserving amplifier (JPC) is used.

The effect of the back-action of a phase-preserving measurement is illustrated in Fig. 12. Each shot of outcome will contain the measurements of both quadrature of the output mode, which we denote as (I_m, Q_m). This I-Q pair will be used to determine the state of the qubit after the measurement and as been pointed out in Ref [54, 106], it contains all the information to track the state evolution of the qubit (provided the measurement is lossless). That is, we can reconstruct the Bloch vector for the qubit after the measurement given the measurement result (I_m, Q_m). However, in an actual experiment, there will also be losses. Therefore, we introduce the concept of measurement efficiency η as in Eq. I.1 as a way to measure how much quantum information is collected by the observer. As an example, for a qubit that is initially prepared in the state $|+y\rangle = (|g\rangle + |e\rangle)/\sqrt{2}$, the final qubit Bloch vector

(x_f, y_f, z_f) is a function of measurement outcome (I_m, Q_m)(for simplicity we will neglect the qubit decoherence and the all losses before the quantum-limited amplifier). Hatridge *et al.* [54] find:

$$x_f(I_m, Q_m) = \mathrm{sech}(\frac{I_m \bar{I}_m}{\sigma^2})\sin[\frac{Q_m \bar{I}_m}{\sigma^2} + \frac{\bar{Q}_m \bar{I}_m}{\sigma^2}(\frac{1-\eta}{\eta})]e^{-\frac{\bar{I}_m^2}{\sigma^2}(\frac{1-\eta}{\eta})} \tag{II.51}$$

$$y_f(I_m, Q_m) = \mathrm{sech}(\frac{I_m \bar{I}_m}{\sigma^2})\cos[\frac{Q_m \bar{I}_m}{\sigma^2} + \frac{\bar{Q}_m \bar{I}_m}{\sigma^2}(\frac{1-\eta}{\eta})]e^{-\frac{\bar{I}_m^2}{\sigma^2}(\frac{1-\eta}{\eta})} \tag{II.52}$$

$$z_f(I_m, Q_m) = \tanh(\frac{I_m \bar{I}_m}{\sigma^2}) \tag{II.53}$$

where $\bar{I}_m$, $\bar{Q}_m$ and σ are the center and standard deviation of 2D Gaussian distribution corresponding to the coherent measurement pulse. The above results indicate that by observing the measurement back-action, we can obtain the measurement efficiency as a parameter to assess the quality of the measurement apparatus.

We use the pulse sequence shown in Fig. 13 to obtain the measurement back-action. We first use a strong projective measurement and record the data from which we will post-select to pick out the runs with qubit found in the ground state. Next, we rotate the qubit into the $|+y\rangle$ state with a $\pi/2$ pulse. Then, we deliberately apply a measurement with a strength weaker than the projective measurement, and record the result. Finally, we do full tomography on the qubit state to determine its Bloch components with another projective measurement. To get the back-action result for a certain weak measurement outcome (I_m, Q_m), the Bloch components of the qubit $(\langle x\rangle_c, \langle y\rangle_c, \langle z\rangle_c)$ is calculated from the tomography result conditioned recording that specific weak measurement result in a finely-binned histogram.

A theoretical result is shown in Fig. 14. When the measurement strength is weak, the ground and excited state distribution largely overlap with each other. Their separation will increases as the measurement strength (or SNR) increases. For the strong measurement case, by definition the two distributions are well separated. The conditional tomography data $\langle X\rangle_c$, $\langle Y\rangle_c$ and $\langle Z\rangle_c$ versus measurement outcome $(I_m/\sigma, Q_m/\sigma)$ is also shown in the figure. When the measure strength is weak, the qubit state receives minimal perturbation from the measurement, with the outcomes corresponding most probably to Bloch vectors along the $+y$ direction. In practice, any outcome is possible, but in practice outcomes which are very

improbable require too many measurements to be practically observed, and so we truncate the theory and set all points to gray which are more than XX σ away from the centers of the two gaussian blobs. We can also see the gradients in $\langle X \rangle_c$ along the Q_m axis and $\langle Z \rangle_c$ along the I_m axis, indicating the back-action of the measurement. In an actual experiment, after getting these back-action data with this weak measurement protocol, by looking at the conditional tomography results and fitting the x- and y- back action for outcomes where the z-component is zero (here $I_m = 0$) to the theory, we can extract the measurement efficiency as a single fit parameter by comparing the frequency of oscillation (which we can extract from the histogram) to the amplitude of oscillations using the theory expression above.

When the measurement is strong, the qubit is then projected to $+z$ direction for positive I_m values and $-z$ direction for negative I_m values. The oscillations in $\langle X \rangle_c$ and $\langle Y \rangle_c$ (where the z back-action is weak), are still visible very near $I_m = 0$ but are both very improbable (hence nearly being pinched off by our chosen cutoff in the graphs) and very quickly varying which will be almost impossible to detect in a practical lossy environment with a reasonable number of repititions of the protocol. Note here that we have set a relatively 'weak' projective measurement to make this effect more visible, in practice we would like SNRs which are even higher.

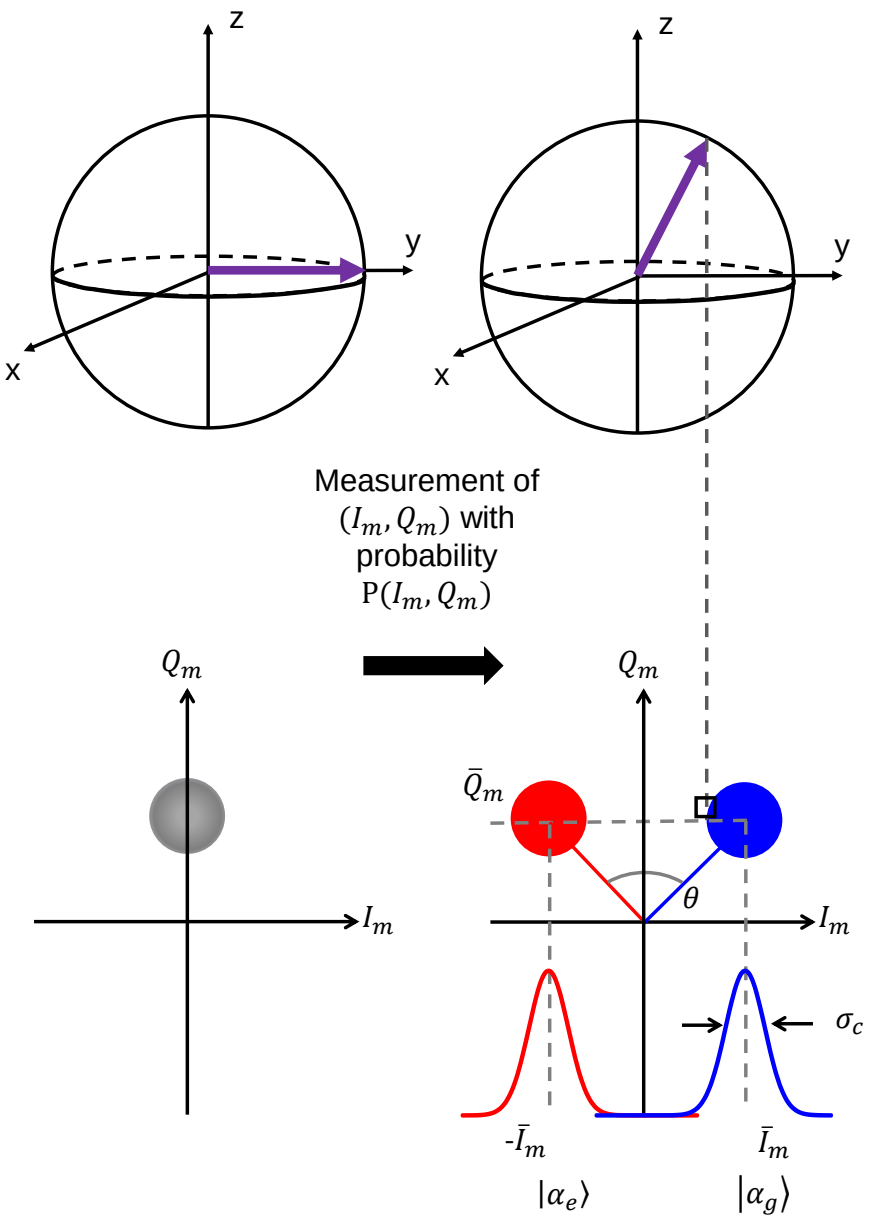

Figure 12: **Bloch sphere representation of measurement back-action.** This graphic is adapted from [54]. Bloch sphere representation of the back-action on the qubit state of a phase-preserving measurement. After a measurement with outcome (I_m, Q_m), the qubit can be found in the state $S_f = (x_f, y_f, z_f)$, with I_m encoding information of the projection of the qubit along z direction. Q_m contains the information of the other component of the back action, which is parallel to $z \times S_i$.

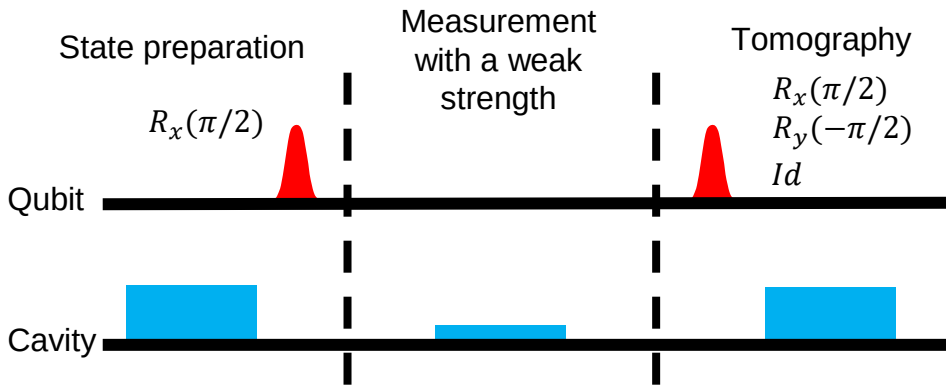

Figure 13: **Pulse sequence for determining the measurement back-action.** The first projective measurement is used to post-select the data for state prepration. The second measurement strength is changed linearly in amplitude. Conditional mpas of $\langle X\rangle_c$, $\langle Y\rangle_c$ and $\langle Z\rangle_c$ versuse measurement outcome (I_m/σ, Q_m/σ) is constructed from the second and third measurement.

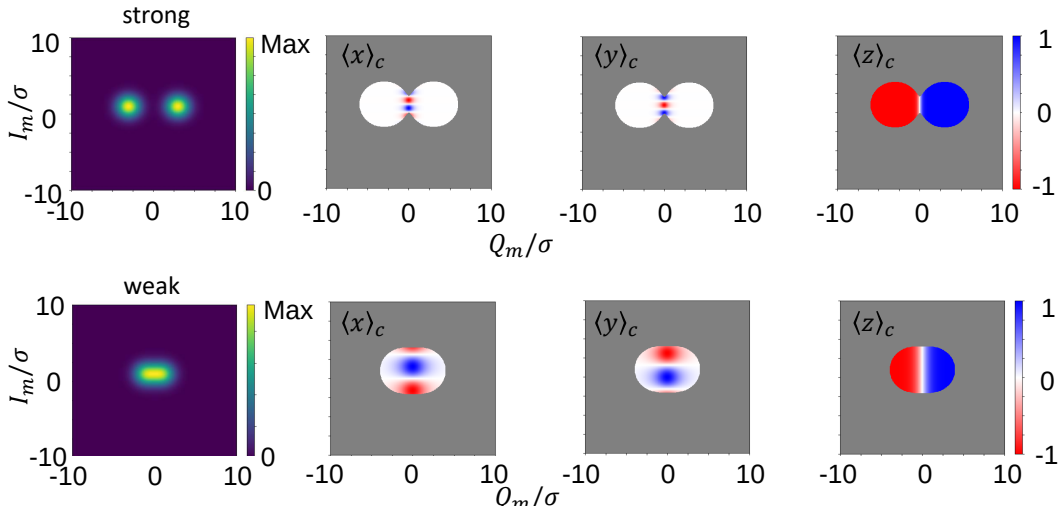

Figure 14: **Theory result for the measurement back-action.** Theory results for the back-action of a 'weak' ($\bar{I}_m/\sigma = 1.0$) and 'strong' ($\bar{I}_m/\sigma = 3.0$) measurement. The three histograms are showing $\langle X\rangle_c$, $\langle Y\rangle_c$ and $\langle Z\rangle_c$ versus the associated (I_m/σ, Q_m/σ) bin.

III. Qubit measurement with two-mode squeezed light

A. Overview

Fault-tolerant quantum information processing with flawed qubits and gates requires highly efficient, quantum non-demolition (QND) qubit readout. In superconducting circuits, qubit readout using coherent light with fidelity above 99% has been achieved by using quantum-limited parametric amplifiers. However, further improvement of such measurement is fundamentally limited by the vacuum fluctuations of the coherent light used for readout. In this chapter, we demonstrate the use of two-mode squeezed (TMS) light instead of coherent light and phase-preserving amplifier combined into an interferometer for dispersive qubit readout, as proposed in Ref. [99]. This measurement scheme is based on a Mach-Zehnder interferometer with active non-linear beam splitters which is commonly known as a SU(1,1) interferometer [107]. Such a measurement scheme implemented in our experiment shows a 44 % improvement in power SNR compare to the usual coherent light readout. Using the weak measurement protocol introduced in CH. II, we also investigate the back-action of the two-mode squeezed light measurement and and found, surprisingly, that tuning the interferometer to be as unprojective as possible was associated with an increase in the quantum efficiency of our readout relative to the optimum setting for projective measurement.

This chapter is organized as follows: we begin in Section III.B and Section III.C by introducing the experimental setup and the basic parameters of our sample. Then in Section III.D, we demonstrate the generation and interference of TMS light using our setup. Next in Section III.E, we show that with TMS light the output noise of the system is qubit state dependent and how we can use this to measure qubit. In Section III.F, we demonstrate how to take advantage of the TMS light to implement a measurement with higher power SNR than the usual coherent light measurement. In Section III.G, we use the weak measurement technique to investigate the back-action of the measurement. Finally in Section III.H, we give a brief conclusion of this chapter and some outlooks for this project.

B. Experimental setup

1. Cryogenic setup

In this experiment, we form an active interferometer with two nominally identical JPCs, the 'entangler' and 'analyzer', by connecting their signal and idler ports [98], as shown in Fig. 15. Uncorrelated vacuum noise enters the interferometer via the inputs of the entangler JPC, which transforms them into highly correlated, two-mode squeezed vacuum traveling along the two arms of the interferometer that we will describe in details in the next section. These two paths recombine and interfere with each other in the analyzer JPC, generating outputs controlled by the gains and relative pump phase of the two JPCs. The input is doubly amplified with zero relative pump phase between the two JPCs (yielding a net amplifier with power gain G_eG_a), while a π relative pump phase will cause the analyzer JPC to de-amplify the output of the entangler JPC. In the absence of loss and added noise, the output of the interferometer will return to uncorrelated vacuum if the gains of the two JPCs are matched and their pump phases are different by π.

We use the interferometer to read out a qubit by interrupting the upper arm with a microwave cavity, which in turn is dispersively coupled to a transmon qubit, as shown in Fig. 15. To achieve a better SNR than qubit readout with coherent light input and phase-preserving amplification (CS + PP), the dispersive phase shift due to interaction with the qubit-cavity system must be either close to zero or π, which correspond to the qubit-cavity dispersive shift χ being much smaller or larger than the cavity linewidth κ [99]. In our experiment, we design the quit-cavity system to be in the small dispersive shift regime with $\chi/\kappa = 0.22$ which is favorable for fast readout.

Although the noise of the interferometer itself can read out the qubit for many combinations of entangler and analyzer gain and relative phase, high SNR readout requires a coherent drive to be applied to the system. The original proposal called for displacing the input to the upper arm of the entangler [99]; however, in this scenario the signal is both amplified and partially transmitted down both arms of the interferometer, so that there is interference in both the output signal and noise. See how the signal changes in Fig. 19.

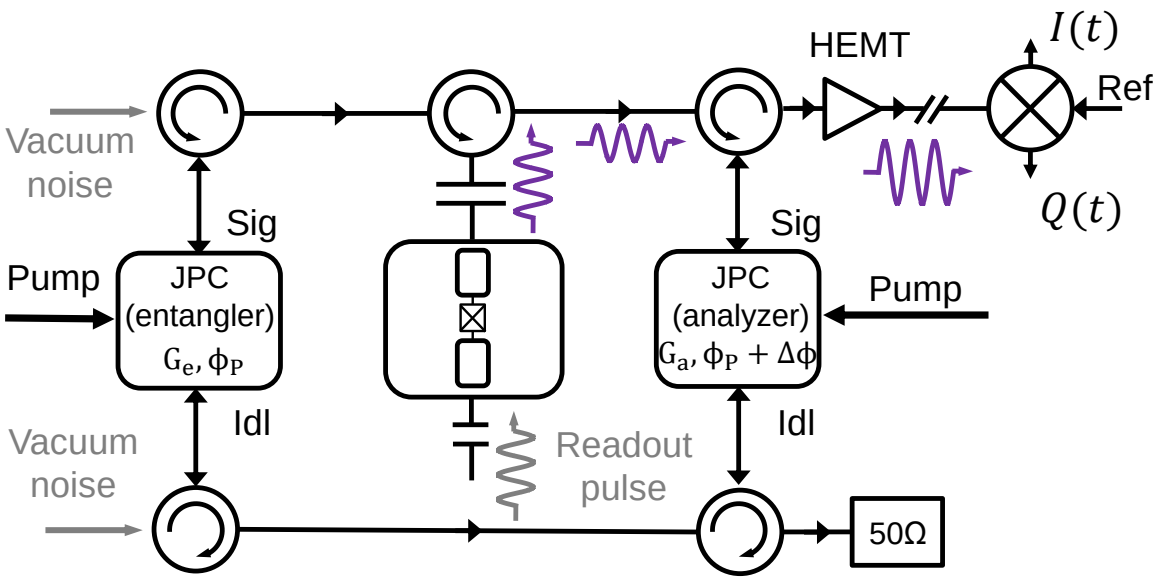

Figure 15: **Schematic of the experiment setup.** Two nominally identical JPCs, entangler and analyzer, are connected by their signal (Sig) and idler (Idl) ports respectively with circulators and superconducting cables to form an interferometer. The unused ports on the circulators are terminated in cold 50 Ω loads which provide quantum vacuum noise to the entangler, and a dump for the unused signal on the lower arm of the interferometer. The upper arm of the interferometer is interrupted by a 3D transmon qubit-cavity system. The qubit measurement pulse is sent into the cavity via its weakly coupled port without going through both arms of the interferometer which enables the switching between the two-mode squeezed light readout and coherent light readout *in situ* by turning on and off the pump of the entangler JPC. The signal is subsequently further amplified by a cryogenic HEMT and demodulated and recorded at room temperature.

This greatly complicates fair comparison with CS + PP readout, and so in our experiment we drive our readout through a second, weakly coupled port in the microwave cavity. The readout signal thus does not interfere, and experiences the same gain (from the analyzer only) in both our TMS and CS + PP readout. In this case, we squeeze only on the noise, with a degradation/enhancement of SNR corresponding to a larger/smaller output noise,

respectively.

In addition to the set up shown in the Fig. 15 that is cooled down to 20 mK, we also show the rest of experimental setup in Fig 16. Fridge input lines carrying signals from room temperature to the system are attenuated and filtered with homemade lossy Eccosorb filters. Room temperature electronics, which include microwave generators, IQ mixers and an arbitrary waveform generator, are used to produce microwave pulses to drive the qubit and cavity. Both the qubit and cavity drives are sent into the system through the qubit-cavity input line, which connects to the weak port of the cavity. The JPCs are pumped with Keysight microwave generator. The output signal from the TMS interferometer is amplified by a chain of low noise cryogenic and room temperature amplifiers before been down-converted, digitized and demodulated with a room-temperature reference copy.

2. Pump leakage cancellation

Another practical issue we have encountered during the experiment is the leakage of pump signal. Due to the design of our JPC, applied pump tones preferentially leave from the signal and idler ports. Similarly, a pump tone can enter a JPC through its signal and idler ports (though in practice we apply pump tones only to the pump port). Thus, in our experiment, a fraction of the pump signal from the first JPC (entangler) always leaks into the second JPC (analyzer) through the arms of the interferometer. The reverse process is also possible, depending on the directionality of our interferometer at the pump frequency. Given that the two JPCs are biased so that their mode frequencies are matched and the second JPC is operated in the high gain (20 dB) regime, this pump leakage can cause large gain variation on the second JPC (gain variation as large as 15 dB was observed).

To eliminate this unwanted effect, we deliver the pump signals to the JPCs through a circuit shown in Fig. 17 similar to the one used in Ref. [98]. In this circuit, the entangler pump is split and fed to two I/Q mixers which provide both JPC pumps. The analyzer's pump signal is a combination of a the desired analyzer pump and a phase and amplitude shifted copy of the entangler pump which cancels its leakage in the analyzer JPC. Experimentally, we nulled the leakage by varying the analyzer pump phase and identifying the correction

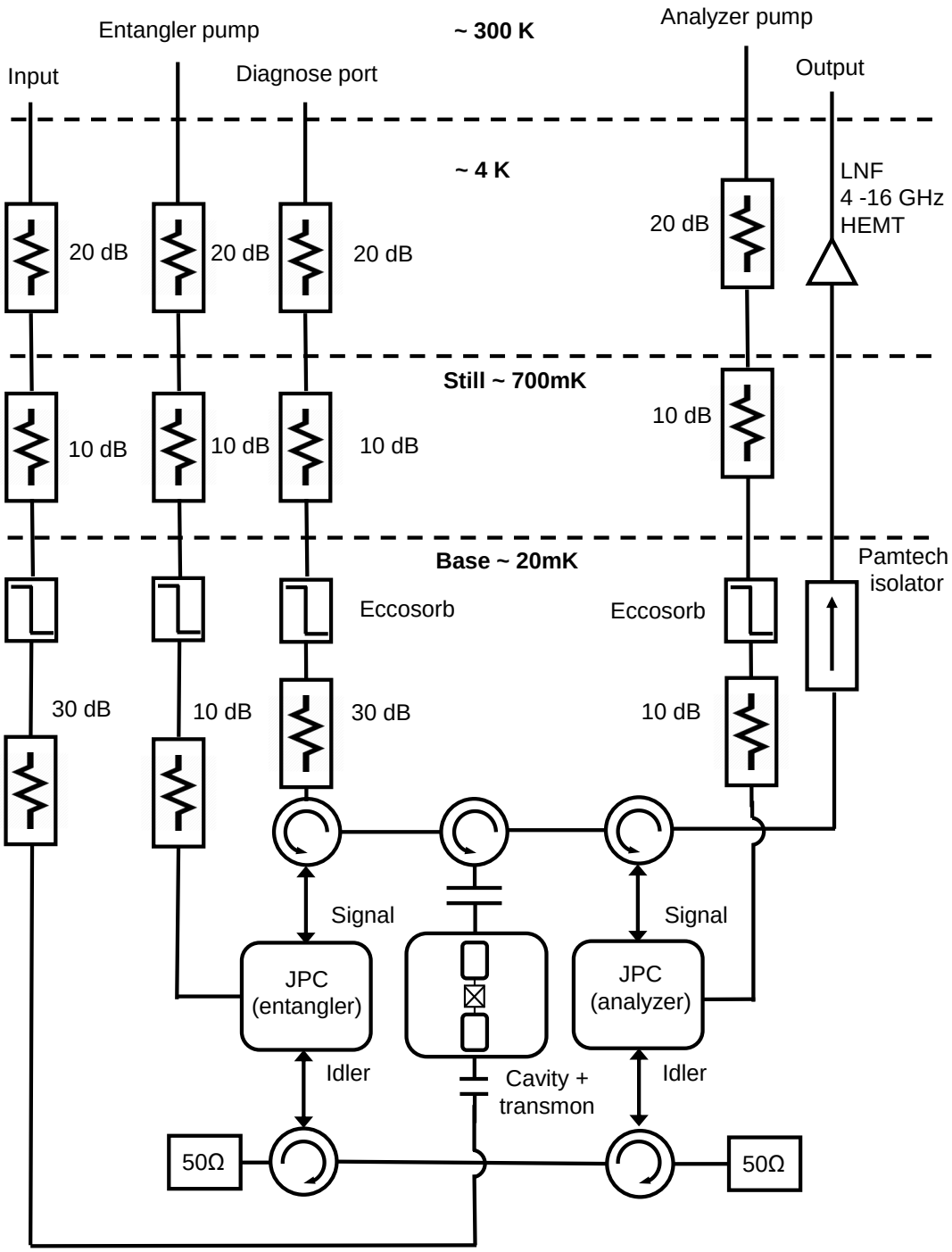

Figure 16: **Wiring diagram of the cryogenic microwave measurement setup.**

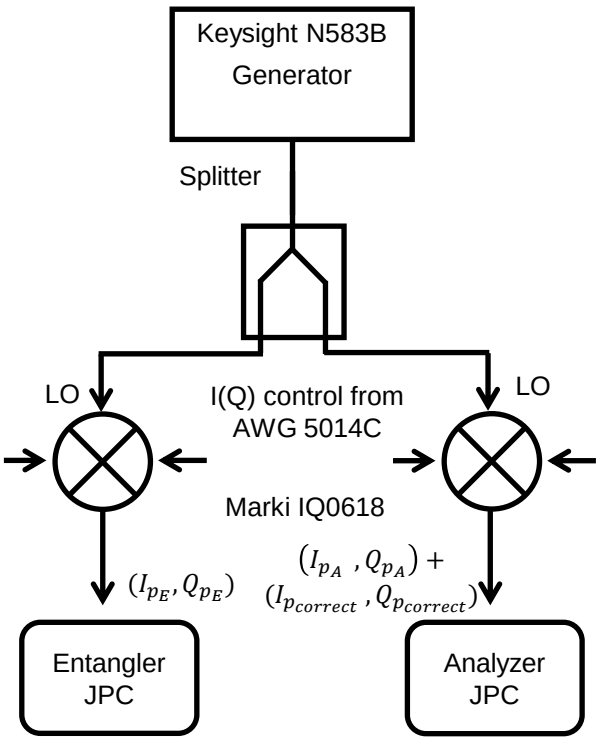

Figure 17: **Wiring diagram of room temperature setup for canceling the pump leakage.** The output of a single generator (Keysight N583B) is split and fed to two I/Q mixers which control the two JPC pumps. The Signal applied to the analyzer JPC is the sum of the desired pump and a correction designed to cancel leakage due to the entangler JPC pump. The use of a single generator has the additional benefit of stabilizing the relative phase of the two pumps, as a drift in phase of the generator affects both pumps equally.

factor where analyzer gain is insensitive to the presence or absence of the entangler pump. Another way of eliminating the pump leakage to the analyzer could be to add low-pass filters on both arms of the interferometer. However, this would introduce additional loss to the interferometer and degrade its performance. Therefore, we chose the active method described here. More, to prove that this effect is due entirely to pump leakage, and not two-mode squeezing effects in the interferometer, we verified the presence of pump leakage and our cancellation scheme with the up-stream, entangler JPC tuned far away in frequency

with flux.

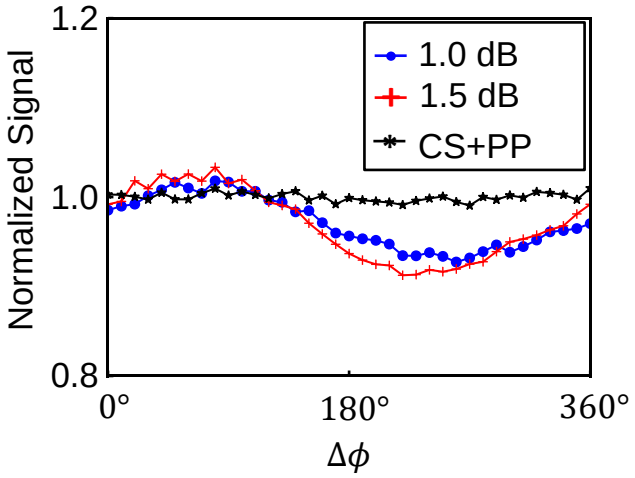

Figure 18: **Normalized signal strength of qubit readout with coherent light and displaced two-mode squeezed vacuum.** The strength of the signals are normalized by the average signal strength of the coherent light readout (CS + PP). Data shown here are for entangler gain $G_e = 1.0$ dB (blue dot), 1.5 dB (red cross) and 0 dB (CS + PP) (black star). The analyzer gain is kept constant at $G_a = 20$ dB.

To quantify how well the cancellation process works, we measured the output signal strength as a function of the relative pump phase for coherent light readout (CS+PP), which should have no pump variation, and displaced two-mode squeezed vacuum readout with the same cavity drive strength. Fig. 18 shows the output signal strength normalized with respect to the average output signal strength of coherent light readout. For displaced two-mode squeezed vacuum readout, the output signal strength varies at most by -8%, which corresponds to a variation of 0.35 dB of the 20 dB gain of the analyzer. Note that this shift is negative, and decreases our SNR, so that the net observed enhancement in readout SNR is entirely due to a reduction in output noise and even larger than the overall SNR improvement suggests.

C. Sample parameters

The cavity in our experiment is a 3D aluminum coaxial post cavity with a resonance frequency of $\omega_c/2\pi = 7.447$ GHz, coupling quality factors of $Q_{strong} = 752$ on the strong port, and $Q_{weak} \sim 1,000,000$ on the weak port. Therefore, the cavity linewidth seen from the strong port is $\kappa/2\pi = 9.9$ MHz. The superconducting qubit is a 3D transmon qubit made by commonly used Dolan bridge technique with ground to excited state transition frequency of $\omega_{ge}/2\pi = 4.102$ GHz, anharmonicity $\alpha = 180$ MHz, and a qubit-cavity dispersive coupling strength of $\chi/2\pi = 2.2$ MHz . This qubit has a T_1 of 18.2 μs, and T_{2R} of 4.4 μs (T_{2E} is 4.6 μs). The cavity is placed in an aluminum shield that is inside a μ-metal cryoperm shield. The whole system is wrapped in mylar.

The cavity is used to perform dispersive measurement on the qubit. The strong port is used to have the qubit-cavity system strongly couple to the interferometer, so that the noise features seen the qubit are determined by the TMS noise. The weak port (whose coupling Q is much higher and therefore much harder to send signal through) is used to send in the control and measurement pulses to the system.

D. Interference of two-mode squeezed light with JPC

An important signature of the TMS light is the coherent interference between the two parts of the light generated by the entangler. The effect of this interference can be both seen in the change of gain and output noise level of the system as a function of the phase difference between the pump signals of the entangler and analyzer. To understand this, we can look at the relation between the input and output mode (a and b) of a phase-preserving amplifier (e.g a JPC):

$$a_{out} = S^\dagger a_{in} S = \cosh(r) a_{in} + e^{i\phi_p} \sinh(r) b_{in}^\dagger \tag{III.1}$$

$$b_{out}^\dagger = S^\dagger b_{in}^\dagger S = \cosh(r) b_{in}^\dagger + e^{-i\phi_p} \sinh(r) a_{in} \tag{III.2}$$

When two identical JPCs are connected with their signal and idler ports respectively, it is straightforward to calculate the scattering parameters for the combined system using the equations above twice. For example, the transmission gain from the signal port of the 'entangler' JPC to the signal port of the 'analyzer' JPC S_{aa} can be written as:

$$S_{aa} = \cosh(r_E)\cosh(r_A) + e^{i\Delta\phi}\sinh(r_E)\sinh(r_A) \tag{III.3}$$

where we can see the amplitude of S_{aa} will vary with the relative pump phase $\Delta\phi$. Especially, when two JPCs has a matched gain ($r_E = r_A = r$) and a relative pump phase difference of π, the total gain of the system will become $\cosh^2(r) - \sinh^2(r) = 1$, indicating that the output signal power will be the same as the input signal. This interference pattern feature demonstrates this important signature of a phase preserving amplifier (e.g. JPC), that both output modes are connected with both input modes, which is a requirement from quantum mechanics. Therefore, light in the two modes of the TMS light are not independent of each other, but tightly correlated and thus can interfere with each other.

Figure. 19 shows data measured using a vector network analyzer as a function of the relative pump phase for $G_e = 0.67$ dB, 9.15 dB and a fixed analyzer JPC gain of $G_a = 10$ dB. By fitting these data with a modified version of Eq. III.3 which includes losses on both arms [98], we can extract the ratio of the transmission efficiencies of the upper and lower arms, which is found to be 0.9. We believe this imbalance in transmission is mostly due to the insertion loss of the extra circulator on the upper arm that connects to the qubit-cavity system. Given the stated loss of 0.2 dB per pass in the circulator, this would give 0.4 dB (transmission coefficient of 0.91) of additional loss on the upper arm, which is consistent with the loss ratio inferred from our data.

The normalized output noise level σ^2_{out} can be also calculated from Eq. III.3, which gives [98]:

$$\sigma^2_{out} = \cosh(2r_E) + \sinh(2r_E)\tanh(2r_A)\cos(\Delta\phi) \tag{III.4}$$

We measure the output noise voltage at the signal port of the analyzer while sweeping the relative phase ($\Delta\phi$) between the two pump tones for different squeezing strength, G_e, on the entangler JPC. The gain of the analyzer JPC, G_a, is kept constant at 20 dB. Unlike measuring the S-parameters value using a vector network analyzer, the noise is measured

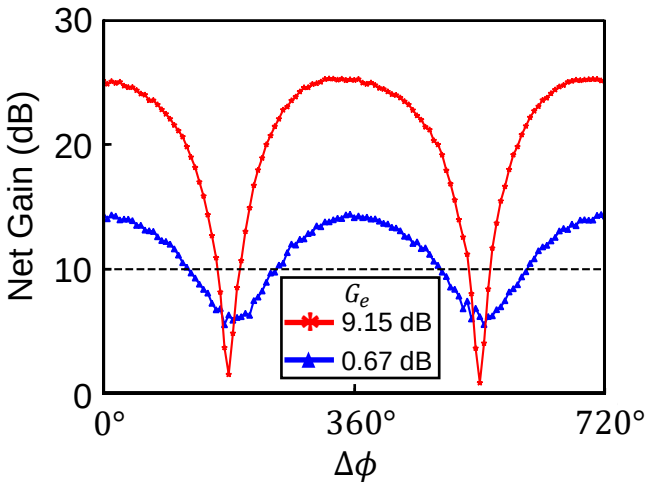

Figure 19: **Transmission measurement of the S parameter S_{aa} of the TMS interferometer as a function of the relative pump phase**. The gain of the analyzer JPC, G_a, is fixed to be 10 dB during the measurement (to avoid gain saturation for large entangler gain settings) as shown by the black dashed line. The blue triangle and red star trace corresponds to the different gain of the entangler JPC.

using an arbitrary waveform generator and a digitizer. For each shot of the measurement, the qubit is prepared in the ground state by post-selecting the result of an initial, projective measurement. After initializing the qubit state, we wait for 10 cavity lifetimes before recording the output voltage of the system for a 660 ns period, from which we obtain the quadrature voltage values (I_m, Q_m) of the noise. For a given squeezing strength, at each relative pump phase, the same measurement is repeated 50,000 times and the outcomes are plotted in the form of a 2D histogram. Fig. 20(a) shows the line cuts along $Q_m = 0$ of the 2D histograms of the measurement outcomes with the entangler off, $G_e = 0$ dB (CS + PP), versus entangler on with $G_e = 1.5$ dB at two different relative pump phases. All the curves are normalized so that the area under the curve is 1. Comparing to the unsqueezed input (CS + PP), the output noise voltage of the two-mode squeezed vacuum changes from larger

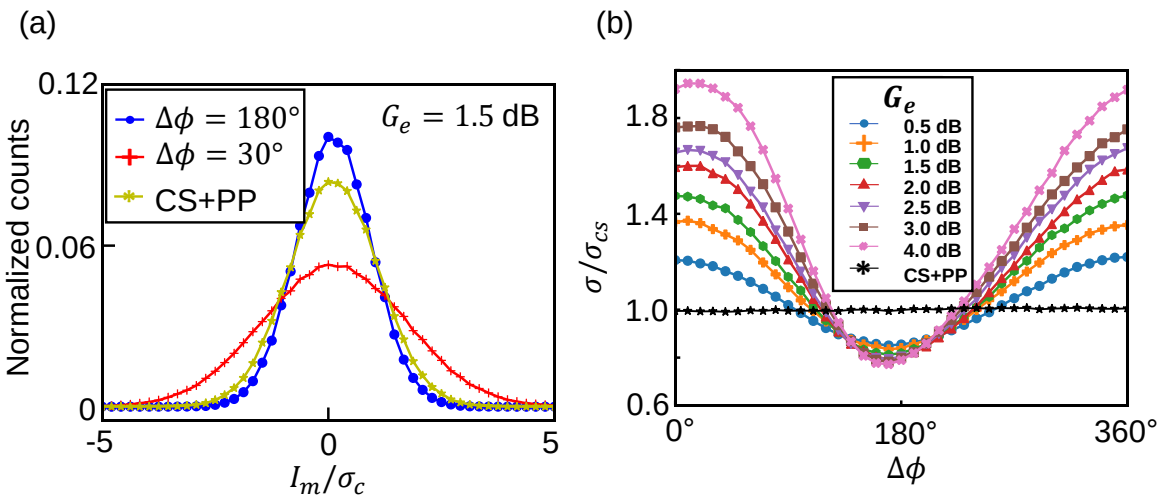

Figure 20: **Two-mode squeezed vacuum.** (a) Normalized 1D Gaussian distribution of noise measurement result for the two-mode squeezed vacuum at featured relative pump phase point with a $G_e = 1.5$ dB. The red cross and blue dot curves are obtained by applying a line cut along $Q_m = 0$ of the 2D histograms at relative pump phase point that gives the highest and lowest noise level respectively. The curve for the case of coherent light (yellow star) is also shown for comparison. (b) Normalized standard deviation of output noise voltage of two-mode squeezed vacuum as a function of relative pump phase $\Delta\phi$ at different entangler gain G_e. The standard deviation of noise voltage at each relative pump phase and entangler gain is obtained by fitting a histograms of 50, 000 repeated measurement results (see supplementary) to a 2D Gaussian distribution. The black star line shows the noise level of the coherent vacuum input as a reference while the other colors each represents a different gain for the entangler JPC. During the measurement, the analyzer gain is $G_a = 20$ dB.

to smaller than that of the amplified vacuum as the two pumps go from in phase to out phase with each other, which demonstrates the correlation between the two parts of the two-mode squeezed vacuum traveling on the two arms of the interferometer.

By fitting the histogram to a 2D Gaussian distribution, the standard deviation of the measurement outcome (σ_I, σ_Q) can be extracted. In Fig. 20(b), we plot the standard devia-

tions of the noise measurement outcomes with respect to relative pump phase for entangler gain ranging from 0 dB to 4 dB (as $\sigma_I \simeq \sigma_Q$ we plot their average). For easier comparison, all the data shown in this figure are normalized by the average standard deviation of the measurement outcome of $G_e = 0$ dB, which is the noise for standard CS + PP qubit measurement. We can see that the output noise level of the two-mode squeezed vacuum oscillates with the relative pump phase. In particular, there exists a range of relative pump phase within which it goes below that of the amplified unsqueezed vacuum. This oscillatory pattern clearly shows the existence of coherent interference between photons in the two arms of the interferometer. It also shows that the output noise level of the two-mode squeezed vacuum can be controlled by the relative pump phase. As the gain of the entangler increases, the suppression of the noise becomes stronger, but at the same time the phase range for noise suppression becomes smaller. This sets the limit for SNR improvement attainable in a given qubit-cavity system. We note that similar result has previously been observed in a setup with only two JPCs and no qubit [98]. This noise reduction is due to the destructive interference between the light in both arms of the interferometer and it points the way to use TMS light for a better qubit measurement.

E. Qubit readout with two-mode squeezed vaccum

In order to utilize the two-mode squeezed vacuum for qubit readout, we first study the effect of the dispersive qubit-cavity phase shift on the interferometer. To do so, we repeat the measurements from Fig. 2 with $G_e = 2.0$ dB and the qubit now being prepared either in the ground or excited state, and the results are shown in Fig. 21(a). The noise behavior of two-mode squeezed vacuum for qubit in ground and excited states are very similar, with a relative phase shift of 40° which is due to the qubit-state dependent dispersive phase shift on photons traveling on the upper arm of the interferometer. For a given relative pump phase, this extra phase shift creates a qubit-state dependent output noise power. This means that, except for the two relative phases ($\Delta\phi = 190°$ and 330°) where the output noise is identical for both qubit states , the noise of the interferometer can measure/dephase the qubit state

without any input drive applied to the cavity. This is very different from CS + PP readout where the cavity must be driven to perform measurement, and the amplifier being on or off should not affect the qubit's dephasing rate.

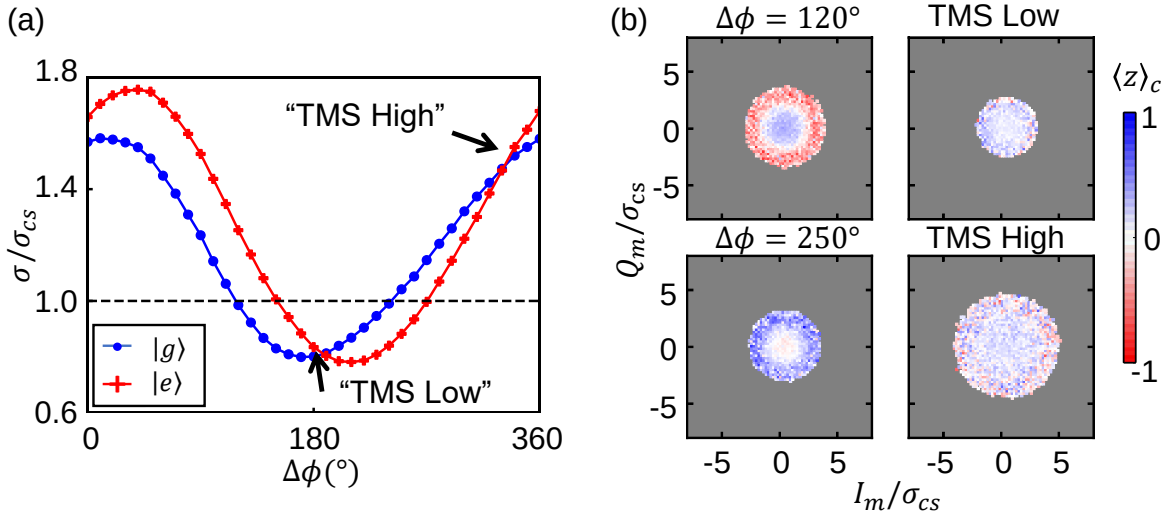

Figure 21: **Qubit readout with two-mode squeezed vacuum.** (a) Normalized standard deviation of output noise voltage for two-mode squeezed vacuum input on the analyzer as a function of relative pump phase and qubit state. The black dotted line shows the standard deviation when the input of the analyzer is the coherent (unsqueezed) vacuum. Blue and red curves represent results for two-mode squeezed vacuum noise recorded when the qubit is in $|g\rangle$ and $|e\rangle$ state respectively. (b) Conditional tomography data for the z component of the qubit Bloch vector after we record the output noise for 660 ns at different relative pump phases. The qubit is prepared in the state of $(|g\rangle + i\,|e\rangle)/\sqrt{2}$. The entangler gain is $G_e = 2.0$ dB and the analyzer gain is $G_a = 20$ dB.

To demonstrate this 'two-mode squeezed vacuum' readout in the interferometer, we modify our measurement protocol by changing the initial state of the qubit to $(|g\rangle + i\,|e\rangle)/\sqrt{2}$, and adding a strong measurement after recording the noise output voltage to determine the final state of the qubit. The pulse sequence is shown in Fig. 22. As in References [54, 108], we construct a histogram where each pixel contains the average of all final measurement results of the z-component of the qubit state Bloch vector conditioned on receiving a particular (I_m,Q_m) voltage in the second (noise) measurement. Fig. 21(b) shows these conditional

z-axis tomography results at four different relative pump phases: $\Delta\phi = 120°$ and $250°$, at which the difference between the output noise power for qubit in ground and excited state is the largest, and $\Delta\phi = 190°$ and $330°$ at which the output noise power for qubit in ground and excited state are the same. At $\Delta\phi = 120°$, we clearly see a 'Bullseye' pattern, with the qubit found to be in $|e\rangle$ if the recorded noise voltage is large, and in $|g\rangle$ if the recorded noise voltage is small. A similar result is also seen at $\Delta\phi = 250°$, with the correspondence between the noise voltage amplitude and qubit state reversed. These results show that two-mode squeezed vacuum in our inteferometer, unlike unsqueezed vacuum, can entangle with the qubit state. An observer with a power meter could perform a (poor fidelity) readout of the qubit simply by measuring how much noise the circuit emits. This also implies that powering the entangler and analyzer will generate continuous qubit dephasing for these bias points. In contrast, at $\Delta\phi = 190°$ and $330°$ where the output noise levels are the same for different qubit states, and so, similarly to unsqueezed vacuum, no information about the qubit can be inferred from the circuit's noise output. We will focus in the next two sections of this paper on experiments at the two 'matched' noise points, which we refer to as 'TMS High' and 'TMS Low' for the point with larger and smaller matched noise, respectively.

F. SNR improvement with displaced two-mode squeezed vacuum

In standard dispersive qubit readout, a coherent microwave pulse containing several photons is used to extract the qubit state information [54, 109]. We are now going to show that SNR of such measurements can be improved by replacing the coherent light with two-mode squeezed light of the same strength. The SNR in our experiment is defined as:

$$\mathrm{SNR} = \frac{(I_c^g - I_c^e)^2 + (Q_c^g - Q_c^e)^2}{\sigma_g^2 + \sigma_e^2} \tag{III.5}$$

where $(I_c^{g(e)}, Q_c^{g(e)})$ is the center of the measurement result distribution when the qubit is in ground (excited) state and $\sigma_{g(e)}$ is the corresponding standard deviation. To determine the SNR, we prepare the qubit in the ground and excited state separately, and then perform the readout by sending a coherent probe signal through the cavity from its weak port. Given

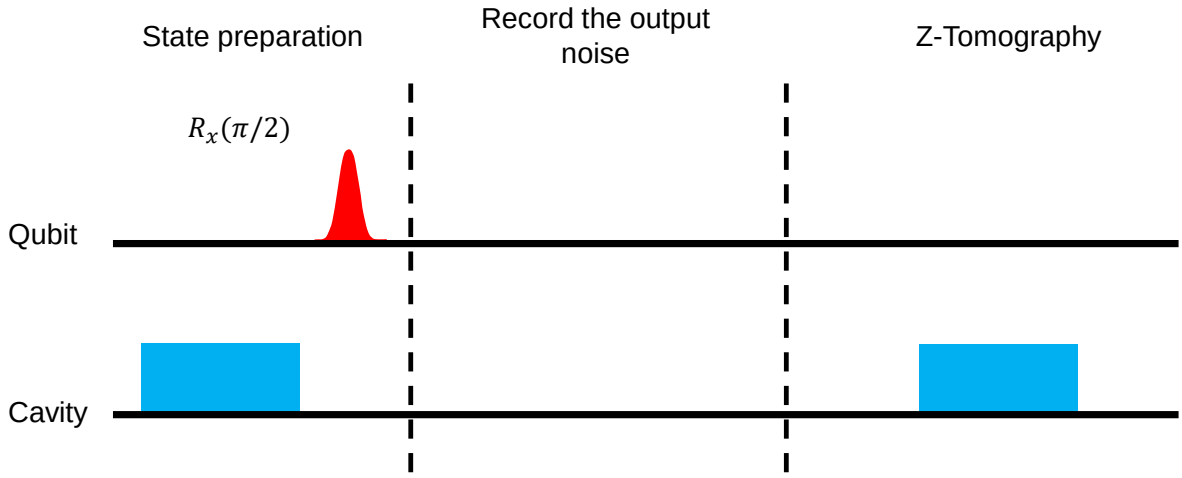

Figure 22: **Pulse sequence for quantifying the back action of noise measurement.** This pulse sequence consists three stages of qubit and cavity manipulation. The first stage is state preparation, during which the qubit is first projected to the state $|g\rangle$ by a strong measurement (blue box) and post-selection, and then rotated to the state $(|g\rangle + i\,|e\rangle)/\sqrt{2}$ by a $R_x(\pi/2)$ pulse (red Gaussian). The second stage is noise measurement, during which the qubit state is measured by only recording the output noise of the system. In the third and final stage a qubit z-component tomography is performed by a strong measurement (blue box) pulse.

that the coupling strength of the strong port is much greater than that of the weak port ($Q_{weak} \gg Q_{strong}$), quantum fluctuations of the field inside the cavity will be set by the two-mode squeezed vacuum present at the strong port. For fair comparison with standard CS + PP readout, we drive the system from the weak port in all cases, rather than driving the entangler amplifier as proposed in [99]. This has the advantage that there is ideally no interference in the amplitude of our signals, and a uniform displacement of the cavity in all measurements (see Fig. 18), and so any change in SNR will be solely due to changing the quantum noise in the interferometer, rather than larger or smaller displacements drives

applied to the cavity.

In Fig. 23, we show the SNR of the dispersive readout with displaced two-mode squeezed vacuum as a function of relative pump phase for different entangler gain. The data is normalized to the average SNR of coherent light ($G_e = 0$ dB) readout with the same strength. Improvement in SNR, as large as 44%, is observed for relative pump phase in the range of 140° to 240° over a wide range of entangler gain. In this range, the signal is actually 8% *smaller* than in CS+PP case (see Fig. 18), and so the entirety of the improvement in SNR is due to suppressed noise in the interferometer's output. Such an improvement in SNR would translate into a suppression of readout error rate that is due to the finite SNR by a factor of 5 when starting out with an error rate of 1% with coherent light, which is normally achievable in superconducting qubit systems.

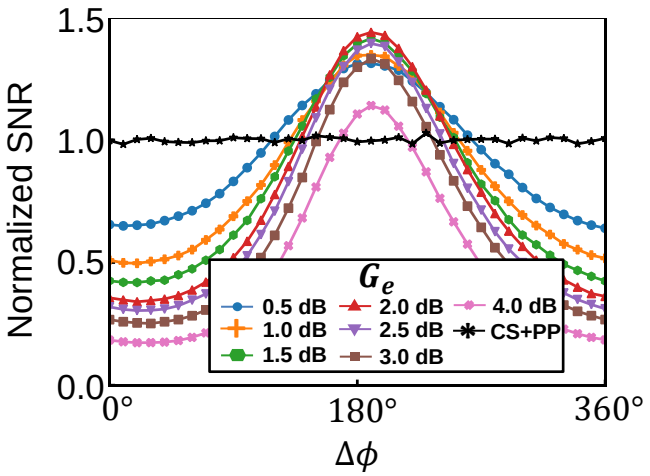

Figure 23: **SNR of qubit readout with coherent light and displaced two-mode squeezed vacuum.** Normalized power SNR for qubit readout with coherent light, and with displaced two-mode squeezed vacuum at different squeezing strength (G_e) as a function of relative pump phase. The SNR is calculated according to Eq. III.5 where the parameters are extracted from a 2D Gaussian fitting of the corresponding data.

Outside this range of phases, readout with displaced two-mode squeezed vacuum has a lower SNR than with coherent light due to one or both of the two qubit states having

a substantially higher noise than CS+PP readout. We also note that the improvement in SNR does not increase monotonically with squeezing strength (r_E, see Sec. II.E); it reaches maximum for entangler gain between 1.5 dB and 2.5 dB, then decreases at higher entangler gain. There are two major reasons for this behavior of the SNR. First, photon loss inside the two-mode squeezed light interferometer limits the maximum amount of entanglement/noise reduction which can be achieved. Second, as we turn up the gain of the entangler JPC, it is more likely to saturate the analyzer JPC and cause its gain to drop and its amplification process to be less ideal, which reduces SNR. This effect is responsible for the drop of SNR for entangler gain of 4 dB shown in Fig. 23. [110, 111].

G. Backaction of two-mode squeezed light measurement

Another important figure-of-merit of a quantum measurement is its efficiency, which determines the fraction of information of the system being measured which is obtained by the observer, rather than lost to all other potential observers [54, 90, 112, 113]. Readout fidelity scales exponentially with measurement efficiency (See Eq. I.1), and thus it plays a vital role in experiments which requires fast and high fidelity measurements, such as feedback control in quantum error correction [114].

As we discussed in Chapter 2 (need an introduction about the science protocol...), in our experiment, the quantum efficiency η of our qubit measurement is determined by analyzing its back-action on the qubit with a weak measurement protocol Ref. [54]. This protocol provides a self-calibrated way of determining the overall efficiency of a measurement system. A typical result for the coherent state measurement and the corresponding tomography data is shown in Fig. 24(a). The conditional x and y components of the qubit state Bloch vector for measurement results that have zero in-phase component ($I = 0$) of coherent light readout is shown in Fig. 25(a). The theory for coherent weak measurement back-action suggests that the amplitude and frequency of the x and y-component oscillation, are determined by both the measurement strength and the efficiency of the measurement system. Therefore, by fitting this set of data to Eq.(science protocol equation), we can obtain the self-calibrated

measurement strength and the overall efficiency of the measurement setup. From the data of coherent light measurement, we obtain a overall efficiency of $\eta = 0.46$ which sets the base line of our system. By accounting for the known loss in coherence due to T_2 process, we can also calculate a corrected efficiency of $\eta_{cor} = 0.52$.

However, as there is no well established theory for weak measurement back-action with our TMS interferometer, we focus our study on two special cases where it most closely resembles the coherent light measurement; the 'TMS High' and 'TMS Low' cases shown in Fig. 21(a) where the output noise power is independent of the qubit state, and the interferometer's output resembles CS + PP readout with unusual noise values. Figure. 24(b) and (c) show the weak measurement result and corresponding tomography data and Fig. 25(b) and (c) show the results of the conditional x and y components of the qubit state Bloch vector at $(I = 0)$ for 'TMS High' and 'TMS Low' case, respectively. We have adjusted the drive amplitudes to match all three measurement types classical SNR (and correspondingly their z-component back-action, see Fig. 26). However, the data clearly show that both the oscillation frequency and amplitude of the x- and y- components are very different from the CS + PP case, which indicates that the back-action strength and measurement efficiency are very different. From the same fitting, we obtain an efficiency of 0.58 at the displaced two-mode squeezed vacuum readout at the 'TMS High' point, and 0.29 at the 'TMS Low' point.

One cause for this effect which we must rule out is that different TMS settings produce larger and smaller noise compared to the fixed contribution of the output chain following the analyzer JPC. That is we need to confirm that the observed large changes in quantum efficiency of the three readout methods *can not* be explained by changes in the ratio of output noise of the TMS interferometer and the classical noise from the output chain.

The overall measurement efficiency of the system extracted from the weak measurement protocol can be expressed as:

$$\eta = \eta_{\text{Amp}}\ \eta_{\text{out}}, \tag{III.6}$$

where η_{Amp} is the efficiency of the system before HEMT (qubit-cavity and JPC/TMS interferometer), η_{out} is the efficiency of the output chain after the analyzer JPC which is dominated by the efficiency of the HEMT amplifier. The efficiency of the output chain, η_{out},

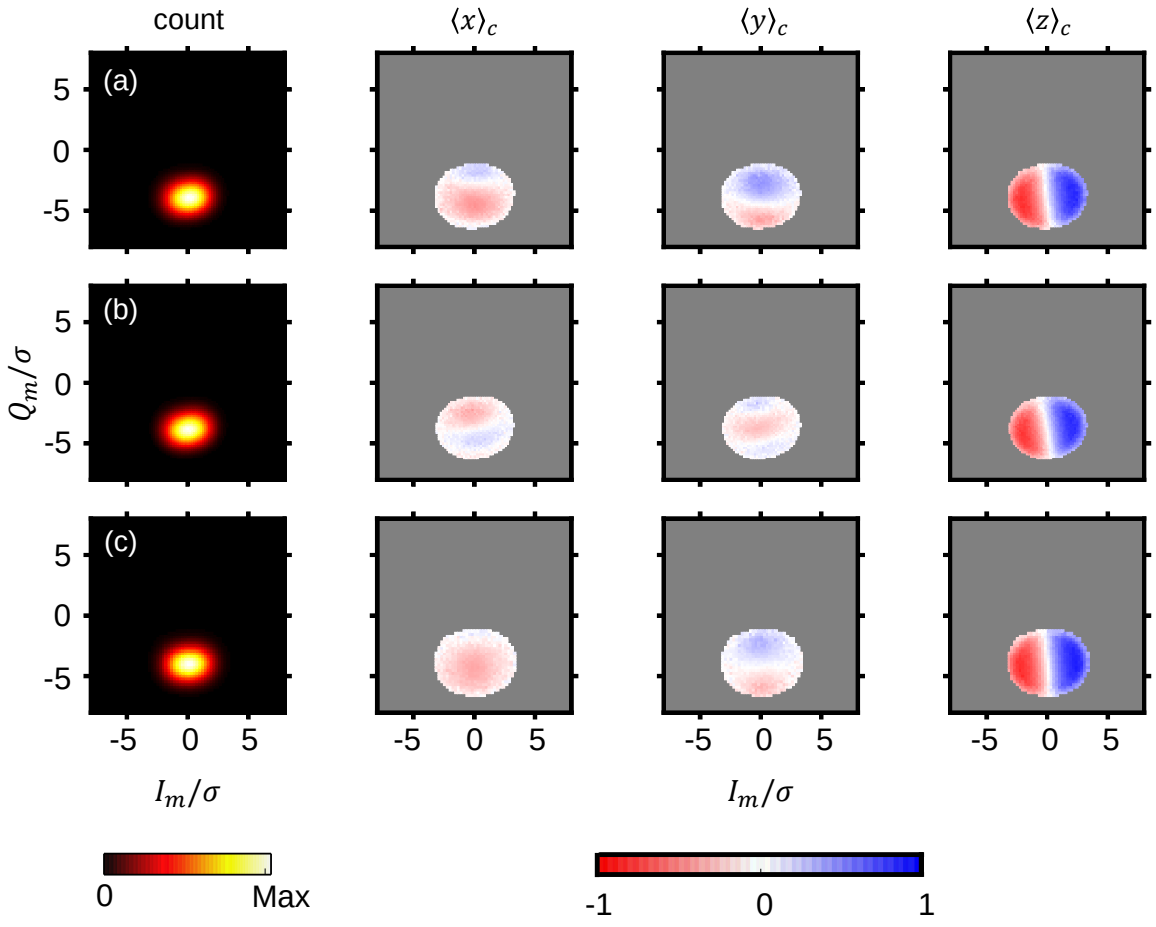

Figure 24: **Experiment data for back action of weak measurement.** Results are shown for the back action of the weak measurement for coherent light (a) and displaced two-mode squeezed vacuum at high(b) and low(c) noise level match point. In all three cases, the strength of the weak measurement is $\bar{I}_m/\sigma = 0.66$. The leftmost column shows the 2D histograms of scaled measurement outcomes recorded during the weak measurements. The right three columns are the conditional tomography data for $\langle x\rangle$, $\langle y\rangle$ and $\langle z\rangle$ component versus the associated $(I_m/\sigma, Q_m/\sigma)$ bin. The value in each bin is the average of all tomography data associated with that (I_m, Q_m) value.

can be expressed as:

$$\eta_{\text{out}} = \frac{N_{\text{Amp}}}{N_{\text{Amp}} + N_{\text{out}}}. \tag{III.7}$$

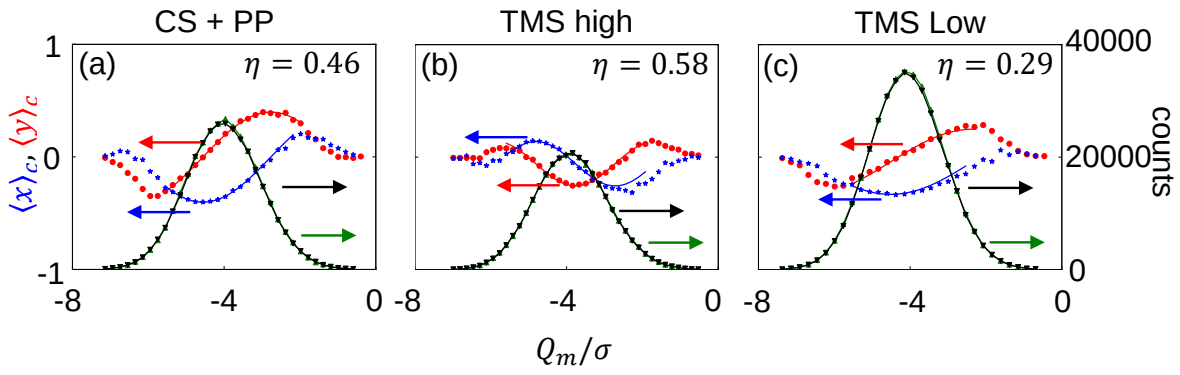

Figure 25: **Quantum efficiency obtained by analyzing the back-action of weak measurements.** Tomography data for x and y (blue stars and red dots) components of the qubit Bloch vector after we apply a weak measurement (see supplementary for details) are plotted against the left axis. The counts observed for each x and y tomography data points are shown with black down pointing triangle and green up pointing triangle, plotted against the right axis. The data is recorded for coherent light as well as displaced two-mode squeezed vacuum at relative pump phase point such that the ground and excited state qubit has the same noise level. Data is then fitted to the theory model for coherent light [54]. The measurement strength is adjusted such that all the measurements have the same SNR. The efficiency value obtained for each point is shown as well. The η is the quantum efficiency extracted from the fitting model . A surprisingly low quantum efficiency is observed when the system has less output noise level.

where N_{Amp} is the output noise power of the analyzer JPC, N_{out} is the added noise power of the output chain referred back to the input of the HEMT. An easily measurable quantity in the lab that is closely related to η_{out} is the noise-visibility-ratio (NVR),

$$NVR = \frac{N_{\text{Amp}} + N_{\text{out}}}{N_{\text{out}}}. \tag{III.8}$$

It is easy to see:

$$\eta_{\text{out}} = 1 - \frac{1}{NVR}. \tag{III.9}$$

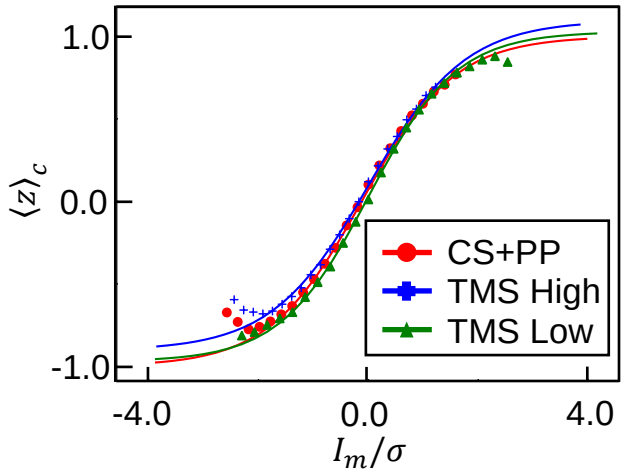

Figure 26: **Experiment data for z-axis back action of weak measurement.** Tomography data for z-component of the qubit Bloch vector along $Q_m = -4$ of the 2D histograms shown in Fig. 24. Different color indicates the case for CS + PP, TMS high match and TMS low match, respectively.

In our experiment, the NVR is typically 7 dB when the analyzer JPC is operated at 20 dB gain. Therefore, for coherent light readout, given $\eta = 0.46$ extracted from the weak measurement, we have $\eta_{Amp} = 0.58$ for our system.

Now consider the case of the displaced two-mode squeezed vacuum (TMS). Even though we did not measure the its NVR directly, we can calculate it based on the NVR of coherent light and the noise suppression/enhancement shown in Fig. 21. The NVR for TMS at the high (H) and low (L) match points can be expressed as

$$NVR_{TMS}^{H/L} = 1 + \frac{N_{TMS}^{H/L}}{N_{\text{out}}} = 1 + \frac{N_{CS}}{N_{\text{out}}}(\frac{\sigma_{TMS}^{H/L}}{\sigma_{CS}})^2, \tag{III.10}$$

which is larger (smaller) at the high (low) match point than that of coherent light. Consequently, the efficiency of the output chain (η_{out}) will also be larger (smaller) than that of the coherent light readout.

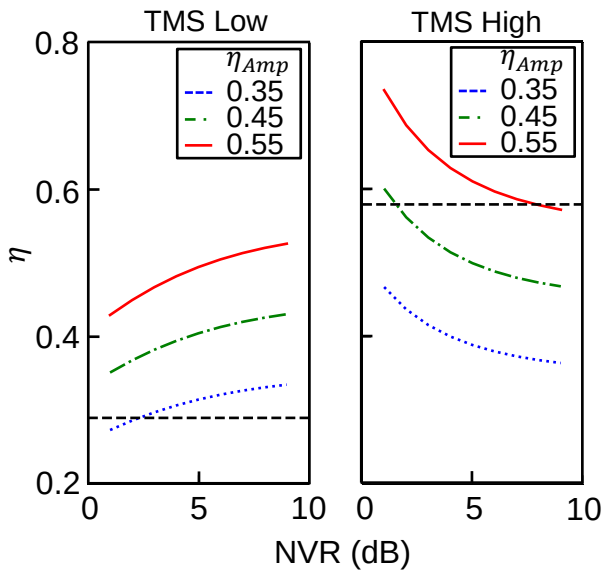

Figure 27: **Calculated overall efficiency of our measurement system for displaced two-mode squeezed vacuum as a function of NVR for different analyzer JPC/TMS interferometer efficiency.** Overall efficiency of the system vs NVR at the 'TMS Low' and 'TMS High' matched points for different amplifier efficiency $\eta_{\text{Amp}} = 0.35$ (blue dash line), 0.45 (green dotted line) and 0.55 (red line). The black dash lines show the value of efficiency obtained from the weak measurement protocol.

If we assume the quantum efficiency of TMS interferometer is the same as that in the coherent light case, namely, $\eta_{Amp} = 0.58$, and a typical coherent light NVR, 7 dB, then given the $\frac{\sigma^H_{TMSL}}{\sigma_{CS}} = 1.21$ and $\frac{\sigma^L_{TMSL}}{\sigma_{CS}} = 0.86$, we can calculate the overall quantum efficiency of the system at the high and low σ match point. We get $\eta^H = 0.48 < \eta^H_{exp} = 0.58$ and $\eta^L = 0.42 > \eta^L_{exp} = 0.29$.

More generally, in Fig. 27 we plot the overall efficiency as a function of NVR for different values of η_{Amp}. This shows that even if we vary the relative noise contributed by the analyzer and the output chain, the known changes in output noise cannot explain simultaneously explain both the TMS High and Low results. Instead, it appears that the TMS readout behaves somewhat analogously to readout with a phase-sensitive amplifier, enhancing measurement

SNR/z back-action at the TMS Low match point at the cost of rendering the x- and y-back action more sensitive to degradation by losses or added noise (and thus lowering the apparent efficiency in our imperfect apparatus). Interestingly, the TMS High match point, which represents a substantially *worse* SNR also allows the qubit's phase back-action to be more faithfully reported to an observer, even in the presence of loss and inefficiency.

H. Conclusion

In this chapter, we have demonstrated a new scheme for interferometric readout of a superconducting qubit with displaced two-mode squeezed vacuum and phase preservation amplification. In this readout scheme, we can increase the SNR of projective readout by suppressing the noise output of our amplifier below the usual Cave's limit for an amplifier fed with unsqueezed vacuum. In our experiment, we have achieved a 44% improvement in power SNR compared to conventional coherent light plus phase-preserving amplification readout. This improvement in SNR will result in a suppression of readout infidelity by a factor of 5, if one starts with a 1% error rate in coherent light readout, with even greater improvements at higher base fidelities.

A still more interesting result emerges as we investigate the quantum readout efficiency of our TMS interferometer using weak measurements at points where the noise output is the same for both qubit states. These data show that there are important effects on the ratio between z back-action and the concomitant qubit phase back-action of this measurement process relative to other known readout schemes. It appears that the increase in SNR at the 'TMS Low' match point comes at the cost of reducing the trackability of phase back-action. Conversely, at the 'TMS High' match point this phase trackability is enhanced. Although we rule out post-interferometer noise as the source of this effect, more theoretical work is needed to understand the role of inefficiencies inside the interferometer due to imperfect squeezing/amplification and losses in the interferometer arms. Finally, while tracking a single qubit's phase during measurement is not of direct value for single qubit measurements in quantum computing, measurement-based entanglement is a vital component of many

error-correction schemes in quantum information, and in these schemes [108,115,116], maintaining/tracking two qubit phase coherence during a high-fidelity measurement is vital. Our current experiment can be readily extended to two-qubit entanglement [115] by adding a second qubit on the lower arm, and we expect the ability to rebalance measurement strength and phase trackability *in-situ* to give crucial tolerance for losses and inefficiencies which currently limit these experiments.

Therefore, this limitation notwithstanding, the fact that the 'TMS High' match point gives this desirable quantum properties at a point which deliberately degrades SNR and fidelity of projective measurement should encourage exploration of measurement methods which are not just the quantum analogs of good classical measurement schemes.

IV. Qubit-bath engineering via parameteric drives: Theory

A. Overview

Loss is ubiquitous in open quantum systems. In general, such dissipation to the environment is undesired as it leads to decoherence of the quantum state of the system. However, by carefully engineering the coupling between the system and the dissipative bath (so called 'bath engineering'), we can also create forms of dissipation which perform a useful task. Examples in superconducting circuits include the use of bath engineering for qubit state preparation/reset [59–61] and generation of multi-qubit entangled states [62, 63]. Some of these protocols rely on the dispersive coupling between the qubit and cavity to create the necessary frequency shift of the qubit drive and use the frequency selectivity of the drives to select the desired processes. This method requires us to populate the cavity to generate the frequency shift, which can cause extra difficulties when reading out the qubit. Another method used in [61] is similar to what we are trying to do in this project, where they used a dc SQUID as a tunable coupler shared between a transmon qubit and a resonator. The coupling strength is controlled by the external flux threading the SQUID. The parametric control is realized by modulating this external flux. This method will require a fast dc control line, and the 'heating' and 'cooling' processes (the meaning of 'heating' and 'cooling' will be clear in the discussion of this chapter) cannot be addressed separately. The use of a dc SQUID will also introduce a large undesired fourth order terms to the system.

In our work, we realize bath engineer a transmon qubit through a 3-wave parametric coupling (similar to the example in Sec. II.C) in the system. We will focus on the theory of such a system in the Chapter and its experimental implementation in the Ch. VI.

We have realized three-wave bath-engineering circuits in two ways, first using the JRM and then, more recently, using SNAIL-based resonators. In both shunted JRM and SNAIL-based circuits at optimal bias points, they provide a large third order term while suppressing the fourth order terms, which will create a frequency shift similar to that in the dispersive measurement. This effect from the fourth order terms is undesirable as it will move the

mode frequencies around when we try to drive the system. However, as discussed in detail below, the three modes of the JRM and their spatial connections make JRM-based circuits less flexible, and this work has moved entirely to SNAIL-based resonators.

This chapter is organized as follows: We begin in Sec. IV.B by introducing the original theory proposal of the project from Hafezi *et al.* [70] in which the authors propose to create a photonic system with chemical potential created by parametrically driven, third-order processes. In Sec. IV.C, we discuss our first design, which is a direct implementation of Hafezi's proposal using a qubit and a JPC with one of its' modes having a very low frequency. We also discuss the practical limitations of this design. Next in Sec. IV.D, we talk about an alternative design we used in the experiment which consists of a qubit and lossy SNAIL resonator parametricaly coupled with each other. Finally, in Sec. IV.E we give a brief conclusion.

B. A parametrically generated chemical potential for light

In this original theory proposal [70], the authors design a parametric scheme to address the issue of chemical potential and thermalization in photonic systems. Unlike fermions (such as electrons), photons lack a natural chemical potential which preserves their number. This is a challenge for the use of photonic modes in quantum simulators and other potential applications [68, 117] , as these systems will tend to decay to the vacuum state. Thus, we seek to create an effective chemical potential by parametrically coupling a photonic system (a microwave mode in our case) to a thermal bath (a lossy microwave resonator mode) at finite temperature. More, chemical potential will be set by the frequency of the parametric drive, and thus is *in situ* tunable over a range of values.

To understand the picture of thermalization via parametric coupling, we consider a system with Hamiltonian H_S coupled to a thermal 'bath' H_B (consisting of a collection of spins or a low-Q mode) via a term λH_{SB}. The thermal bath will start in a initial state $\rho_B = e^{-\beta H_B}$, where β is the inverse temperature $\beta = 1/k_B T$ (k_B is the Boltzmann constant and T is the temperature). For a usual, non-parametric coupling, the coupling strength λ is a constant

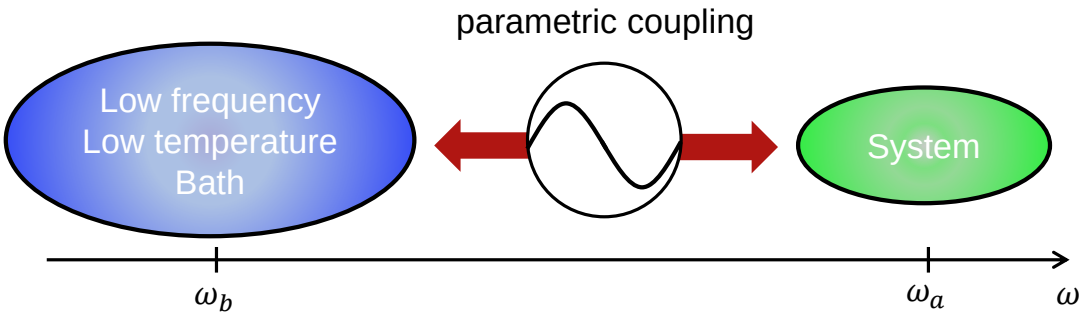

Figure 28: **Schematics of the system parametrically couple to a thermal bath.** Thermal bath with mode b can be parametrically coupled to a higher frequency system with mode a. Figure is adapted from Hafezi *et al.* [70].

which is determined by the distribution of the electromagnetic fields set by the physical geometry of the system and bath. One modification of this proposal is to replace this constant coupling strength with a parametric one as shown in Fig. 28, that is, $\lambda \to 2\lambda\cos(\omega_p t)$, where ω_p is the frequency of the parametric drive. Now the Hamiltonian of full system-bath is given by:

$$H = H_S + H_B + 2\lambda\cos(\omega_p t)H_{SB} \tag{IV.1}$$

Here we assume the system-bath coupling H_{SB} takes the bi-linear form, which is commonly available in superconducting circuits:

$$H_{SB} = \Sigma_j (a + a^\dagger) B_j \tag{IV.2}$$

where B_js are the bath operators, and $a^\dagger$ (a) is the creation (annihilation) operator for the primary system mode we wish to control. In general, H_s can be any system Hamiltonian, but here for our purpose, we will take H_s to be an anharmonic oscillator: $H_s = \omega_a a^\dagger a - \alpha a^\dagger a a^\dagger a$.

Then we move to a rotating frame with the rotating operator: $R = \exp(-i\omega_p t a^\dagger a)$. The Hamiltonian transformation is given by:

$$\begin{aligned} \tilde{H} &= R^\dagger H R - iR^\dagger \dot{R} \\ &= H_s - \omega_p a^\dagger a + H_B + 2\lambda \cos(\omega_p t) R^\dagger H_{SB} R \end{aligned} \tag{IV.3}$$

where H_s and H_B remains unchanged as $[H_s, R] = [H_B, R] = 0$ and $iR^\dagger \dot{R} = -\omega_p a^\dagger a$. The system-bath coupling term now becomes:

$$\begin{aligned} \tilde{H}_{SB} &= \lambda \Sigma_j R^\dagger [(e^{-i\omega_p t} + e^{i\omega_p t})(a + a^\dagger) B_j] R \\ &= \lambda \Sigma_j (a + a^\dagger + a e^{-2i\omega_p t} + a^\dagger e^{2i\omega_p t}) B_j \\ &\simeq \lambda \Sigma_j (a + a^\dagger) B_j \end{aligned} \tag{IV.4}$$

The key approximation we use from line 2 to line 3 in Eq. IV.4 is the rotating wave approximation. We neglect the fast oscillating terms like $ae^{-2i\omega_p t}$ to reach the simplified form of $\tilde{H}_{SB}$. Putting all the terms together, we get the new Hamiltonian in the rotating frame:

$$\tilde{H} = H_s - \mu N + \lambda \tilde{H}_{SB} + H_B \tag{IV.5}$$

where $\mu = \omega_p$ and $N = a^\dagger a$ is the number operator for the system. Then given a weak coupling λ and the bath state $H_B = \exp(-\beta H_B)$, we will get an equilibrium thermal state for system in the long time limit:

$$\rho \simeq \exp[-\beta(H_s - \mu N)] \tag{IV.6}$$

This is the distribution of the grand canonical ensemble and we can thus identify the chemical potential for the system to be $\mu = \omega_p$. As ω_p is the frequency of the parametric drive manually applied to the system, this result indicates we have created a photonic system with a tunable chemical potential.

The key point in this proposal is to have a low temperature, low frequency bath parametrically coupled to a high frequency mode. Because of the low frequency of the bath, the drive frequency $\omega_{p1} = \omega_a + \omega_b$ for 'up going' process that populates the qubit photon and the frequency $\omega_{p2} = \omega_b - \omega_b$ for 'down going' process that empties the qubit photon are close to each other. So, one parametric pump can drive both processes and by controlling

the drive detuning one can change the relative rate of two processes, thus creating a tunable chemical potential. However, as we will see in the later part of this chapter, we can also apply the drives separately by having a high Q qubit couple to a lossy SNAIL mode. This method turns out to be actually more flexible and give a variety of new controls compare to the original proposal.

C. Bath engineering via a JPC with one low-frequency mode

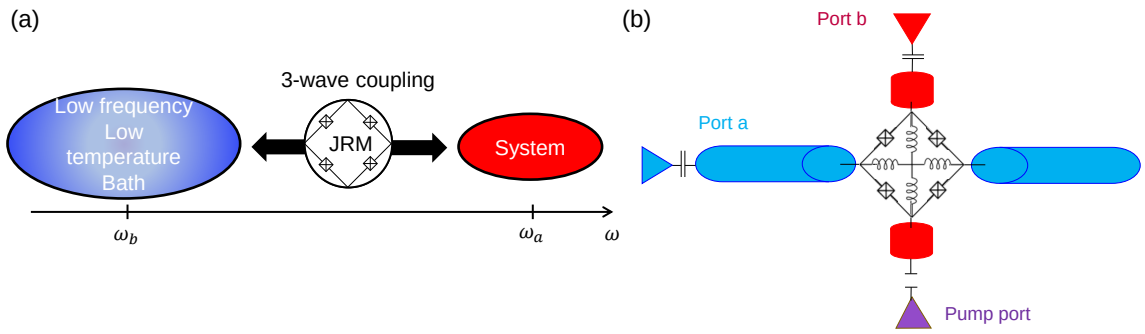

Figure 29: **Low frequency JPC implementation for bath engineering.** (a) The idler mode of the JPC is designed to have low frequency ($\sim$ 300 MHz) that serves as the low frequency, low temperature bath. The signal mode is a high frequency ($\sim$ 7.5 GHz) mode. It couples to a transmon qubit to create the necessary anharmonicity, then this new non-linear mode will be the system mode. There is a common mode that is not shown in the figure. The JRM provides the 3-wave mixing term which generates the parametric coupling between the system and bath. (b) Schematic of such implementation. The design is similar to a conventional JPC, only with one of the mode (mode a) being the low frequency one. The low frequency mode is realized by increasing the length of the transmission line (the length is not to scale in the schematic).

We first introduce a direct implementation for the original proposal. As shown in Fig. 29, we consider a JPC with a low frequency ($\sim$ 300 MHz) idler mode and a high frequency ($\sim$ 7.5 GHz) signal mode. The signal mode is used as the system mode and its frequency

is chosen as a convenient 'typical' frequency for qubits and cavities. The idler mode is used as the low temperature bath. Its low frequency mode sets the temperature of the 'bath'. Since $\hbar\omega_i \ll k_B T$, this resonator has non-zero photon occupancy and as chemical potential transfers photon number, not energy, so the lower frequency mode is higher effective occupancy and thus at a higher temperature. However, if we realize this mode using a transmission line resonator (see Fig. 29(b)), as in a conventional JPC (like in Sec. II.D) it will give rise to other practical issues that could limit the performance of the device. We will give more detailed discussion about this in the end of this section.

The signal mode then needs to couple to a transmon qubit to introduce anharmonicity to the mode, making it a weakly anharmonic qubit. This effective qubit mode is then used as the 'system'. The common mode is not shown in the figure (we will discuss its issues in this section and Sec. VI.B), but as we discuss in the JPC chapter, the JRM creates a 3-wave mixing term between these modes, leads to the interaction Hamiltonian:

$$H_{int} = g_3 \Phi_s \Phi_i \Phi_c \tag{IV.7}$$

where g_3 is the third order coupling strength and the Φ_is are the fluxes for each mode, where s, i and c represent signal, idler, and common mode respectively. If we re-write it in terms of the creation and annihilation operators, we will get:

$$H_{int} = g_3 (a + a^\dagger)(b + b^\dagger)(c + c^\dagger) \tag{IV.8}$$

To match the notation we used in the previous section, here we let a be the signal mode, b be the idler mode and c be the common mode. Now if we apply the parametric drive on the common mode at frequency ω_p and keep it far detuned from the its own eigen frequency, this drive can be considered as a 'stiff' pump, meaning we can replace the operator c by its classical average $\langle c \rangle e^{-i\omega_p t}$:

$$H_{int} = g_3 \langle c \rangle (e^{-i\omega_p t} + e^{i\omega_p t})(a + a^\dagger)(b + b^\dagger) \tag{IV.9}$$

and we find our reach the desired parametric coupling discussed in the previous section.

Now the next question is to introduce the anharmonicity to the signal mode. One relevant design is the 'Trimon' device from R. Vijay's group at TIFR [118, 119]. A 'Trimon'

device is a three-qubit system that is based on the JRM. The JRM is shunted by connecting superconducting pads to each node to create three coupled non-linear oscillator modes. Each mode behaves as a transmon qubit with resonant frequency and anharmonicity set by the shunted capacitance and junction parameters. This indeed produces our required non-linear signal mode, but there is also a non-trivial cross-Kerr type inter-mode couplings due to sharing of the for junctions amongst all three modes. The cross-Kerr couplings will shift the mode frequencies as the system is driven by parametric pumps, creating extra difficulties to implement the protocol. More, it is unclear whether we can create the required differences in frequency among the modes.

Instead of the Trimon idea, we plan to directly bring another transmon into close resonance with the signal mode to give it enough nonlinearity to behave like a qubit. In practice, this ancillary qubit needs to have a strong enough coupling with the signal mode to provide enough anharmonicity for the 'hybridized signal mode' used in the protocol. Also, in order to perform the measurement, we would need another ancillary readout mode to probe the state of this hybrid transmon-signal mode.

This low frequency JPC idea is not impossible to implement with superconducting circuits techniques, however there are some practical issues that need to be taken into account. The low frequency mode will give rise to two problems. Firstly, the participation ratio, defined as:

$$p = \frac{L_j}{L_j + L_{ext}} \tag{IV.10}$$

where L_j is the inductance from the junctions in each mode and L_{ext} is the external linear inductance in the corresponding mode. So we can see from this equation, the participation ratio will be low for this mode, as large linear inductance is used to bring down the mode frequency. This will lower the coupling strength between the modes and thus require a larger pumping strength which may triggering other higher order effects before we implement the desired process. For a detailed discussion about how the participation ratio is related with the coupling strength between modes in a JPC (or SNAIL other Josephson-junction containing mode), see Ref [120]. Secondly, a low frequency mode has many harmonics, some of which can be near the signal frequency, leads to a frequency crowding problem. As shown in the next chapter, we try to solve this problem by designing a bandgap filter to have a stop band

near the signal mode. In addition to these problems, another challenge is to to maintain a high Q for the hybrid transmon-signal mode so that photons can live long enough in this mode for the thermalization process to finish. This is achievable in principle. However, as we will talk about in the next chapter, it turns out to be one of the major challenges as we try to bring this idea to realization.

D. Bath engineering via lossy SNAIL

1. System Hamiltonian

In this section, we will introduce another proposal for this project: to implement a controllable bath for a transmon qubit by dispersively coupling it to a lossy SNAILmon as we discussed in Sec. II.F. A schematic is shown in Fig. 30. The system includes a transmon qubit and SNAIL with a dipole-dipole coupling between them. The Hamiltonian for such a system can be writen as:

$$H_{sys}/\hbar = \omega_a a^\dagger a - \alpha/2 a^\dagger a a^\dagger a + \omega_b b^\dagger b + g_{bbb}(b+b^\dagger)^3 + g_{ab}(a^\dagger b + a b^\dagger) \tag{IV.11}$$

where a ($a^\dagger$) and b ($b^\dagger$) are the annihilation (creation) operators for the qubit and SNAIL mode, respectively, ω_a and ω_b are the frequencies for qubit and SNAIL, α is the anharmonicity of the qubit, g_{bbb} is the third order coefficient of the SNAIL mode and g_{ab} is the coupling strength between the qubit and SNAIL. To simplify this Hamiltonian, we can diagonalize the linear part of the it and re-write the Hamiltonian in the new basis [121]:

$$\begin{aligned} \tilde{a} &= \cos(\frac{\theta}{2})a + \sin(\frac{\theta}{2})b \\ \tilde{b} &= -\sin(\frac{\theta}{2})a + \cos(\frac{\theta}{2})b \end{aligned} \tag{IV.12}$$

where $\theta = \arctan(\frac{2g_{ab}}{\Delta})$, and $\Delta = \omega_b - \omega_a$ is the frequency difference between the SNAIL and qubit. In this new basis, the new eigenfrequencies of each mode is given by:

$$\begin{aligned} \tilde{\omega}_a &= \frac{\omega_a + \omega_b - \sqrt{4g_{ab}^2 + \Delta^2}}{2} \\ \tilde{\omega}_b &= \frac{\omega_a + \omega_b + \sqrt{4g_{ab}^2 + \Delta^2}}{2} \end{aligned} \tag{IV.13}$$

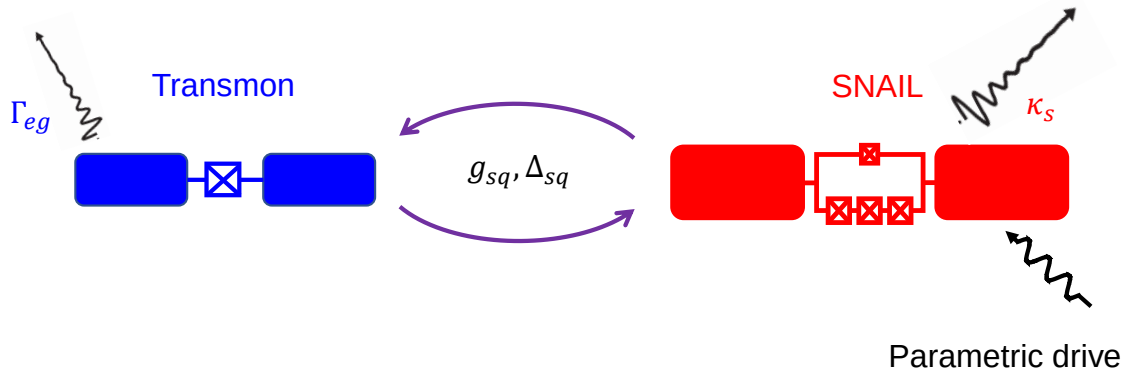

Figure 30: **Schematic of a transmon qubit dispersively coupled to a lossy SNAIL.** To implement a controllable bath for the transmon qubit, we have it coupled to a SNAIL. The SNAIL is to introduce a third order term in the system and is placed in the proximity of the qubit to produce a dipole-dipole coupling between them. The qubit is designed to have a high coherence while the SNAIL mode is made to strongly coupled to the environment. The bath engineering is realized by combining this dissipation and the parametric drives applied to the SNAIL mode.

with these results, we can now re-write the system Hamiltonian in the new basis as:

$$\begin{aligned}\tilde{H}_{sys}/\hbar = \tilde{\omega}_a \tilde{a}^\dagger \tilde{a} - \alpha[(\cos(\frac{\theta}{2})\tilde{a}^\dagger - \sin(\frac{\theta}{2})\tilde{b}^\dagger)\ (\cos(\frac{\theta}{2})\tilde{a} - \sin(\frac{\theta}{2})\tilde{b})]^2 \\ + \tilde{\omega}_b \tilde{b}^\dagger \tilde{b} + g_{bbb}(\sin(\frac{\theta}{2})\tilde{a} + \cos(\frac{\theta}{2})\tilde{b} + h.c)^3.\end{aligned} \tag{IV.14}$$

Due to hybridization, the third- and fourth-order nonlinearities which were previously exclusive to the SNAIL and qubit, respectively, are now distributed throughout the system, resulting in self- and cross-nonlinearities of each order for both modes. To see this more clearly, we can factor out the second term in the first line (originally the qubit Kerr term), to find:

$$\begin{aligned}\tilde{H}_{sys}/\hbar = \tilde{\omega}_a \tilde{a}^\dagger \tilde{a} + g_{aaaa} \tilde{a}^\dagger \tilde{a} \tilde{a}^\dagger \tilde{a} + \tilde{\omega}_b \tilde{b}^\dagger \tilde{b} + g_{bbbb} \tilde{b}^\dagger \tilde{b} \tilde{b}^\dagger \tilde{b} \\ + g_{aabb}(\tilde{a}^\dagger \tilde{a} \tilde{b}^\dagger \tilde{b}) + g_{bbb}(\sin(\frac{\theta}{2})\tilde{a} + \cos(\frac{\theta}{2})\tilde{b} + h.c)^3.\end{aligned} \tag{IV.15}$$

The last term is a three-wave mixing term comes from the third order term provided by the SNAIL. Then, similarly to what we have done with the JPC, we can apply various pumps at different properly chosen frequencies to drive the desired parametric processes. By combining these processes with the dissipation of the SNAIL mode, we can independently control the relaxation rates of the qubit and thus effectively create the 'heating' and 'cooling' process for the transmon.

For simplicity, here we only keep the fourth order terms that can survive the rotating wave approximation. The dipole-dipole coupling term is eliminated by the diagonalization, and the sine and cosine factors for the fourth order terms have been absorbed into the coupling strengths. Under the assumption that the modes are in the dispersive limit ($\Delta \gg g_{ab}$), we approximate $\cos(\frac{\theta}{2}) \simeq 1$ and $\sin(\frac{\theta}{2}) \simeq \theta/2 = \frac{g_{ab}}{\Delta}$, and so for each b index appearing in a fourth-order coupling, the strength will fall by $\frac{g_{ab}}{\Delta}$. Correspondingly, we will later make us of a similar notation for third order couplings in which every a index reduces the coupling strength by the same factor. Thus, the g_{aaaa} term, which represents the anharmonicity of the hybridized qubit modeis approximately unchanged, so that $g_{aaaa} \simeq -\alpha$. We also note that there is a new anharmonicity been introduced to the SNAIL-like mode. However as $g_{bbbb} = -\alpha(\frac{g_{ab}}{\Delta})^4$ is relatively both relative small and this mode will not be populated during the process due to the deliberately high loss rate of the SNAIL, so that we can safely neglect the effect of this term. Taken together, the first five terms describe a system of a qubit-like mode (an anharmonic oscillator) and a nearly-harmonic oscillator with a cross-Kerr $g_{aabb} = -\alpha(\frac{g_{ab}}{\Delta})^2$, which is a further undesired Kerr term that also comes from the anharmonicity of the qubit and the mode hybridization. It will have two effects that lead to unwanted frequency shifts when we apply parametric drives. One is the frequency shift due to 'real' photons in the system, but as our protocol only requires a few photons in both modes ($|g\rangle$ and $|e\rangle$ for qubit, and $0 \sim 2$ photons for SNAIL), this effect won't create a larger enough shift to change the behavior of the system. However, the off-resonance pump on SNAIL mode will also interact with this cross-Kerr term to generate AC Stark shifts that we will discuss below.

In addition to these unwanted Kerr terms, however, we have also created a series of cross-third order terms, of amplitude $g_{abb} = g_{bbb}(\frac{g_{ab}}{\Delta})$ which will power the bath engineering

processes we discuss below. A final note, for simplicity will omit the tilde symbol in our further calculations, so all the operators in the following of this section are in the hybrid basis unless otherwise stated.

2. Bath engineering with drive and dissipation of the system

As shown in Fig. 30, in order to implement a controllable bath, we need to combine the effects of parametric drives and SNAIL dissipation. The drive is applied to the SNAIL mode, and to model such a drive, we consider another term H_d for the system in addition to the H_{sys} in Eq. IV.15:

$$H_d = \epsilon_d(e^{i(\omega_d t+\phi_d)}b^\dagger + e^{-i(\omega_d t+\phi_d)}b) \tag{IV.16}$$

where ϵ_d is the magnitude of the drive, ω_d is the frequency of the drive and ϕ_d is the phase of the drive. Now the Hamiltonian that describes this driving system is given by $H = H_{sys}+H_d$. To eliminate this extra drive term, we move to a new displacement frame with operator $D(\beta) = e^{\beta b^\dagger - \beta^* b}$, where we carefully choose $\beta = \frac{\epsilon_d e^{-i\phi_d}}{\omega_d-\omega_b}$. Then by taking the displacement transformation of the Hamiltonian, $H' = D^\dagger H D - iD^\dagger\partial_t D$, we get the Hamiltonian in this frame:

$$\begin{aligned} H/\hbar = &\omega_a a^\dagger a - \alpha a^\dagger a a^\dagger a + \omega_b b^\dagger b \\ &+ g_{bbb}(\sin(\frac{\theta}{2})a + \cos(\frac{\theta}{2})(b+\beta e^{-i\omega_d t}) + h.c)^3 \\ &+ g_{aabb}a^\dagger a(b+\beta e^{-i\omega_d t})(b^\dagger + \beta e^{i\omega_d t}). \end{aligned} \tag{IV.17}$$

To further eliminate the time dependence in this Hamiltonian, we then transform again with $R = e^{i\omega_a t a^\dagger a + i\omega_b t b^\dagger b}$ and $H' = R^\dagger H R - iR^\dagger\partial_t R$, giving:

$$\begin{aligned} H/\hbar = &-\alpha a^\dagger a a^\dagger a + g_{bbb}(\sin(\frac{\theta}{2})ae^{-i\omega_a t} + \cos(\frac{\theta}{2})(be^{-i\omega_b t} + \beta e^{-i\omega_d t}) + h.c)^3 \\ &+ g_{aabb}a^\dagger e^{i\omega_a t}ae^{-i\omega_a t}(be^{-i\omega_b t} + \beta e^{-i\omega_d t})(b^\dagger e^{i\omega_b t} + \beta e^{i\omega_d t}). \end{aligned} \tag{IV.18}$$

With this Hamiltonian, we can see the effect of the parametric drive more clearly.

For example, if we pump the system at a frequency of $\omega_d = \omega_a + \omega_b$ (we will refer as a **'Σ drive'** in the future), then under the rotating wave approximation which eliminate all remaining fast rotating terms, we get this Hamiltonian:

$$H_\Sigma/\hbar = -\alpha a^\dagger a a^\dagger a + g_{abb}(\beta_\Sigma a^\dagger b^\dagger + \beta_\Sigma^* ab) + g_{aabb}a^\dagger a b^\dagger b + g_{aabb}a^\dagger a\beta_\Sigma^*\beta_\Sigma. \tag{IV.19}$$

The second term corresponds to a photon pair generation/annihilation process, where $g_{abb} = 6\ g_{bbb}\sin(\frac{\theta}{2})\cos^2(\frac{\theta}{2})$ is the effective three-body term (the factor of 6 comes from the exapnsion of the cube term) and β_Σ is the parametric driving strength. Effectively, we are creating a two-body coupling strength $g_\Sigma = g_{abb}\beta_\Sigma$ for the Σ drive generated from the combination of Σ drive and three-wave mixing coupling. The final two terms are the undesired AC Stark shifts, whose effects we will discuss further in the next section.

Similarly, if we pump the system at a frequency of $\omega_d = \omega_b - \omega_a$ (we will refer as 'δ **drive**' in the future), we will create another interaction Hamiltonian, this time with a photon swapping term resulting from the parametric drive:

$$H_\delta/\hbar = -\alpha a^\dagger a a^\dagger a + g_{abb}(\beta_\delta a^\dagger b + \beta_\delta^* a b^\dagger) + g_{aabb} a^\dagger a b^\dagger b + g_{aabb} a^\dagger a \beta_\delta^* \beta_\delta. \tag{IV.20}$$

where β_δ is the average driving voltage for the δ drive. Like before, the effective two-body coupling strength for the δ process is $g_\delta = g_{abb}\beta_\delta$.

In addition to these drives, there will also be dissipation which needs to be taken into account. We consider two important sources of dissipation in our model, the energy relaxation of the qubit with a rate of $\Gamma_{eg} = 1/T_1$ (assume the qubit temperature is zero) and SNAIL with a rate of $\kappa_s = 1/T_s$. We design the system in such a way that the qubit is weakly coupled to the environment while SNAIL has a strong external coupling so that $\kappa_s \gg \kappa_q$.

Bath engineering is realized by combining the dissipation and drives. We start with the 'Σ drive' case as an example. If we first neglect the higher order effects from the Kerr terms, this Hamiltonian from Eq. IV.19 will be very similar to that of a JPC which operates in the gain mode as in Sec. II.D with the only difference that one of the mode is strongly anharmonic. We show the energy level diagram for the system in Fig. 31 where the red numbers represent the state of the SNAIL and the blue letters represent the state of the qubit. Similar to JPC in gain mode, if we start in the ground state of the system $|0, g\rangle$, this pump will start to populate the qubit and SNAIL (signal and idler) mode, creates a coherent oscillation between the state $|0, g\rangle$ and the state $|1, e\rangle$. Next, as we have made the SNAIL mode to be very lossy compared to the qubit and drive rate ($\kappa_s \gg \kappa_q$), once the system reaches the state $|1, e\rangle$, the photon in the SNAIL will quickly decay into the external transmission line, leave the system in the state $|0, e\rangle$, as shown in Fig. 31(a). Effectively,

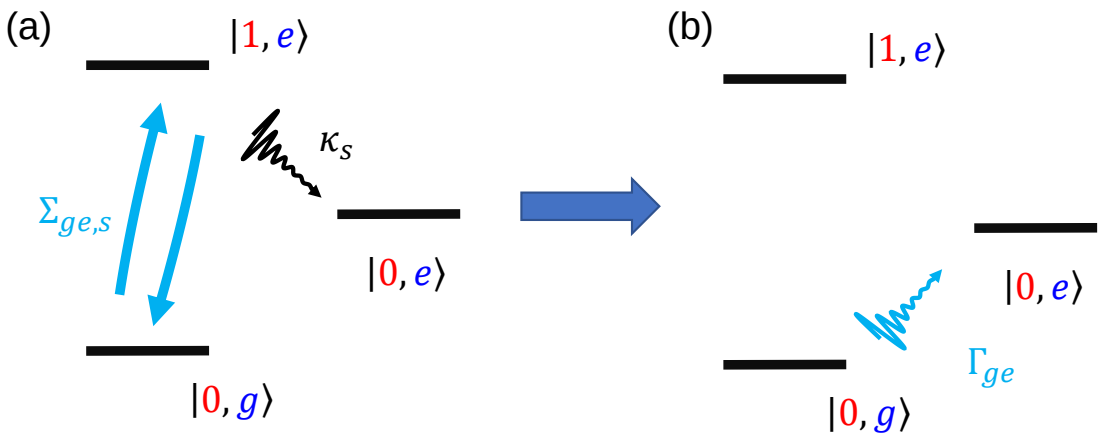

Figure 31: **'Heating process': effect of the 'Σ drive' and dissipation.** Red numbers represent the state of the SNAIL and the blue letters represent the state of the qubit. (a) The system starts in the state $|0,g\rangle$, then by turning on 'Σ drive', we create a coherent oscillation between $|0,g\rangle$ and $|1,e\rangle$. Because of the high loss rate of the SNAIL mode, κ_s, it will quickly lose its photon when system reaches $|1,e\rangle$, leave the system be in the state $|0,e\rangle$. (b) The whole process is effectively a 'heating process' for the qubit, since the qubit is incoherently brought from ground state to excited state.

the whole process behaves as if one has incoherently brought the qubit from ground state to excited state, thus a 'heating process', as shown in Fig. 31(b).

One important difference between this system and a JPC is that the qubit is a anharmonic and so the system is blocked from continually creating photon pairs. As we apply the 'Σ drive', the frequency will already be α detuned when going from $|1,e\rangle$ to $|2,f\rangle$ due to the anharmonicity of the qubit, as shown in Fig. 32. This stops the system from climbing the Fock ladder of each mode. There are two important notes here. The SNAIL itself has a very small Kerr term, and so the bath engineering is not strongly impacted by the state of the SNAIL, so that the SNAIL starting in state $|1\rangle$ does not prevent the bath engineering from functioning. More, the qubit spectrum gives us a series of heating and cooling processes we can control with a set of sum and difference frequency pumps for the different transmon

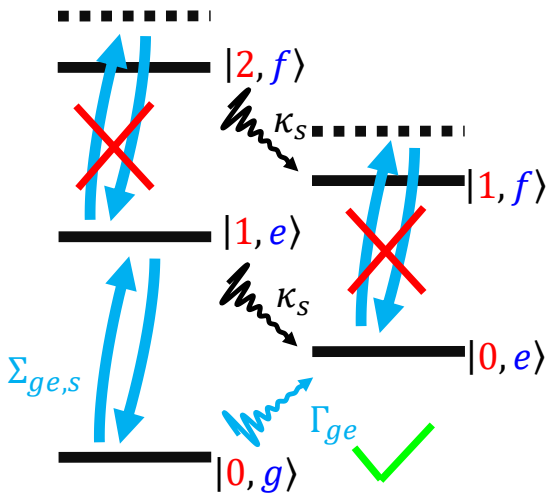

Figure 32: **Drive selectivity due to the qubit anharmonicity.** Red numbers represent the state of the SNAIL and the blue letters represent the state of the qubit. The pump frequency for $|0, g\rangle$ and $|1, e\rangle$ transition ($\Sigma_{ge,s}$) is one α detuned from the pump that drives $|1, e\rangle \leftrightarrow |2, f\rangle$ due the anharmonicty of the qubit. This non-linearity limits the process to happen within the $|g\rangle \sim |e\rangle$ manifold for the qubit.

transitions.

The 'δ drive' functions similarly, as shown in Fig. 33. The 'δ drive' is similar to JPC in conversion mode, if we start in the excited state of the transmon $|0, e\rangle$, this pump will start to create a coherent swapping between the state $|0, e\rangle$ and the state $|1, g\rangle$. Then, since the SNAIL mode is very lossy, once the system reaches the state $|1, g\rangle$, the photon in the SNAIL will quickly decay into the external transmission line, leave the system in the state $|0, g\rangle$, as shown in Fig. 33(a). Effectively, the whole process behaves as if one has incoherently brought the qubit from excited state to ground state, but at a rate much faster than the qubit's natural decay rate, thus a 'cooling process', as shown in Fig. 33(b).

In addition to the control between $|g\rangle$ and $|e\rangle$ state, the protocol can be easily extended to the $|f\rangle$ by varying the parametric pump frequencies, as shown in Fig. 34. With the same argument, by applying the parametric drive at frequency of $\omega_{\Sigma_{ef,s}} = \omega_{ef} + \omega_b$ and

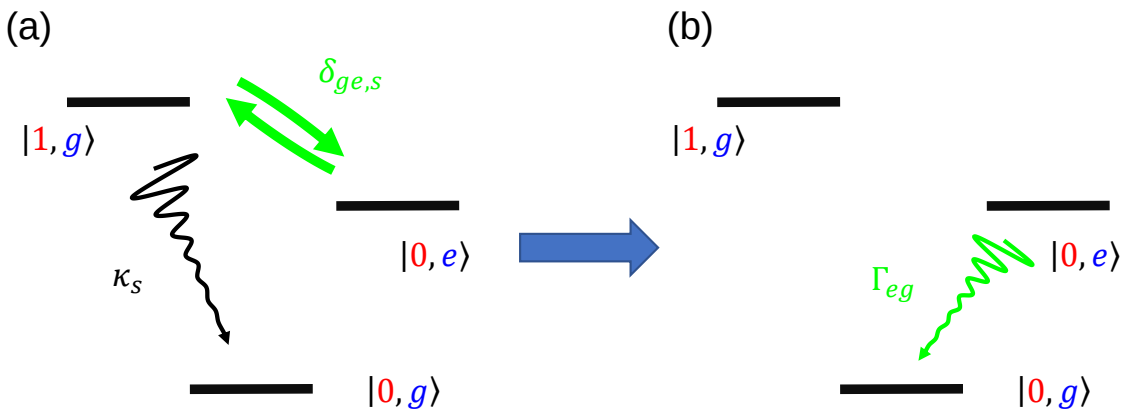

Figure 33: **'Cooling process': effect of the 'δ drive' and dissipation.** Red numbers represent the state of the SNAIL and the blue letters represent the state of the qubit. (a) System starts in the state $|0,e\rangle$, then by turning on 'δ drive', we create a coherent oscillation between $|0,e\rangle$ and $|1,g\rangle$. Because of the high loss rate of the SNAIL mode, κ_s, it will quickly lose its photon when system reaches $|1,g\rangle$, leave the system be in the state $|0,g\rangle$. (b) The whole process is effectively a 'cooling process' for the qubit, since the qubit is incoherently brought from excited state to ground state.

$\omega_{\delta_{ef,s}} = \omega_b - \omega_{ef}$ (where $\omega_{ef} = \omega_a - \alpha$ is the qubit ef transition frequency), we can create the 'heating' and 'cooling' processes respectively between the $|e\rangle$ and $|f\rangle$ states.

As we see in Eq. IV.6, for a system thermalizing to a bath (the lossy SNAIL in our case) at a fixed temperature given by β, a controllable chemical potential indicates that the final equilibrium can still be tuned by the value of the chemical potential μ. In the original proposal, this effect is enabled by changing the frequency of the parametric drives. Here in our case, as we have all the control knobs of the 'heating' and 'cooling' processes between the $|g\rangle$, $|e\rangle$ and $|f\rangle$ states, we can control these up-going and down-going rates by tuning the strength of the corresponding drives. Both the final (incoherent) steady state and the rate at which system reaches such state can be set by carefully choosing the magnitudes of these drives. Therefore implement the system with a controllable chemical potential.

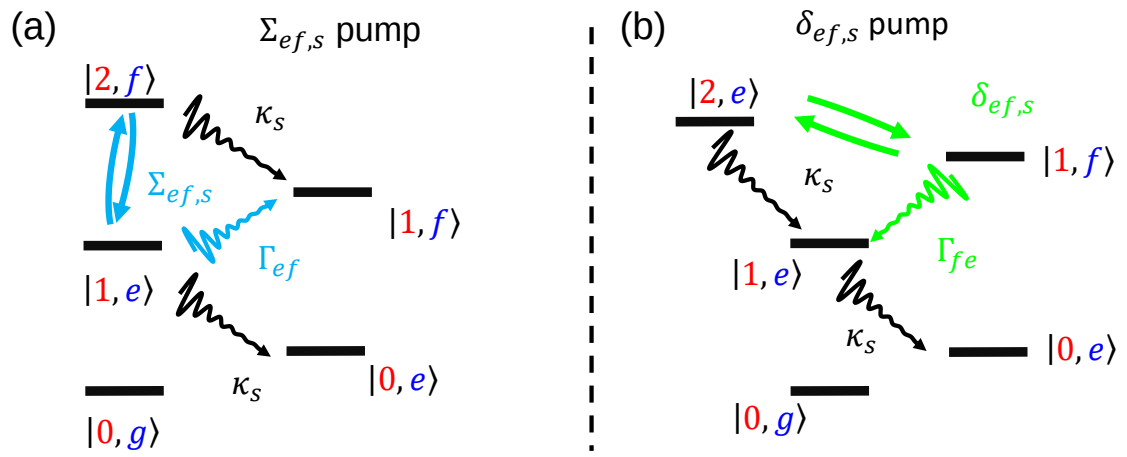

Figure 34: **Schematics of ef control.** Red numbers represent the state of the SNAIL and the blue letters represent the state of the qubit. (a) System starts in the state $|1,e\rangle$, then by turning on '$\Sigma_{ef,s}$ drive' with $\omega_{\Sigma_{ef,s}} = \omega_a - \alpha + \omega_b$, we create a coherent oscillation between $|1,e\rangle$ and $|2,f\rangle$. Because of the high loss rate of the SNAIL mode, κ_s, it will quickly lose its photon when system reaches $|2,f\rangle$, leave the system be in the state $|1,f\rangle$ the whole process is effectively a 'heating process' for the qubit between the e and f state. (b) System starts in the state $|1,f\rangle$, then by turning on '$\delta_{ef,s}$ drive' with $\omega_{\delta_{ef,s}} = \omega_b - (\omega_a - \alpha)$, we create a coherent oscillation between $|1,f\rangle$ and $|2,e\rangle$. Because of the high loss rate of the SNAIL mode, κ_s, it will quickly lose its photon when system reaches $|2,e\rangle$, leave the system be in the state $|1,e\rangle$ the whole process is effectively a 'cooling process' for the qubit between the e and f state. Note that this process can also be used for focing f state back to e when we are only interested in the processes in the two-level system.

3. Master equation and numerical results

To solve the full, lossy dynamics of the engineered system, one needs to consider the quantum master equation of the system. A detailed derivation of master equation for an open quantum system can be found in reference [86]. Specifically for our setup, we consider a transmon qubit coupled to a lossy SNAIL which in turn has a single parametric drive applied to it. The system Hamiltonian is given in Eq. IV.18. For the dissipator terms, we

consider the damping rates κ_q for the qubit, κ_s for the SNAIL and also a thermal excitation rate κ_{q-up} for qubit due to the finite temperature of the sample. With the Hamiltonian and the dissipator terms, we can write the master equation as:

$$\frac{d\rho}{dt} = \frac{1}{i\hbar}[H, \rho] + \mathcal{D}(\sqrt{\kappa_q}a)\rho + \mathcal{D}(\sqrt{\kappa_s}b)\rho + \mathcal{D}(\sqrt{\kappa_{q-up}}a^\dagger)\rho \tag{IV.21}$$

where ρ is the density matrix of the system, while $\mathcal{D}(O)\rho = O\rho O^\dagger - \frac{1}{2}\{O^\dagger O, \rho\}$ describes the effect of the dissipators. This equation can be solved numerically. Here we are going to discuss several important cases with different pump conditions.

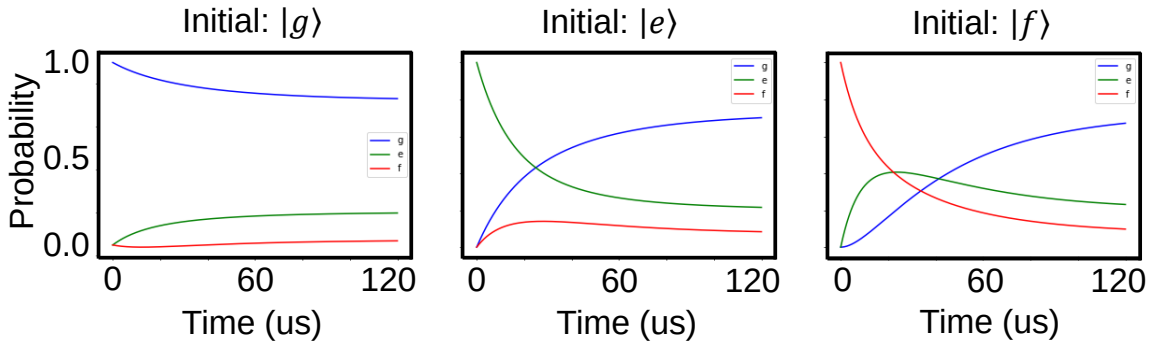

Figure 35: **Simulation result for natural decay.** All plots are qubit state probability for different energy levels as a function of time for different initial states. No drive is applied to the system. In each case, the qubit thermalizes to a state whose population distribution is set by the bath temperature regardless of the initial state of the qubit.

Let us first start with the simplest case, when there is no parametric drive applied to the system. Then under the rotating wave approximation, the Hamiltonian is simplified to an uncoupled qubit mode and SNAIL mode, as none of the third order terms can survive the approximation. In Fig. 35, we start with different qubit initial states: $|g\rangle$, $|e\rangle$ and $|f\rangle$ and plot the population number of each qubit level as a function of time. The parameters are $\omega_a/2\pi = 4.0$ GHz, $\alpha/2\pi = -200$ MHz, $\omega_b/2\pi = 8.5$ GHz, $\kappa_s/2\pi = 16$ MHz, $\kappa_q/2\pi = 0.052$ MHz and $\kappa_{q-up}/2\pi = 0.013$ MHz (the decay rates match a particular instance of our experiment which expired duing the COVID 2019 shutdown). Despite the different initial

states, due to the effect from both photon decay and thermal excitation, the qubit will finally reach a steady mix state, where the ratio between the population of each energy level is controlled by the rates of the 'up going' and 'down going' processes.

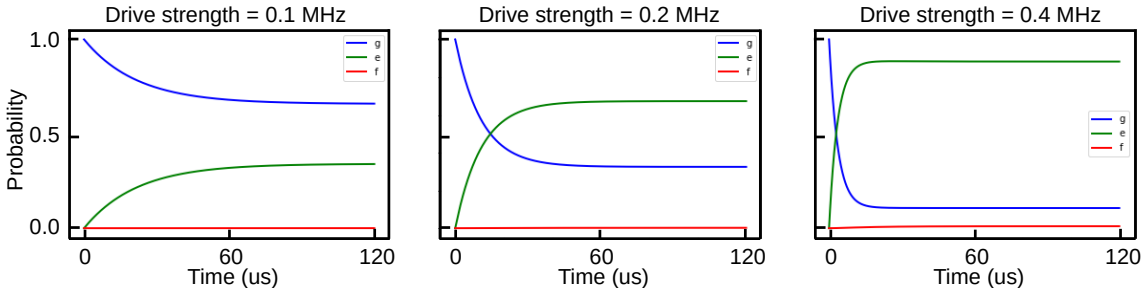

Figure 36: **Simulation result for $\Sigma_{ge,s}$ drive at different driving strengths.** All plots are qubit state probability versus time. The qubit is prepared in ground state. When the $\Sigma_{ge,s}$ drive is on, the $|e\rangle$ state population starts to increase, as expected. As the driving strength becomes stronger, the qubit both thermalizes to its equilibrium faster and also the excited state population is larger, indicating a 'hotter' qubit. As we keep increasing the drive strength, we reach a population inversion state for the qubit (with a negative effective temperature), which is not realizable by thermalizing the qubit to a natural heat bath.

Next we move to a slightly more complicated case: single '$\Sigma_{ge,s}$ drive'. As we discussed previously, now the Hamiltonian under the rotating wave approximation for this case is $H/\hbar = -\alpha a^\dagger a a^\dagger a + g_\Sigma(\beta_\Sigma a^\dagger b^\dagger + \beta_\Sigma^* ab)$, where we neglect the cross-Kerr terms whose effect will be discussed later. The decay parameters we are using are the same as in the undriven case, while the parametric driving strength is varied from 0.1 MHz to 0.4 MHz. In Fig. 36, we show the results of how the population changes vs. time under these different $\Sigma_{ge,s}$ driving strengths when qubit starts in ground state. As we expected from the argument in the previous section, with the $\Sigma_{ge,s}$ pump on, the system begins to heat up: the ground state population decreases while the excited state population increases. We also note that as this pumping strength gets stronger, there is some non-zero population of the $|f\rangle$ state. The rate at which system thermalizes to its equilibrium ($1/T_1 = \Gamma_{eg} + \Gamma_{ge}$) increases as we turn on the pumping strength. The population distribution in equilibrium is determined by both the qubit decay rate Γ_{eg}, which is unchanged, and the heating rate which is now dominated

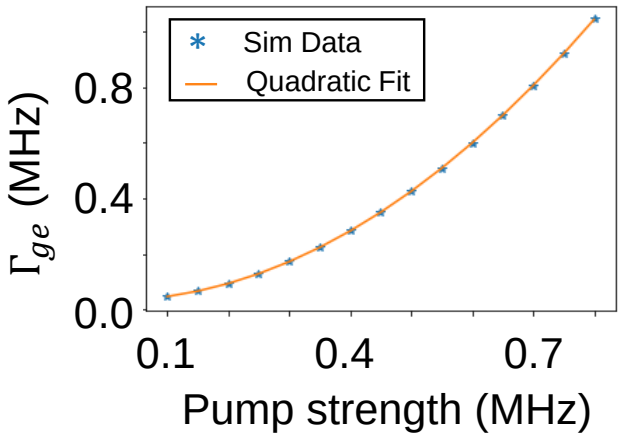

Figure 37: **'$\Sigma_{ge,s}$ drive' Γ_{ge} and Γ_{eg} vs pump strength**. The 'heating' rate Γ_{eg} as a function of driving strength. The rate for each data point is extracted from an exponential fitting from the result similar to Fig. 36. The observed heating rate scales quadratically with ump power.

by the parametrically generated heating process. The relation between this thermalizing rate and the corresponding pumping strength is shown in Fig. 37. As the overall process is a competition between 'measurement' by SNAIL photon decay and coherent Rabi driving, we expect to see a quadratic (rather than linear) relation between pump drive voltage and qubit relation rate. Therefore we fit the result to a quadratic model and the fitting curve demonstrates a good agreement to the simulated result, showing our understanding is correct.

Another similar example is the single $\Delta_{ge,s}$ drive, the Hamiltonian for this case is $H/\hbar = -\alpha a^\dagger a a^\dagger a + g_\delta(\beta_\delta a^\dagger b + \beta_\delta^* a b^\dagger)$. We use the same parameters for the simulation with a driving strength changing from 0.1 MHz to 0.4 MHz. In Fig. 38, we show the result of how the population changes as time under different $\delta_{ge,s}$ driving strengths when qubit starts in excited state. With the $\delta_{ge,s}$ pump on, the excited state population starts to decrease but at a rate faster than its natural decay and as we increase the driving strength, not only qubit decays faster but also it reaches a equilibrium with more ground state population. By comparing

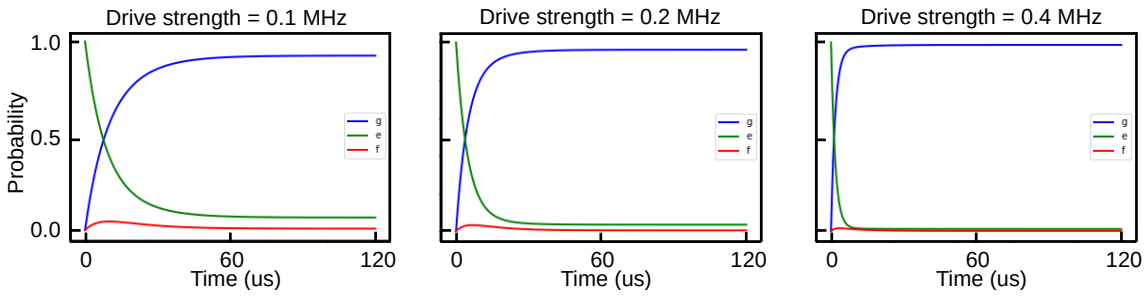

Figure 38: **Simulation result for $\delta_{ge,s}$ drive at different driving strengths.** All plots are qubit state probability versus time. The qubit is prepared in excited state. When $\Sigma_{ge,s}$ drive is on, the $|e\rangle$ state population starts to decrease more quickly, as expected. As the driving strength becomes stronger, the qubit thermalizes to its equilibrium faster and also the ground state population is larger, indicating a 'cooler' qubit.

the final population distribution with the natural decay case in Fig. 35, we note that with the 'cooling' process on, the qubit indeed thermalizes to a new state that has a lower temperature.

Next, as we want to control both the final population distribution and the rate that system reaches to that state, we need to apply the 'Σ' and 'δ' drives at the same time with carefully chosen strengths. In this case, the Hamiltonian for the system is: $H/\hbar = -\alpha a^\dagger a a^\dagger a + g_\Sigma(\beta_\Sigma a^\dagger b^\dagger + \beta_\Sigma^* a b) + g_\delta(\beta_\delta a^\dagger b + \beta_\delta^* a b^\dagger)$. Its effect is shown in Fig. 39, where we plot the population number as a function of time for the single and multi-pump cases. In the single pump case, we apply a '$\Sigma_{ge,s}$' pump with a strength of 0.1 MHz and for the multi-pump case, we use a 0.48 MHz '$\Sigma_{ge,s}$' pump and a 0.3 MHz '$\delta_{ge,s}$' pump. In both pumping schemes, the qubit thermalizes to a steady state with the same population distribution, corresponding to the same chemical potential. It is also clear to see that with both pumps on, the system reaches the equilibrium faster than the single pump case showing that by carefully choosing the strengths of the 'heating' and 'cooling' processes we can control both the final state of the system and the rate it goes to that state, thus creating a controllable bath for the qubit.

This can be explained by the Kerr effect which we neglect when considering the single pump process, and this can be a limitation to the performance of some single pump process

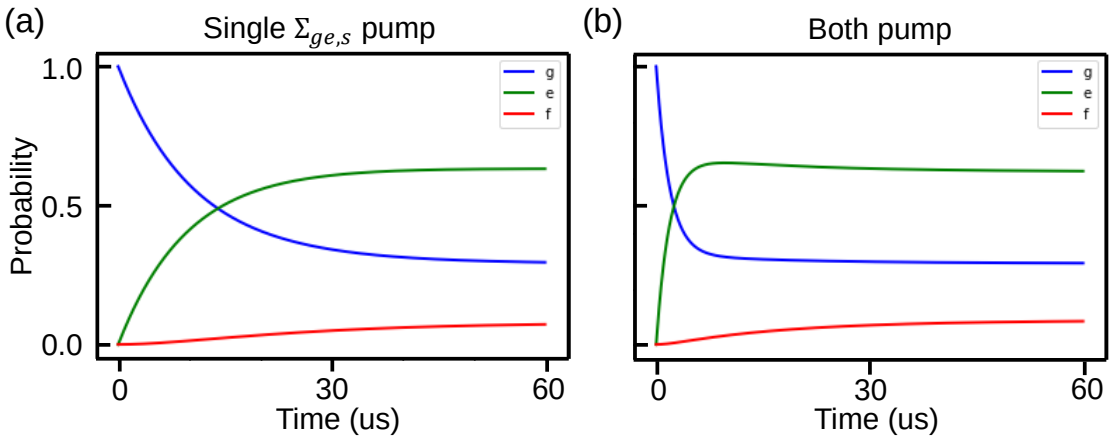

Figure 39: **Simulation result for single and multiple parametric drives.** All plots are qubit state probability versus time. The qubit is prepared in ground state. (a) We apply a single $\Sigma_{ge,s}$ drive to the system with a strength of 0.1 MHz. The qubit starts heating as we turn on the drive and it thermalizes to a distribution with $P_g = 0.29$, $P_e = 0.63$ and $P_f = 0.08$. (b) We apply a a 0.48 MHz '$\Sigma_{ge,s}$' pump and a 0.3 MHz '$\delta_{ge,s}$' pump. Now the system still thermalizes to the same population distribution, but at a much faster rate(τ_{ge} of $\sim$ 10 μs vs $\sim$ 1 μs). This shows that by applying multiple parametric drives we can independently control both the relaxation rate and the final thermal state populations.

as we have seen in our JPC research [81, 82, 89]. It is alos very important when we try to implement a multi-parametric pumping process like we are trying to do here, as each pump will change the behavior of the other pumps by a fair bit, like we see in [120].

To see this effect clearly, we consider the Hamiltonian with fourth order terms:

$$H/\hbar = -\alpha a^\dagger a a^\dagger a + g_\Sigma(\beta_\Sigma a^\dagger b^\dagger + \beta_\Sigma^* ab) + g_\delta(\beta_\delta a^\dagger b + \beta_\delta^* ab^\dagger) + g_{ssqq} a^\dagger a(\beta_\Sigma^* \beta_\Sigma + \beta_\delta^* \beta_\delta) \quad \text{(IV.22)}$$

The Kerr effect comes from the last term in the Hamiltonian which will shift the mode frequency with pump photons. This extra detune in frequency will result in a decrease of the pump rate as the drive is no longer on resonance and thus require a frequency correction to achieve the optimal pumping conditions. To understand this effect we drive the system

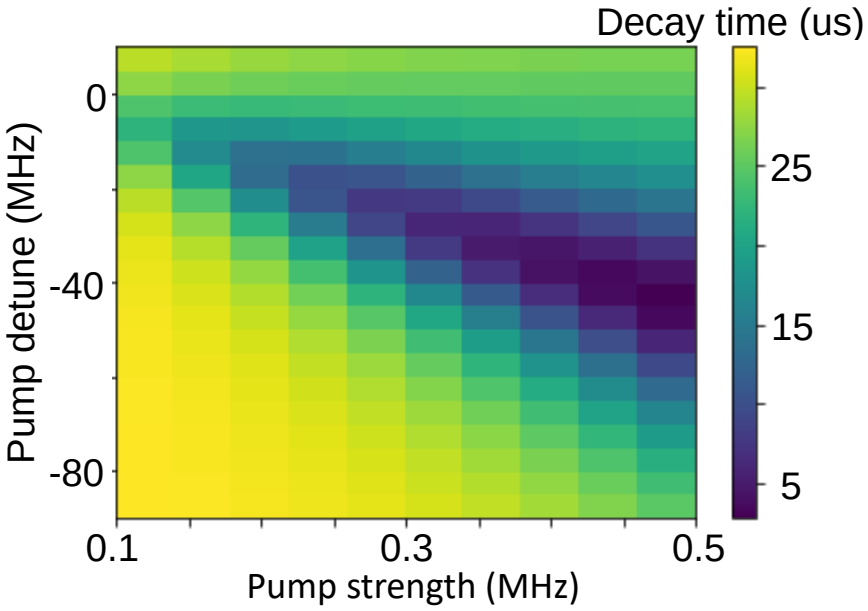

Figure 40: **Kerr effect on $\delta_{ge,s}$ drive.** The excited state decay time as a function of different pump conditions. The qubit is prepared in excited state and we apply a $\delta_{ge,s}$ pump to the system. We sweep the frequency and strength of the pump and record the e state population as a function of time. Then the decay of this population is fit to an exponential model to extract the decay time.

with a single '$\delta_{ge,s}$' drive and sweep the drive strength and frequency. The qubit starts in the excited state, and we fit the decay of the e state population with an exponential model.

In Fig. 40, we plot this decay time as a function of the pump conditions. The optimal pump frequencies (the points with fast decay rate), are moving negatively as we increasing the pumping strength. This is very important as we apply multiple pumps to the system, as extra frequencies detune need to be considered for all the processes to reach the designed rates. A more detailed comparison between the experimental data and simulation results shown in this section will be discussed in the next chapter.

E. Conclusion

In this chapter, we introduced a pair of linked theoretical proposals that address the bath engineering the steady-state population and decay rates of photonic systems. In the first (dubbed a 'photon chemical potential'), by a parametrically coupling the photonic system to be controlled (a transmon qubit in our case) to a finite-temperature (and hence also low-frequency) auxilliary mode, the system can equilibrate to the temperature of the bath, with a tunable chemical potential that is controlled by the parametric drive. We discuss how to implement this proposal with a JPC with one arm at very low frequencies, and the other hyridized with a transmon qubit. This works in principle but has practical challenges as one of the mode frequency is one order of magnitude lower than the conventional JPC mode frequencies.

We next explained a more promising variation of this protocol, which is to have the transmon mode coupled to a single lossy SNAIL mode. By parametrically driving the SNAIL, we can trigger the 'heating' and 'cooling' processes for the qubit independently, and no longer depend on the SNAIL-mode having a low frequency and finite temperature (in fact it is preferable to have it at frequency not too dissimilar from the qubit). Detailed numerical simulations show that we indeed have independent control of the heating and cooling processes, and can implement them jointly provided we compensate for cross-Kerr related frequency shifts in the system. Therefore the photonic system with a controllable chemical potential can be realized with the carefully chosen drive conditions. In the next chapter, we show the experimental realization of both methods (JPC- and SNAIL-based) and compare our simulation results to the data.

V. From Hamiltonian to microwave design

A. Overview

In the previous chapter, we clarified the design the corresponding Hamiltonian we will use for the experiment. The next step requires us to transform the numerical simulation parameters into the target values that can guide the microwave design, and then into physical modes in metal cavities and on sapphire chips. The technique needed for the task is called 'black box quantization' (BBQ). In this chapter, I will use the qubit-cavity and qubit-SNAIL coupling as examples to demonstrate how we can use the BBQ method to make the connections between the parameters in physical microwave design and terms in Hamiltonian and to arrive at functional, practical devices.

B. Black box quantization

Black box quantization [122] is a semi-classical method that is originally used to determine the effective quantum Hamiltonian of a superconducting circuit that contains a Josephson junctions coupled to electromagnetic environments. This method teaches us how to take the simulation result we obtain in the microwave simulation software (like HFSS) and transform it into the coefficients of our Hamiltonian. It is designed for calculating the anharmonicity and dispersive shift for a qubit-cavity system, but it can easily extend to the calculation of third order couplings between the modes, like a qubit coupling to a SNAIL in our chemical potential project.

Let us review how the method works for the qubit-cavity system as a start. The theory treats the fourth order terms as perturbations. Therefore, the junction will be viewed as two parts: a purely nonlinear element whose energy is given by $E_J(1-\cos(\varphi)) - (E_J/2)\varphi^2$, a linear inductor with inductance $L_{J0} = \varphi_0/I_0$ and a linear capacitor with capacitance C_s, as shown in Fig. 41(a). Then the linear part of this model will be absorbed into the linear

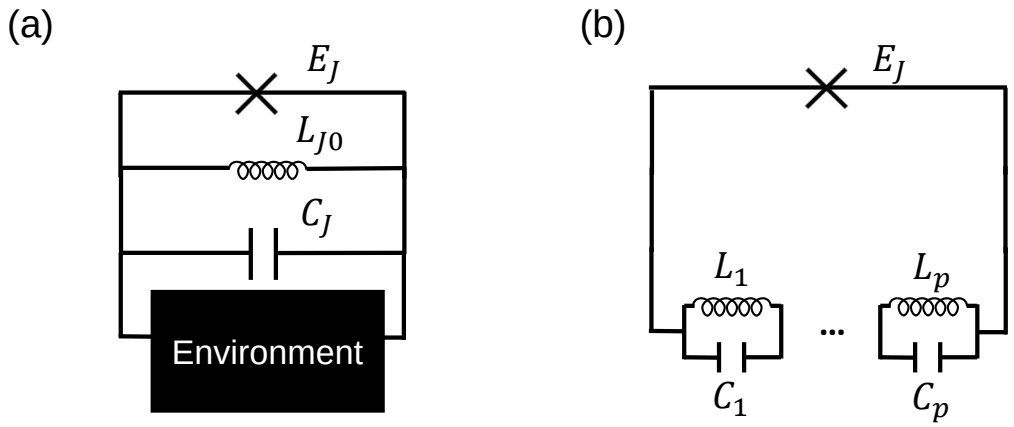

Figure 41: **Schematic of black box quantization.** (a) A transmon qubit couples the environment. The transmon is viewed as three different parts. The nonlinear part of the junction with Josephson energy E_J (represented by the cross symbol), the linear inductance L_J and the capacitance C_J. (b) The linear part of the transmon is absorbed into the environment black box. The modes in the environment is synthesized by an equivalent circuit of several parallel LC oscillators in series using Foster's theorem. Adapted from [122]

.

modes of the system (cavity mode) and together they form the 'black box' environment seen by the qubit. According to Foster's theorem [123], this black box can be synthesized by an equivalent circuit of several parallel LC oscillators in series, as in Fig. 41(b). Then the Hamiltonian of the system can be written as:

$$H = \Sigma_p(\frac{C_p Q_p^2}{2} + \frac{L_p \Phi_p^2}{2}) - \frac{1}{24} E_J \varphi^4 \tag{V.1}$$

where C_p, L_p, Q_p and Φ_p are the linear capacitance, inductance, charge and flux of the mode p respectively. To write it in terms of creation and annihilation operators use the same quantization technique in Ch. II, we have:

$$H = \Sigma_p \hbar \omega_p a_p^\dagger a_p - \frac{1}{24} \varphi^4 \tag{V.2}$$

where $\omega_p = 1/\sqrt{L_p C_p}$ is the frequency of each mode. In the case of a qubit-cavity system, $p = q, c$ for qubit and cavity. φ is the flux across the nonlinear part of the junction and Kirchhoff's law requires that $\varphi = \Sigma_p \Phi_p / \varphi_0$:

$$\varphi = \Sigma_p \sqrt{\frac{\hbar}{2} Z_p^{eff}} (a_p + a_p^\dagger) \tag{V.3}$$

where Z_p^{eff} is the effective impedance of each mode seen by the junction. Note that the treatment here is effectively the same as the diagnolization we did for a coupled qubit-system in Ch. II. Now the question becomes how to determine the value of Z_p^{eff} from the microwave simulation. The expression is given by the admittance $Y(\omega)$ with:

$$Z_p^{eff} = \frac{2}{\omega_p \mathrm{Im}[Y'(\omega_p)])} \tag{V.4}$$

and the resonator frequency of each mode can be identified by the zero point of the imaginary part of the admittance: $\mathrm{Im}[Y(\omega_p)] = 0$. The admittance function $Y(\omega)$ can be obtained from the microwave simulation software like HFSS. Then by finding its zero point and the slope at that point, we are able to calculate the quantization coefficients of each mode, and then by substituting them into Eq. V.2 and Eq. V.3, and expand the fourth term, we will be able to write down the important parameters like frequency, anharmonicity and dispersive shift. We can then tune the geometry of the design (like the size of the cavity, position of the qubit, size of the qubit antenna, ect.), and simulate the $Y(\omega)$, repeat the same calculation until we get the desired the Hamiltonian as we will show in Ch. VI.

Similarly in the SNAIL calculation, we will treat the third order terms as the perturbations. Now the Hamiltonian is:

$$H = \Sigma_p (\frac{C_p Q_p^2}{2} + \frac{L_p \Phi_p^2}{2}) + c_3 \varphi^3 \tag{V.5}$$

where c_3 is the third order coefficient we get from a SNAIL calculation, as will be discussed in next section.

C. SNAIL coefficient calculation

As we discussed in Ch. II, the SNAIL Hamiltonian as in Eq. II.49, can be Taylor expanded near its energy minimum φ_{min}, as shown in Eq. II.50. Let $\tilde{\varphi} = \varphi - \varphi_{min}$, we have:

$$H_{SNAIL} = c_2\tilde{\varphi}^2 + c_3\tilde{\varphi}^3 + c_4\tilde{\varphi}^4 + ... \tag{V.6}$$

with

$$\begin{aligned} c_2 &= \frac{1}{6}E_J(\cos(\frac{\varphi_{ext} - \varphi_{min}}{3}) + 3\alpha\cos(\varphi_{min})) \\ c_3 &= \frac{1}{54}E_J(\sin(\frac{\varphi_{ext} - \varphi_{min}}{3}) - 9\alpha\sin(\varphi_{min})) \\ c_4 &= -\frac{1}{648}E_J(\cos(\frac{\varphi_{ext} - \varphi_{min}}{3}) + 27\alpha\cos(\varphi_{min})) \end{aligned} \tag{V.7}$$

and φ_{min} is determined by finding the extreme point of the energy:

$$\frac{\partial H_{SNAIL}}{\partial\varphi}|_{\varphi=\varphi_{min}} = E_J\alpha\sin(\varphi_{min}) - E_J\sin(\frac{\varphi_{ext} - \varphi_{min}}{3}) = 0 \tag{V.8}$$

Once the circuit parameter α and E_J is determined, we can solve the SNAIL coefficient by first numerically get the value of energy minimum point as a function of the external flux: $\varphi_{min} = \varphi_{min}(\varphi_{ext})$. Then plug this result into the expression of each coefficients, we able to get $c_2(\varphi_{ext})$, $c_3(\varphi_{ext})$ and $c_4(\varphi_{ext})$.

As we want to use the SNAIL as a dipole element with a pure third order nonlinearity, we need to operate it at a fourth order cancellation point, that is the external flux which gives $c_4(\varphi_{ext}) = 0$. Then once we get this good operation point, we can calculate the second order coefficient $c_2(\varphi)$, which will lead to a linear inductance term used in the BBQ as:

$$L_s = \frac{\phi_0^2}{2c_2(\varphi_{ext})} \tag{V.9}$$

and the third order coefficient c_3 is like $-1/24E_J$ in the qubit-cavity example.

So to calculate the coupling between the SNAIL to another mode, with the same technique in the previous section to find the mode frequency and effective impedance, we get:

$$H = \Sigma_p\hbar\omega_p a_p^\dagger a_p + c_3(\Sigma_p\sqrt{\frac{\hbar}{2}Z_p^{eff}}(a_p + a_p^\dagger))^3 \tag{V.10}$$

the coupling strength we used in Ch. VI is obtained by expanding the cubic term.

D. User's manual for BBQ

The method we described in this chapter can be used in the calculation of other dipole element with different order of nonlinearity. And the nonlinear element can couple to different modes in the system, so that a multi-wave coupling can be generated. To follow this method, we need to:

A. First calculate the behavior of the nonlinear element, expand its nonlinear potential around its energy minimum point.

B. We will then be able to separate the linear part (second order term) from the higher order terms in which we will keep the lowest order as a perturbation of the system. The linear term will be absorbed into the black box seeing be the pure nonlinear part of the device and lead us to a more generalized Hamiltonian:

$$H = \Sigma_p(\frac{C_p Q_p^2}{2} + \frac{L_p \Phi_p^2}{2}) + c_n \varphi^n \tag{V.11}$$

where c_n is the coefficient of the corresponding nonlinear term. Here we assume we are using the Josephson junction based device, so the nonlinearity comes from the flux part of the device. The Hamiltonian can be quantized using Eq. V.4, with the effective impedance and mode frequency obtained from the data of the microwave simulation.

C. Then due to the Kirchhoff's law: $\varphi = \Sigma_p \Phi_p / \varphi_0$. We can re-write the Hamiltonian in the form of the operators. Note that the Foster theorem takes care of the mode diagonalization, so the mode we get in the final Hamiltonian is already in the dressed basis. Then the Kirchhoff's law indicates that the nonlinearity from the bare mode of the nonlinear device is distributed into all the dressed modes, with a weight given by the effective impedance seen by the element. The magnitude of this effective impedance is determined by the coupling strength between a certain mode to the nonlinear mode which will then reflect in the amplitude of the coupling terms in the expansion.

For the interested reader, he laboratory has since largely switched to the Energy participation ratio form of BBQ [124] for the similar tasks but it is faster to simulate. We also note that a more complicated theory is needed for the system with multiple nonlinear devices with different order of nonlinearity, there are currently theory treatments for this

type of problems in [125], and more careful understanding is needed for connecting it with the microwave simulation results.

VI. Qubit-bath engineering via parametric drive: Experiment

A. Overview

In this chapter, we introduce experimental realizations for the proposals we discussed in the previous chapter. This chapter is organized as follows: We begin in Sec. VI.B by introducing the how to directly implement the original theory proposal via a low frequency JPC. We will discuss the design and fabrication of the sample, as well as the practical issues which hampered this implementation. In Sec. VI.C, we demonstrate bath engineering by instead parametrically coupling a qubit to a lossy SNAIL mode. We discuss the design and fabrication of the samples and focus on comparing the data to the simulation result in the previous chapter. Next, in Sec. VI.D, we discuss the significance of this experimental platform and its potential application in other projects.

B. Low frequency JPC

1. Transmission line based low-frequency JPC

In this section, we are going to talk about the experimental implementation of the original Hafezi proposal [70] with a low frequency JPC. As we discussed in the previous chapter, this low frequency design has a few special requirements compared to a conventional JPC with more usual signal and idler frequencies ($5 \sim 12$ GHz). Firstly, we need a large bandwidth at the very lower frequency (idler) mode so it can decay rapidly. Secondly, there should be no harmonic of the idler or common mode near the pump frequency, so that the parametric pump can be considered to be 'stiff'. Thirdly, there should be enough coupling between the low and high frequency mode so the parametric process can be driven with a moderate strength that will not trigger other undesired higher order effects. Finally, high frequency (signal) mode needs to have a low bandwidth, that is, the photons need to live long enough

for the thermalization to be done, and it should be relatively anharmonic (that is, a qubit).

Since the modes in a conventional JPC live use transmission line based $\lambda/2$ resonators, a low frequency mode can be realized by using a long transmission line that can hold the standing wave with the correspondingly long wavelength. However, there will be many higher harmonics of this low frequency mode. To prevent them showing up near the signal mode, we need to integrate a band pass filter into the idler resonator. The filter is designed using a impedance engineering technique [126, 127]. It consists of alternating sections of high and low impedance coplanar waveguide transmission lines which result in a wide stop band near the signal frequency with carefully chosen parameters. In Fig. 42(a) we show the design of the low frequency JPC with the built in filter simulated in Microwave Office (a microwave circuit simulation software). Figure 42(b) is the schematic of each unit cell of the filter that consists of a low and high impedance transmission line. Figure. 42(c) shows simulation result for the transmission coefficient from 'idler' port to the 'signal' port. There is a clear stop band (below 50 dB attenuation) from $6 \sim 9$ GHz which prevents the higher harmonics of the common and idler modes from appearing near the pump frequency and signal mode.

This design was realized with etched Nb resonators on a silicon chip provided by the Houck group at Princeton University. A picture of the chip and sample mount (also provided by the Houck laboratory) is shown in Fig. 43. The next step was to fabricate the JRM onto the device. In Fig. 44 we show the optical images of the different JRMs we used in the experiment. Figure. 44(a) demonstrates the first version of JRM we worked with, which has shunted linear inductors to prevent hysteresis. However, this extra inductance will also decrease the participation ratio of each mode, resulting in a lower coupling strength between the modes which makes it harder to drive the desired parametric processes. Thus, in order to achieve a higher participation ratio, we get rid of the shunted linear inductors and created the second version of the JRM, as shown in Fig. 44(b).

We were able to perform basic measurements on this second JPC (note: a qubit had not been added yet to hybridize with the signal mode). In Fig. 45, we show the reflection phase data of the 'idler' and 'signal' mode of the device. The accurate frequency and bandwidth of each mode can be obtained by fitting the data to a reflection model. The low frequency 'idler' mode is at 230 MHz with a bandwidth of 18 MHz ($Q_{ext} = 13$ and $Q_{int} = 2653$) and

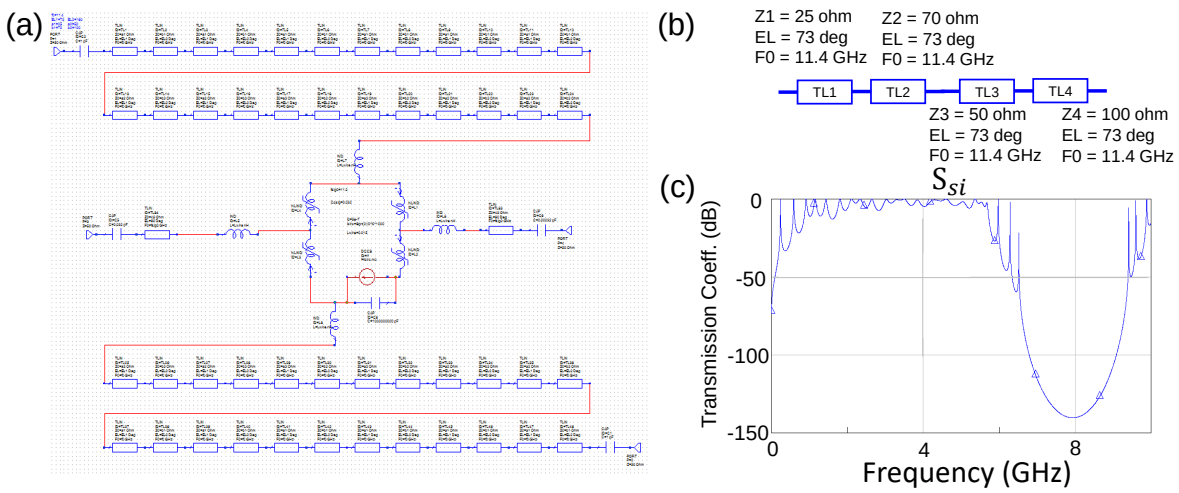

Figure 42: **Bandpass filter design for low frequency JPC.** (a) The schematic of the low frequency JPC with bandpass filter in microwave office. The single mode is simulated as two transmission lines connect to the JRM with linear inductors. The idler mode is made with a group of transmission lines of alternating sections of high and low impedance transmission lines. The JRM in the center is simulated with four identical non-linear inductors. The current source is used to simulate the external flux that goes through the JRM. (b) The unit cell that builds the bandpass filter. The idler arm is made with this cell being repeated several times. (c) The simulation result of the transmission coefficient from ideler port to signal port as a function of frequency. We can see a clear stop band near the pump frequency as expected.

the high frequency 'signal' mode is at 7.255 GHz with a bandwidth of 2 MHz ($Q_{ext} = 4896$ and $Q_{int} = 5966$).

Now, with the modes at the desired frequencies, we need to parametrically drive the device as we discussed in the previous chapter. As the signal mode is not anharmonic, the chemical potential behavior will not appear, but we can characterize the parametric drives by studying the gain and conversion behavior of this rather exotic JPC. In Fig. 46 we show the results of the strongest gain and conversion process we could achieve in this device. The

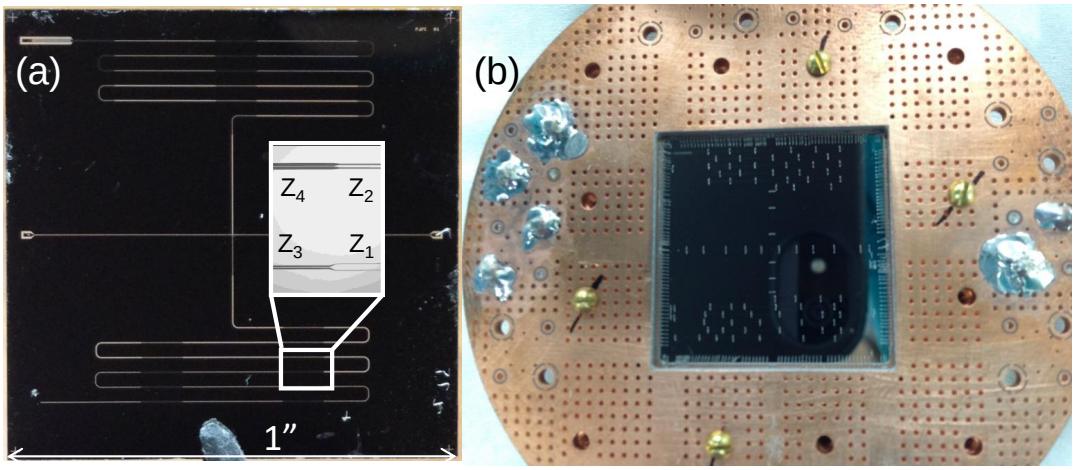

Figure 43: **Optical images of low frequency JPC.** (a) Optical images for the JPC chip. The straight horizontal transmission line resonator is the signal mode. The meander transmission line with varying width is the idler mode that has filter built in. The inset shows a zoomed-in image of the unit cell of the filter that corresponds to Fig. 42(b). (b) Image of the JPC chip loaded in the sample holder. The wire bonds throughout the sample edge and surface are to better connect the ground plane to get rid of other undesired parasitic modes.

gain of a JPC is given by [83]:

$$\sqrt{G} = \frac{1 + |\rho_0|^2}{1 - |\rho_0|^2} \tag{VI.1}$$

and the dimensionless pump amplitude ρ_0 is given by:

$$\rho_0 = \frac{2g_3\sqrt{\bar{n}_p}e^{-i\varphi_p}}{\sqrt{\kappa_s\kappa_i}}. \tag{VI.2}$$

where κ_s and κ_i are the bandwidth of the signal and idler mode respectively, g_3 is the third order coupling term for the JPC, $\bar{n}_p$ is the average pump photon number, and φ_p is the pump phase. So with κ_s and κ_i and G, we can calculate the parametric coupling strength for the gain, $g_G = g_3\sqrt{\bar{n}_G} = 0.72$ MHz, and conversion, $g_C = g_3\sqrt{\bar{n}_C} = 1.1$ MHz.

As we discussed before, the photon in the signal mode should live long enough for the thermalization process to finish, that is, the rate of the parametric drive should be faster than the decay rate of the signal mode: $g_G > \kappa_s$ and $g_C > \kappa_s$. Unfortunately, this is not the

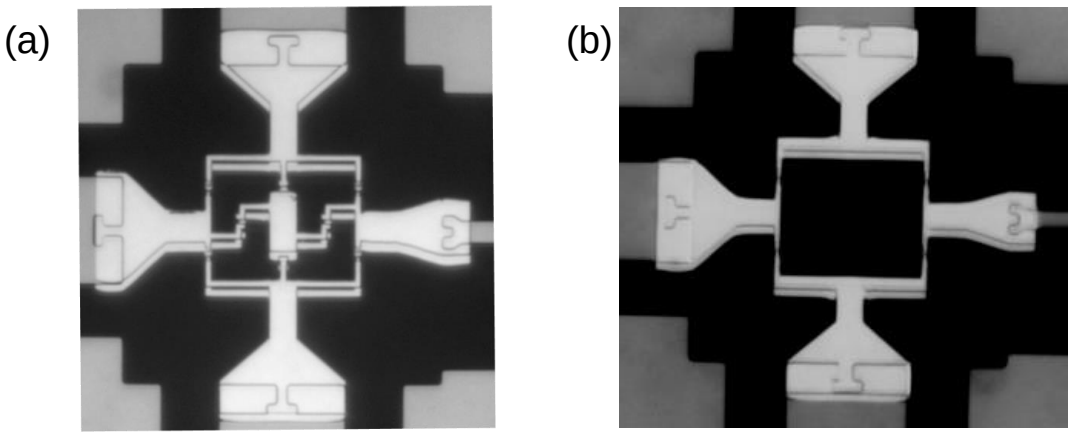

Figure 44: **Optical images of the JRM.**(a) The picture of the first version of the JRM with linear shunting inductors in the middle to prevent hysteresis. (b) The picture of the JRM we used in the final version of the device. We eliminated the shunting inductors to achieve a higher JRM participation ratio and hence stronger three-wave couplings.

case for this device, where $\kappa_a = 2$ MHz. There are two reasons for this: firstly, in order to make a mode with a frequency one order of magnitude lower than the conventional value, we have to use a long transmission line as the resonator which will introduce large linear inductance and thus lower the participation ratio (see Eq. IV.10) of the mode. And for the third order coupling strength g_3 [80]:

$$g_3^2 \propto p_s p_i p_c \omega_s \omega_i \omega_c \tag{VI.3}$$

where p_i is the participation ratio of each mode. So, it is clear that a low frequency, low participation ratio mode will decrease the third order coupling strength. Given that we are limited in how much pump power we can apply to the dilution refrigerator without heating the fridge, and that higher-order nonlinearities can also be activated by too-strong pumping, this places an ultimate limit on the achievable parametric pumping rate. Both issues were problematic in this sample, though we believe the latter was the ultimate limitation. Secondly, because we were not able to make an excellent superconducting contact between the Nb (resonator) and Al (JRM), which resulted in a low internal Q of the signal mode.

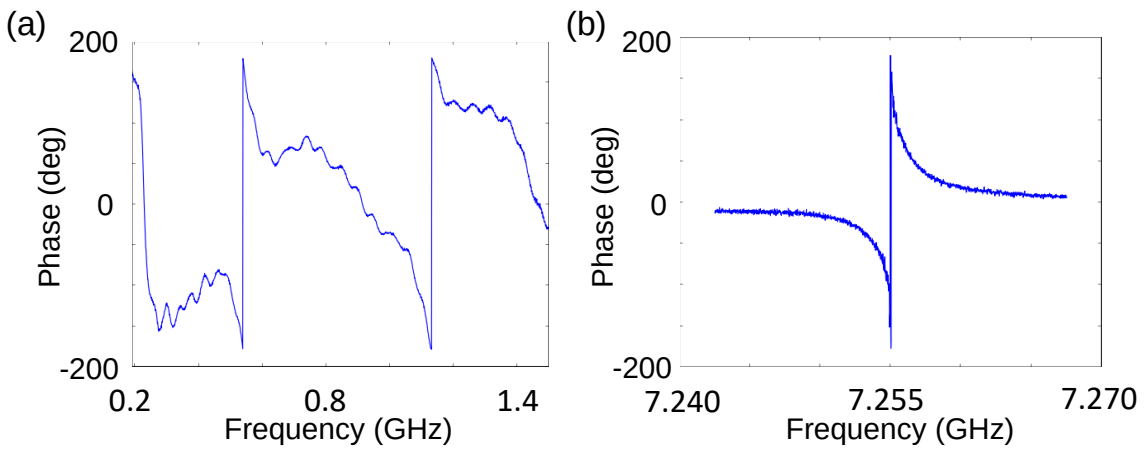

Figure 45: **Phase data of the modes of the low frequency JPC.** The reflected phase as a function of frequency for the (a)idler and (b)signal mode. Note that there are several idler harmonics, with the lowest at 0.2 GHz. The internal and external Q of each mode can be extracted by fitting the data (including amplitude response which is not shown) to a reflection model.

2. Lumped low-frequency JPC

To address the participation issue, We next tried to improve the JPC idea by fabricating a lumped version which replaced the transmission line with parallel plate capacitors. A schematic of this lumped idea is shown in Fig. 47. In this circuit, the low frequency can now be achieved by with a large, lumped capacitor (with minimal stray inductance compared to a long transmission line shown in Fig.7), and thus the participation ratio can be higher than the old design. More, there will be no higher harmonics of the idler mode near the signal mode, and so the device requires no internal filter.

This design was first simulated using Ansys' High Frequency Structure Simulator (HFSS) software. The 3D model for the lumped JPC is shown in Fig. 48(a). The structure (and hence fabrication) of a lumped JPC is more complicated than a transmission line based JPC. We first need to lay down a layer of NbTiN (yellow) on the Silicon chip (light blue) using optical lithography technique as the ground plane. This material has advantages over

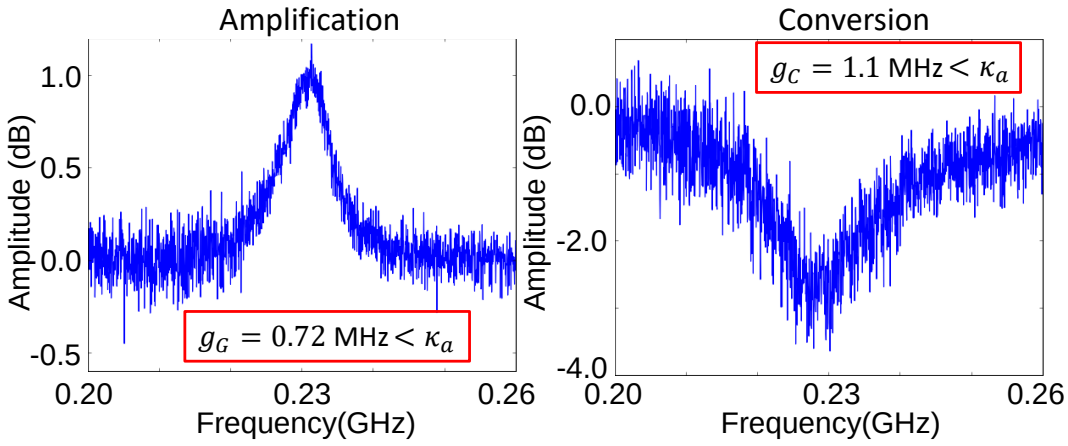

Figure 46: **Gain and conversion data for low frequency JPC.** The amplitude of the reflected signal as a function of frequency near the idler mode when the device is operated in the (a)amplification and (b)conversion mode. The result shown here is the maximum gain/conversion we could achieve from this device. The rate of the parametric processes can be calculated from Eq. VI.2 (see text for more details).

other choices such as Nb and Al in terms of making contact to subsequent aluminum layers, however, in this fabrication it is primarily used as it was a fabrication process the lab had good experience with. Then, a layer of e-beam evaporated sapphire (orange) is deposited through and optical mask on top of the ground plane to serve as the dielectric layer for the lumped capacitors. Finally, the junctions and the top pad of the capacitor is deposited on the top of the sapphire layer using the E-beam lithography technique. A zoomed picture of the device is shown in Fig. 48(b). Here we can see the JRM is placed in the center, where the capacitor pads (dark blue) of signal (vertical pad) and idler (horizontal pad) cross each other. The capacitance of each mode (c_a and c_b in Fig. 47) is determined by the pad area that overlaps with the ground plane (yellow).Therefore the capacitor pad of the idler mode is much larger compare to that of the signal mode, as the idler frequency ($\sim$ 300 MHz)is one order of magnitude lower than the signal frequency ($\sim$ 7 GHz). The coupling capacitor is formed by the top pad (dark blue), the dielectric layer (orange) and the external transmission line (green) that is on the same layer as the ground plane. Thus, the the external coupling

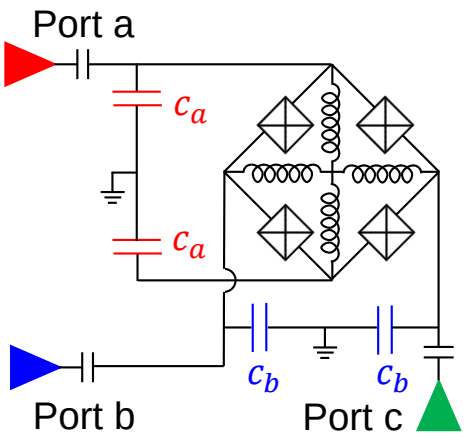

Figure 47: **Circuit schematic for lumped low frequency JPC.** The JRM is in parallel with two sets of capacitors to form the lumped resonators that replace the transmission line resonators in the microstrip JPC as in Fig. 7. By minimizing the linear inductance in the device, we raise the participation ratio of each mode and thus increase the coupling strength between the modes.

strength of each mode is controlled by the overlapping area between the top pad and the transmission line. The inset of Fig. 48(b) shows the structure of the JRM, which is very similar to the JRM in a microstrip JPC, there are four small junctions (little red pad) on the outer arm of ring of the JRM and large shunted linear inductors (the red cross) in the middle of the ring. For future Hatlab reference, the HFSS file of this design is located in: F:/HFSS/LJPC.

Once the device is successfully fabricated, it follows the same step as a microstrip JPC to be assembled. The amplifier chip will first be glued to the copper sample box as in Fig. 7(d) using silver paste. Then it is mounted on a copper holder with a magnetic coil attached to it. The whole device is placed in a Aluminum shield that is inside another cryoperm shield made with high-μ metal to prevent influence from external field fluctuations.

However, we are not able to see a clear mode nor a gain/conversion process near the designed low frequency. There could be potential issue in the output channel as we don't

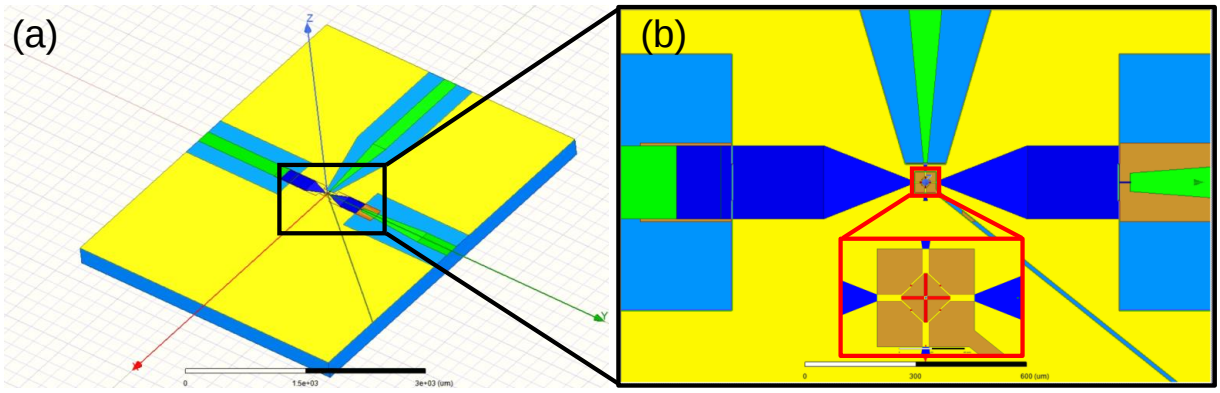

Figure 48: **3D model for lumped low frequency JPC in HFSS.** We try to implement the a lumped JPC. Our design is modeled in HFSS to determine the design parameters for right mode frequencies. (a) An overview of the device that couples to the external transmission lines (green). (b) A zoomed in picture shows the details of the lumped JPC. The whole device is made on the sapphire chip (light blue) with a layer of ground plane (yellow) made with NbTiN on top of it. Then, another layer of sapphire (orange) is deposited on top of the ground plane at designated area. Finally the top pad of the lumped capacitor (dark blue) and junctions and linear shunts(red) are deposited on the top of the sapphire. See text for the details of the fabrication. Inset: a zoomed picture of the JRM.

have a good circulator/isolator that is designed to work at such low frequency. It could also be there is some bad connections between the chip and the external transmission line that happens at the packaging stage when preparing the sample. There are two reasons we did not keep pushing on this design. Firstly, according to the result of other lumped JPCs made by my colleagues [120], the internal Q are still on the order of a few thousand which is still not enough for our need (~ 10000). More, to completely implement the proposal, we need to add a qubit-cavity system onto the chip while engineering the qubit to have a strong enough coupling between the signal mode while maintaining a decent coherence time. This raises extra complexities for the design and fabrication process. Secondly, as we worked through the project, we come up with a simpler, yet more promising design using a 3D transmon and a lossy SNAIL which we will discuss in the next section.

We do believe the difficulties we are having with this lumped low frequency JPC can be solved with a more careful fabrication and trouble shooting with the input/output lines of the fridge. While we found that the lossy SNAIL is indeed more promising for this particular project, the idea of using lumped elements to design a JPC with a mode whose frequency is lower than the conventional value still has potential uses.

C. Qubit parametrically coupled to a lossy SNAIL

1. Microwave design and fabrication of the sample

Before we start to introduce the final version of our design I want to briefly mention a transitional design between a low frequency JPC version and a lossy SNAIL version. We still try to create a three-wave coupling between a non-linear mode and a low frequency mode through a SNAIL. But, instead using a transmission line based resonator in the JPC, we directly use a transmon qubit and a resonator with large inductance provided by an array of junctions [128, 129]. The schematic of this design is shown in Fig. 49(a). The transmon, SNAIL and the low frequency resonator is fabricated on the sample chip which will be placed in a two-part sample holder. The Aluminum part is a 3D coaxial cavity which will be used for qubit readout and the Copper part has a tube in it for placing the sample and allows the external flux to go through the SNAIL. In design, we directly couple a low frequency mode to an anharmonic mode, so there will be no more needs of integrating a qubit onto the amplifier chip as we would have to do in the JPC version. And given the typical life time of a transmon in an Aluminum cavity ($\sim 30 - 50\mu s$), the photon in the qubit can live long enough for the thermalization process to be finished provided the system could have a similar coupling strength as that in the JPC version. However this design is less ideal as we have difficulties seeing the coupling between the SNAIL and the lower frequency resonator mode in the HFSS simulation and there are two major challenges for fabrication: firstly, the large area of the antenna pad will need a long writing time during which the beam may be drifting. Secondly, there is a non-trivial chance that some of the junctions are bad in the

low frequency mode due to the large number of Josephson junctions.

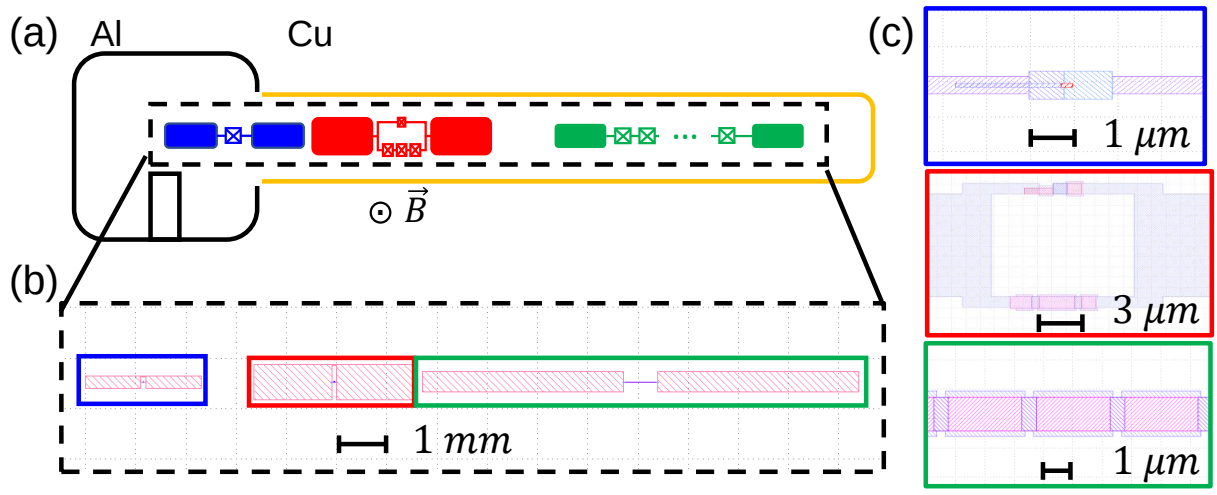

Figure 49: **Summary of the 'three-mode' version with SNAIL and array low frequency resonator.** (a) Schematic of the new 'three-mode' design. A transmon qubit (blue) is coupled to a low frequency mode (green) through a SNAIL mode (red). The low frequency mode is achieved by using a junction array shunted with an antenna capacitor. The chip is placed in a two-part sample holder. The aluminum part is a 3D coaxial cavity which will be used for qubit readout and the Copper part has a tube in it which holds the SNAIL and low-frequency modes and allows the flux tuning of the SNAIL. (b) The klayout file of the design. (c) Zoomed in picture that shows the details of the junctions used in the three components. The qubit is designed to be 4.3 GHz with an anharmonicity of 180 MHz, the SNAIL is design to be at 9 GHz, and the low frequency mode is designed to be at 300 MHz.

We still faced challenges hybridizing with the low-frequency mode due to the use of too much inductance lowering the participation ratio. This remains a problem even with the 'three-mode' design. Happily, while we were still searching for a solution, another ongoing project in lab inspired us. In that project, we were trying to build a microwave laser (maser) using a system consisting of a lossy SNAIL which controls a transmon qubit to form the masing medium. The transmon is in turn resonantly coupled to a high Q (maser) cavity. Simulations for the maser project showed that by detuning the transmon and cavity and

driving the SNAIL and transmon in same way as we would do for a gain process in the JPC, we are able to achieve a 'maser ratchet', that is, to see the population inversion on the qubit. In retrospect, this is directly the 'heating' component we wish for our chemical potential project, as described in the previous chapter. Thus, we arrived at our final and very successful implementation of the 'photon chemical potential'. We modified our plan from Fig. 49 to the final version, as shown in Fig. 50(a). Here we just get rid of the low frequency mode with the junction array as we no longer need the low frequency mode, and rely on multiple parametric drives to give control of bot the transmon temperature and relaxation rates. Similar to the previous case, we now put both the transmon and SNAIL on the same chip. This chip is then placed in the same two-part sample holder. In Fig. 51, we show the final version of the 3D model we used for the microwave design in HFSS. The junctions for the qubit and SNAIL are modeled as a lumped inductor. The inductance is set as the linear inductance value for the qubit and SNAIL at superconducting temperature. In our case, we choose the qubit inductance to be $L_q = 10$ nH and the SNAIL inductance to be $L_s = 0.1$ nH which is the inductance value for the SNAIL at fourth order cancellation point, see AppendixV.C. These values correspond to an transmon junction with a critical current $I_{q0} = 0.03\ \mu A$, and SNAIL with the E_J ratio of $\alpha = 0.23$ and a large junction critical current $I_{S0} = 1.32\ \mu A$ at flux point $\varphi_{ext} = 0.76\pi$.

We use the original, admittance-based black-box quantization (BBQ) method [122] to transfer the design parameters into the coefficients of the device Hamiltonian. As a note to the interested reader, the laboratory has since largely switched to the Energy participation ratio form of BBQ [124] as it is faster to simulate, but this design predates its adoption. We obtain the parameters related with the qubit-cavity coupling by adding a lumped port to the transmon junction in the file. We ignore contributions due to the SNAIL to avoid the difficulties of multi-mode BBQ, but this simplification is reasonable as the SNAIL should be biased to have no 4th order terms in its Hamiltoninan. As is usual in BBQ, by looking at the zero crossing point of the imaginary component of the impedance function Fig. 52, we can calculate the frequency and anharmonicity of the qubit, the frequency of the cavity, and the dispersive shift between them, see AppendixV.B.

Another important set of parameters is related to the SNAIL's third order nonlinearity

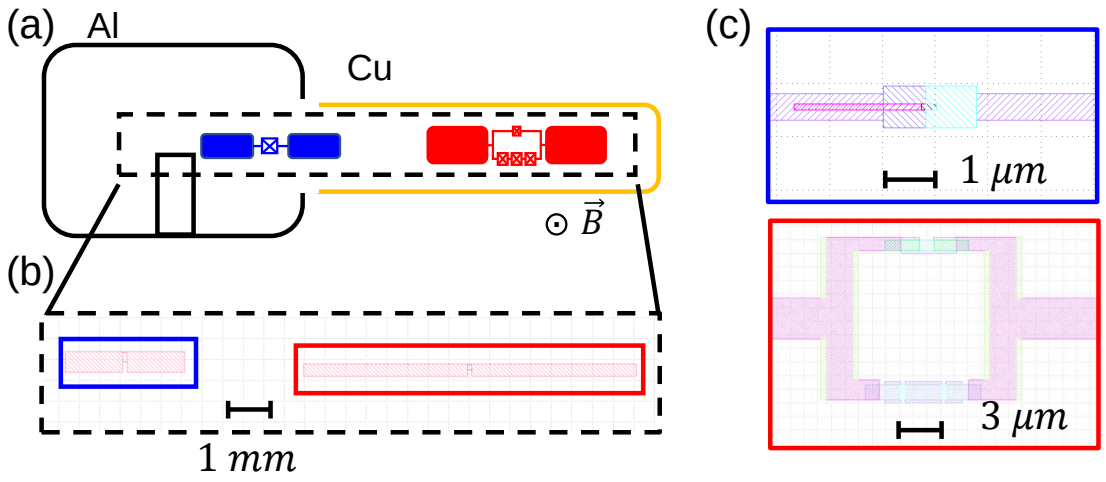

Figure 50: **Summary of the chemical potential with lossy SNAIL.** (a) Schematic of the new lossy SNAIL design. A transmon qubit (blue) is directly coupled to a SNAIL mode (red). The chip is placed in a two-part sample holder. The aluminum part (black) is a 3D coaxial cavity which will be used for qubit readout and the Copper part (orange) has a tube in it for placing the sample and allows the flux tuning of the SNAIL via an external coil. (b) The klayout file of the design. The transmon center line is designed to be higher than the center line of the SNAIL. This is because we try to get a higher dispersive coupling between the qubit and cavity by moving it to a area with higher cavity field. Then the cavity bandwidth can be larger to perform a faster readout. (c) Zoomed in images which show the details of the junctions used in the three components. See text for detailed designed parameters.

and its coupling to the transmon. These are the equivalent of the 4th order self- and cross-Kerrs. We have adapted our BBQ calculations to expand assuming a third order term in the SNAIL junction, and ignoring the nonlinearity of the transmon (which is both not too anharmonic and has no native 4th order term). The BBQ calculation for third order is obtained by setting the lumped port on the SNAIL in the file and eliminating the port on the transmon junction. In particular, for this device we are interested in the term g_{abb}, which, as detailed in the previous chapter, allows us to pump the SNAIL (b) to create an effective

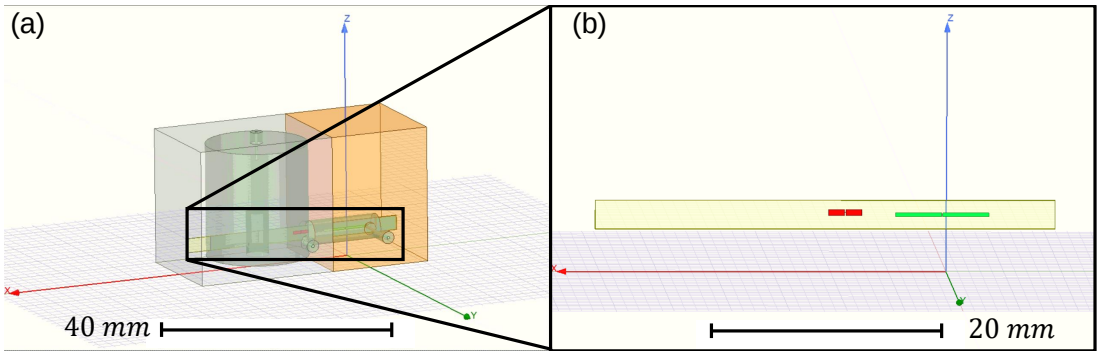

Figure 51: **HFSS design of a qubit couple to a lossy SNAIL.** The microwave properties are designed with the HFSS software. Here we show the 3D model we used for simulation in (a) and a zoomed picture of the chip in (b). Both the transmon qubit (red piece) and the SNAIL (green piece) is set close to each other on the same sapphire chip to create enough coupling between them. The cavity that holds the chip has two parts. The chip is then inserted into the cavity that has two parts. The aluminum part is a high Q 3D cavity that used for dispersive qubit measurement. The copper part is a circular waveguide that severs as an enclosure (in the same way as in Ref [130]) and enable us to apply external flux through the SNAIL. The chip is a double side polished sapphire. It is 40 mm long, and 2.5 mm wide with a thickness of 430 μm. The diameter of the tube in the copper part is 4 mm.

second order interaction between the SNAIL (b) and qubit (a). The details of both 'third order' and 'fourth order' BBQ are detailed in AppendixV.B. While our calculation method, handling one term per simulation is tractable, and has yielded good devices, it is clearly not ideal. In future work, it would be advantageous if we could develop an all-order, multi-mode calculation method, but that is beyond the scope of my thesis.

By adding a wave port boundary condition to the cavity port and SNAIL port, the coupling bandwidth of each port can also be extracted by fitting the reflection curve. Our simulation yields $\kappa_c = 0.6$ MHz and $\kappa_s = 16$ MHz. An estimate of the qubit life time can be obtained from the quality factor of the qubit mode in the eigenmode simulation: $T_1 = Q_q/\omega_q$.

The design parameters are: qubit frequency is 4.3 GHz with anharmonicity of 180 MHz.

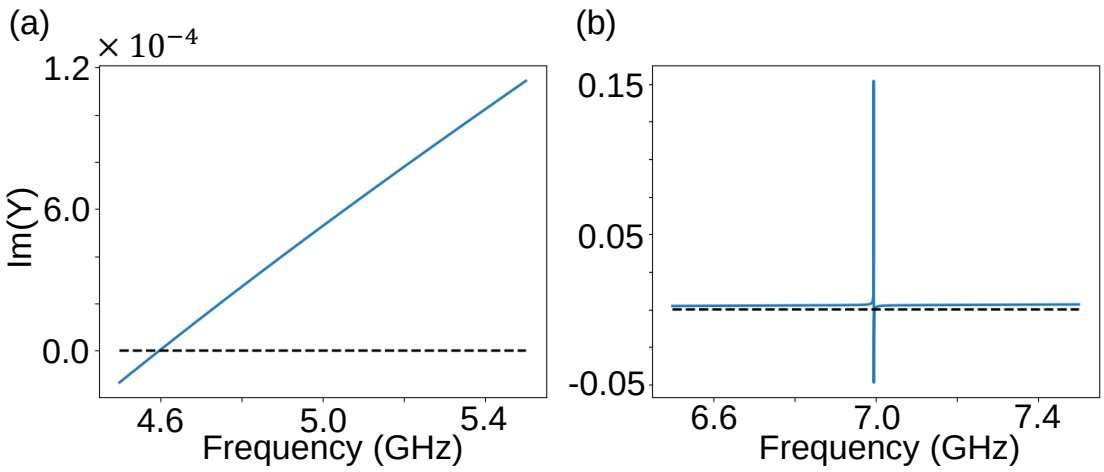

Figure 52: **Im(Y) from qubit lumped port.** Imaginary part of the impedance parameter as a function of frequency. The result is measured with the lumped port set on the qubit, that is the impedance seen by the qubit. Simulation results for the qubit mode and cavity mode are shown in (a) and (b) respectively. The zero points of the curves give the information about the mode frequencies and coupling strength. See appendixV.B for more details.

The simulated T_1 given by the eignmode simulation is $\sim$ 100 μs. The cavity frequency is 7.0 GHz with a bandwidth of $\kappa_c/2\pi = 0.6$ MHz and a dispersive coupling between the qubit and cavity $\chi_{qc} = 0.3$ MHz. The SNAIL frequency at the fourth order cancellation point is 9.0 GHz, with a bandwidth of $\kappa_s/2\pi = 16$ MHz, the third order coefficient for the SNAIl is $g_{sss} = 18$ MHz, with $g_{sq}/\Delta_{sq} = 0.01$, so the third order coupling between the SNAIL and qubit is $g_{ssq} = 0.17$ MHz.

The linewidth of the cavity and dispersive shift is chosen to so we can do a good qubit measurement (well separated Gaussian distribution on the I-Q plane) within a reasonable time ($\sim 1\mu s$). Note that there is a trade off between the dispersive shift and the coupling strength between the qubit and cavity. Move the qubit part into the Al part will provide a stronger disersive shift but less coupling to the SNAIL. The SNAIL linewidth is chosen to be larger to allow the fast decay of the photon in the SNAIL mode. The coupling strength is designed to be larger enough to support the parametric processes without causing a decrease

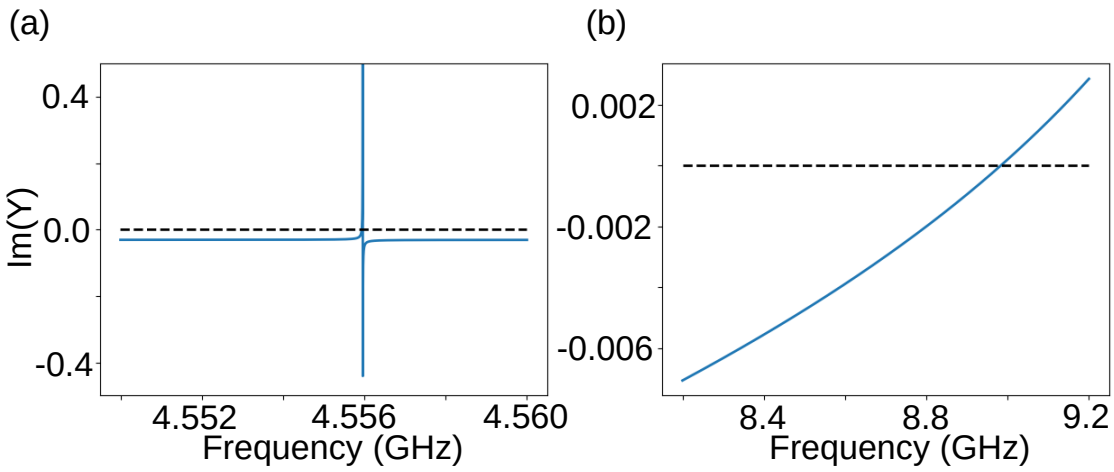

Figure 53: **Im(Y) from SNAIL lumped port.** Imaginary part of the impedance parameter as a function of frequency. The result is measured with the lumped port set on the SNAIL, that is the impedance seen by the SNAIL. Simulation results for the qubit mode and cavity mode are shown in (a) and (b) respectively. The zero points of the curves give the information about the mode frequencies and coupling strength. See appendix V.B for more details.

in the life time of the qubit through the Purcell effect. All the mode frequency is design to have no frequency collisions in the summation or the difference between any combination of modes to prevent triggering other undesired parametric processes.

We can then use the parameters in this file to draw our pattern for the fabrication. In Fig. we show the final Klayout file we used for the EBL writing. The position of the qubit and SNAIL and the size of the antenna pad is straight forward to acquire. The part that needs more attention is the junction areas for the modes. For qubit junction, as we know the desired linear inductance L_q, then the critical current of the junction is determined as $I_q = L_q/\varphi_0$ where φ_0 is the reduced flux quanta. The I_q sets the area of the junction as $A_q = I_q/\rho_I$ (ρ_I is the current density of the junction. This is a parameter sets by the fabrication conditions that needs to be calibrated for different fabrication platform). As for the SNAIL mode, the L_s we put in the HFSS is the desired linear inductance for the whole SNAIL at its fourth order cancellation point. We also want to keep the inductance

ratio between the small junction and larger junction in the SNAIL to be 0.23 to prevent the hysteresis in the mode. Then with the ratio and L_s we can determine the inductance of the small and large junction as in Sec. V.C, from which the area of each junction can be set in the same way as the qubit junction.

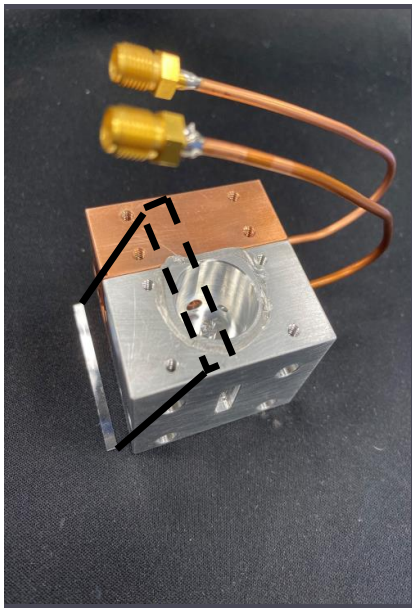

Figure 54: **Picture of the chemical potential experiment setup.** Both the qubit and SANIL is fabricated on the same sapphire chip shown in the bottom left of the picture. It is placed inside a two-part sample holder. The upper portion contains a copper tube which houses the SNAIL and has an external magnet for flux bias. The tube continues past the copper/aluminum junction and enters a 3-D post cavity. The transmon is partly in the cavity and partly in the tube, and couples to both the cavity and SNAIL. The whole device is coupled to external transmission lines through three different ports: the SNAIL port (on the Copper part), the weak port (on the Aluminum part) and the cavity port (goes into the Al cavity from the top through the lead that is not shown). See text for the purpose of each ports.

2. Experiment setup

Figure 54 shows a picture of the final chemical potential device. As we introduced in previous section, both the transmon qubit and the SNAIL are fabricated on the same sapphire chip. The chip is then inserted into the two-part sample holder, consisting of a copper tube which joins an aluminum tube which in turn enters a 3D post cavity [131].

The device connects to the external transmission lines through three different ports, the 'weak', 'cavity' and 'snail' port, as shown in the schematic in Fig. 55. The 'weak' port is designed to provide coupling to transmon for us to do drive transmon transitions but not strong enough to decrease the life time of the qubit through the Purcell effect. The measurement pulse is reflected from the 'cavity' port (where it is entangled with the state of the qubit) and then amplified by a TWPA provided by W. Oliver's Lincoln Lab group. The pump of the TWPA is combined with the measurement signal through a directional coupler. The 'SNAIL' port has the strongest coupling to the transmission line to provide enough photon loss rate of the SNAIL mode required by the protocol (it also makes parametric driving of the SNAIL easier). The parameteric drives are applied to this port through a directional coupler to allow us to monitor the output and identify the SNAIL mode frequency via the 'SNAIL diagnostic port'. Note that this port is used only in determining the bias condition for the SNAIL, and is not regularly monitored while bath engineering the qubit, and hence has no parametric amplifier. The external flux is created by a superconducting magnet coil mounted near the SNAIL, in the copper part of the sample holder (not shown in the figure).

3. Sample parameters

The Aluminum cavity in our experiment is 3D coaxial post cavity with a resonant frequency of $\omega_c/2\pi = 6.996$ GHz, coupling quality factors of $Q_{cavity} = 11,660$ on the cavity port and $Q_{weak} \sim 1,000,000$ on the weak port. Therefore, the cavity linewidth seen from the strong port is $\kappa_{cavity}/2\pi = 0.6$ MHz. The tube diameter in the copper part is 4.4 mm. The superconducting qubit is a 3D transmon qubit made by commonly used Dolan bridge technique with ground to excited state transition frequency of $\omega_{ge}/2\pi = 3.778$ GHz, anhar-

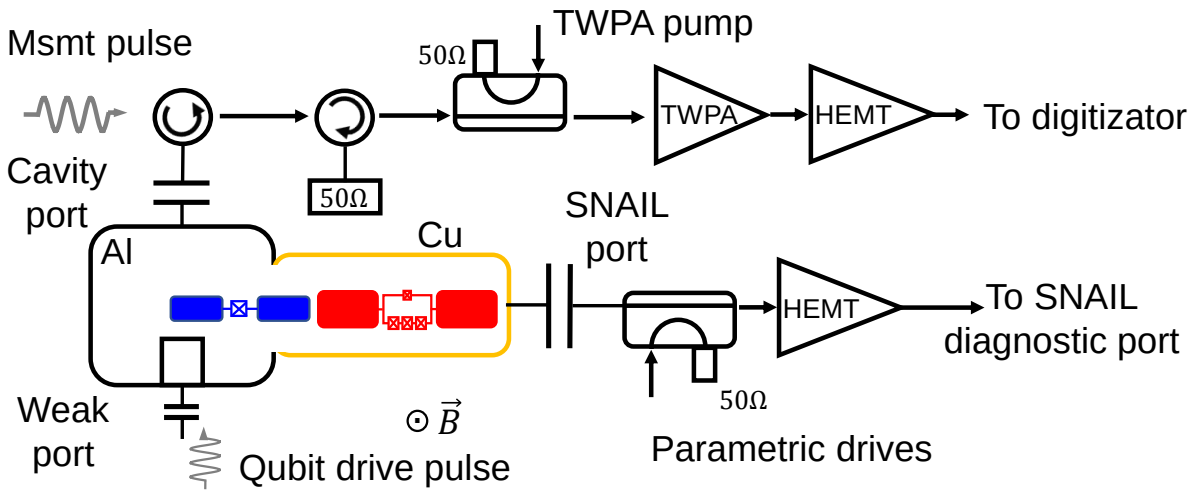

Figure 55: **Schematic of the chemical potential experiment setup.** The device is connected to the external environment through three different ports: weak port, cavity weak port and SNAIL port. Qubit drive pulses are sent through the weak port. Measurement pulses are reflected from the cavity port and them sent to the TWPA before finally being digitized at room temperature (not shown). The pump of the TWPA is also sent on this output line through a directional coupler. The coupling between the SNAIL port and system is designed be strong, in order to make the SNAIL both lossy and easier to drive. The parametric drives are sent through this port from a directional coupler, which also allows diagnostic measurement of the SNAIL for tuning.

monicity $\alpha = 180$ MHz, and a qubit-cavity dispersive coupling strength of $\chi/2\pi = 0.3$ MHz. This qubit has a T_1 of 15.6 μs, and T_{2R} of 8.5 μs (T_{2E} is 8.5 μs). The SNAIL is also made with the Dolan bridge technique with the frequency at zero flux of 9.2 GHz and frequency at operation point of 8.0 GHz (where we found experimentally that we could apply the strongest drives with the cleanest qubit response). The SNAIL is strongly coupled to the external environment with a coupling quality factors of $Q_s = 500$. The whole system is wrapped in aluminized mylar and mounted in a cryoperm shield (which is wrapped in a separate layer of aluminized mylar), with no external aluminum shielding. As shown in Figure. 56, the device is mounted at the base stage of an Oxford dry helium dilution refrigerator. The SNAIL

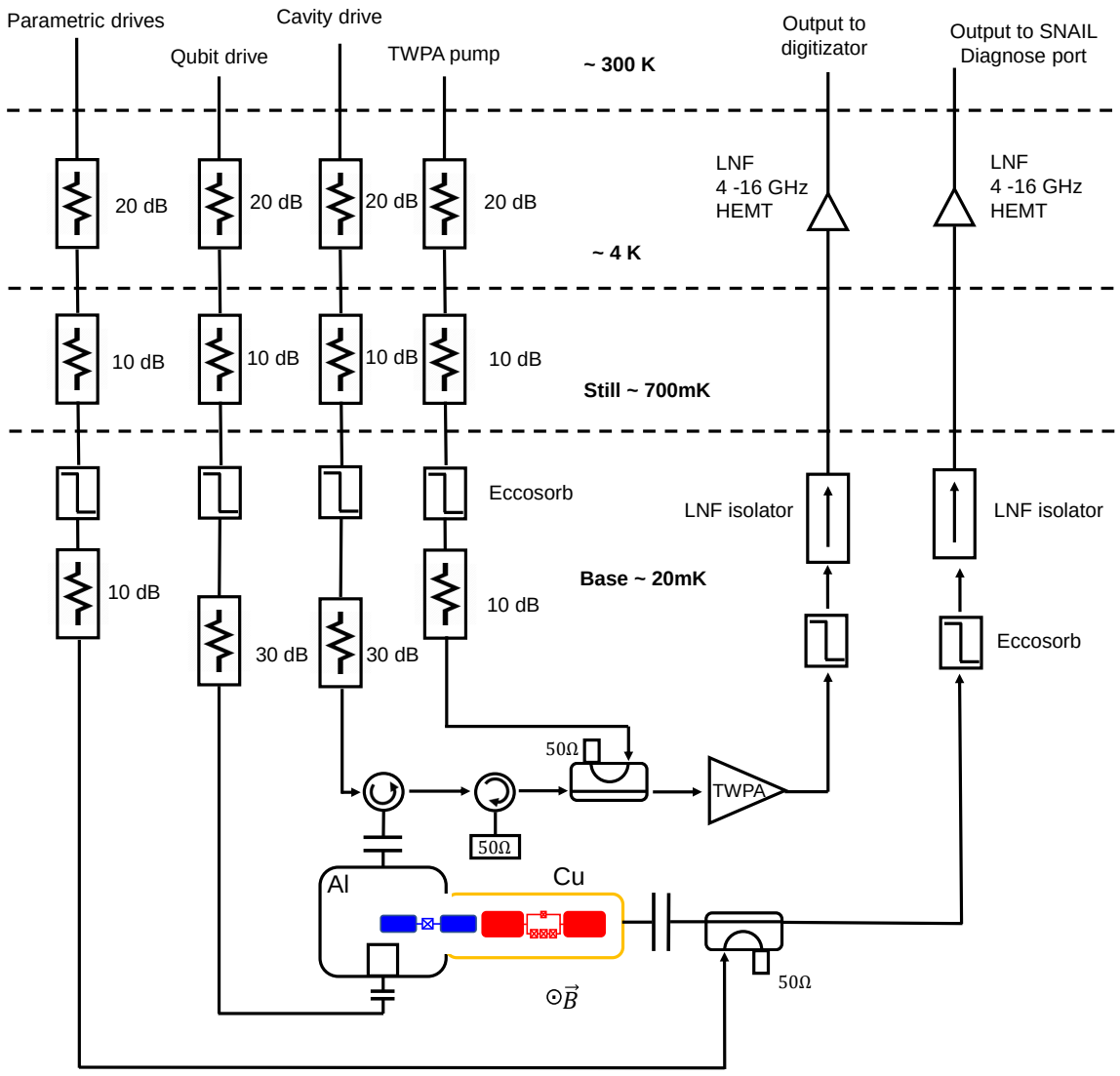

Figure 56: **Wiring diagram of the cryogenic microwave measurement setup for chemical potential experiment.** The experiment is cooled down to around 20 mK on the base of a dilution refrigerator. Input lines carrying signals to the system were attenuated and filtered using homemade lossy Eccosorb filters. The SNAIL flux control is realized with DC signals sent through a separate DC superconducting loom provided by Oxford (not shown) to the magnet, which is bolted to the sample. Output lines carrying signals from the system are also filtered with homemade lossy Eccosorb filter to prevent high frequency stray photons. The isolators on the output lines are used to prevent reflected signals from the HEMT amplifiers/upper stages from propagating backwards into our sample.

information can be accessed from the parametric drives port. An external magnetic flux Φ_{ext} is applied to the SNAIL by a magnet coil close to the sample.

4. Experiment results

Flux bias of the SNAIL mode

In Fig. 57(a) we show the resonant frequency f_s of the SNAIL mode as a function of Φ_{ext}, determined through reflection measurements off of this port. We also sweep the Φ_{ext} in the opposite direction and get the same mode frequencies, indicating that there is no hysteresis in our device.

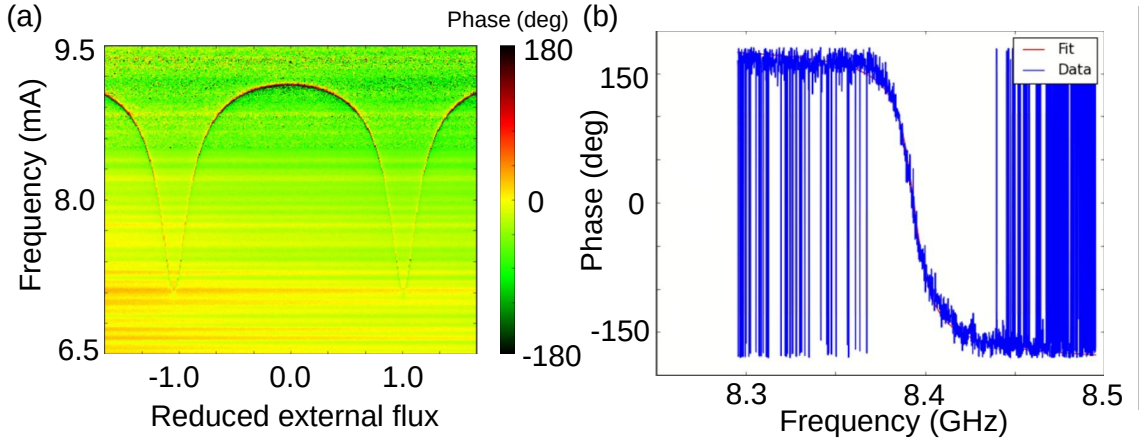

Figure 57: **Flux sweep data of the SNAIL mode.** (a) Reflected phase as a function of frequency for SNAIL mode at different external flux points. The flux is applied through a superconducting coil mounted near the SNAIL. (b) The phase data (blue) measured at $\Phi_{ext} = 0.62\pi$, where the device is operated during the experiment. The data is fitted to a reflection model (red) to obtained the bandwidth for the SNAIL mode.

In Fig. 57(b) we show the reflection data at the bias point $\Phi_{ext} = 0.62\pi$ we operated at during the experiment. The bandwidth of the this mode can be extracted by fitting this data to a reflection model.

At the operational point, by applying the parametric drives to the device at a frequency of $\omega_d = \omega_s + \omega_{ge}$ or $\omega_d = \omega_s - \omega_{ge}$, we can trigger the 'heating' and 'cooling' process

respectively. In practice, however, we need to find the optimal point by sweeping around this ideal frequency, as the pump photons will cause the mode frequency to shift due the Kerr effect, as shown and discussed later in Fig. 62. The qubit state is measured using the conventional dispersive readout method with a TWPA as our nearly quantum-limited amplifier. The TWPA is driven by its own pump tone to achieve a 15 dB gain near the frequency of the readout cavity.

Pulse sequences and measurement protocol

The pulse sequence for studying the qubit's response to bath engineering is shown in Fig. 59. The qubit is first projected to the $|g\rangle$ state by a strong measurement and post-selection, and then rotated to state $|g\rangle$, $|e\rangle$ and $|f\rangle$ as required by the experiment with appropriate *pi* pulses. Next, we apply parametric drives through the SNAIL port with different frequencies to trigger different processes in the system and affect the qubit's relaxation. The length of this stage is a variable, which corresponds to the 'time' parameters in the later sections. In the last stage of the experiment, a strong measurement is performed to readout the state of the qubit in the z basis.

When deciding the state of the qubit from a measurement, there are two regimes of measurement. The first case is when the system is connected with the TWPA as we planned, then we are able to perform a single shot measurement on each readout pulse. A typical result is shown in Fig. 58. where we repeat the same measurement for multiple times and plot all the result as a histogram on the I-Q plane (note that the TWPA is acting as a phase preserving amplifier in these experiments) as shown in Fig. 58. The color of each pixel represents how many times the corresponding I-Q pair has shown up in all these measurements. In this case, the qubit is prepared in the state $(|g\rangle + |e\rangle)/\sqrt{2}$, and we can see two bright blobs in the histogram which correspond to the $|g\rangle$ and $|e\rangle$ states. We also see a third, dimmer, blob which corresponds to the $|f\rangle$ and other higher states that shows up due the finite temperature of the system. Then, in principle, we could prepare the qubit in $|g\rangle$, $|e\rangle$ and $|f\rangle$ state and measure it to get the information of the center of each distribution, and could assign any measurement result we get later to a certain qubit state that it is closest to. The limitation of the fidelity of this method is that the $|f\rangle$ state population is not accurate,

as it is actually the population of all the higher energy state. And there will also be the infidelity that comes from the finite SNR of the measurement, that is there is a non-trivial chances we will identify a $|g\rangle$ state qubit as an $|e\rangle$ state one and vice versa.

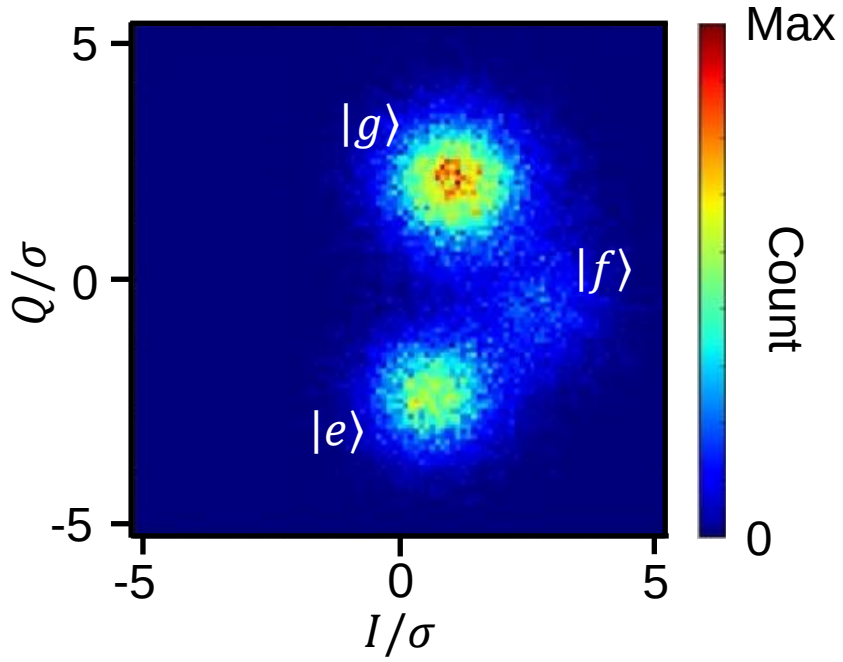

Figure 58: **Histogram of a qubit meausrement with TWPA.** Multiple shots of the measurement is taken and the data are plotted in the form of a 2D histogram. As we discussed in Ch. II, the coherent light can be visulized as a 2D Gaussian distribution on the I-Q plane. For different qubit state, the light will pick up a different phase shift, due the dispersive coupling between the qubit and the readout cavity, result in a different position on the I-Q plane. Note that the $|f\rangle$ state actually represents all the higher state that we cannot distinguish due the the choice of the probe frequency.

The second situation is for the cases when we do not have a TWPA connected with the system, which is not ideal, yet a practical situation we need to deal with as we often mounted more than one sample and had only one TWPA. Without the parametric amplifier, we can no longer perform the single shot measurement to identify where the $|g\rangle$, $|e\rangle$ and $|f\rangle$ states are using the histogram. In this case, we design a series of calibration pulses before each experiment to get the corrected reflected voltage value for different qubit states. There are

six different calibration pulses:

- 1. No pulse, then measure.
- 2. A ge pi pulse, then measure.
- 3. A ge pi pulse, an ef pi pulse, then measure.
- 4. A ge pi pulse, an ef pi pulse, a ge pi pulse, then measure.
- 5. An ef pi pulse, then measure.
- 6. An ef pi pulse, a ge pi pulse, then measure.

Let $V_{g,e,f}$ and $P_{g,e,f}$ be the reflected voltage and population at equilibrium temperature for qubit in $|g\rangle$, $|e\rangle$ and $|f\rangle$ state, V_i be the measured voltage for ith measurement, and assume $|f\rangle$ state population is small at equilibrium, so we have $P_f \sim 0$ and thus $P_g + P_e = 1$. We have:

$$\begin{aligned} V_1 &= P_g V_g + P_e V_e \\ V_2 &= P_g V_e + P_e V_g \\ V_3 &= P_g V_f + P_e V_g \\ V_4 &= P_g V_f + P_e V_e \\ V_5 &= P_e V_f + P_g V_g \\ V_6 &= P_e V_f + P_g V_e. \end{aligned} \tag{VI.4}$$

Recombining these equations, we note that:

$$\frac{V_6 - V_5}{V_4 - V_3} = \frac{P_g}{P_e} \tag{VI.5}$$

then with $P_g + P_e = 1$, we are able to solve P_g and P_e from this equation. Once we have P_g and P_e and substitute them into the equation of V_1, V_2 and V_3, we are able to solve $V_{g,e,f}$, which will then be the calibrated voltage value for the experiment.

This method, however, requires that we do not have too much $|f\rangle$ state at first and that the life time of qubit is long so that decaying to another state during the measurement is unlikely. Unfortunately, this may not always be the case. More, we do not base this measurement on single shots but on ensemble averages, so that population drift, readout drift, and noise can combine to sometimes give nonphysical data (like a negative population) as shown in some of our data.

Fitting relaxation rates

Assuming that the transmon decays via single-photon loss processes, as is usual for a harmonic oscillator, we consider a semi-classical model that describes the evolution of the qubit's polarization using the Bloch equations, with times τ_{ij} or rates Γ_{ij} representing transitions from state i to state j . We define $P_g(t)$, $P_e(t)$ and $P_f(t)$ to be the population of $|g\rangle$, $|e\rangle$ and $|f\rangle$ state, respectively, so that:

$$\begin{aligned}
\frac{dP_g(t)}{dt} &= -P_g(t)(\frac{1}{\tau_{ge}}) + P_e(t)(\frac{1}{\tau_{eg}}) \\
\frac{dP_e(t)}{dt} &= P_g(t)(\frac{1}{\tau_{ge}}) - P_e(t)(\frac{1}{\tau_{eg}}) + P_f(t)(\frac{1}{\tau_{fe}}) \\
\frac{dP_f(t)}{dt} &= -P_f(t)(\frac{1}{\tau_{fe}}) + P_e(t)(\frac{1}{\tau_{ef}})
\end{aligned} \tag{VI.6}$$

Simply put, for each state the rate of the population change is determined by the summation of the rate for the qubit leaving the current state and the rate for the other states qubit coming to this state. This group of differential equations can be solved numerically given the initial state of the system $P_g(0)$, $P_e(0)$ and $P_f(0)$. In practice, we determine the rates of each process γ_{ij} is by comparing the data to the numeric result of the above equations while manually adjusting the rates until it matches with the data, as we have found that automatic fitting can be quite unstable for this system. This is how we get the 'fit' curves and relaxation rates in the figures shown below. We should also note here that the rates can vary by a factor of 100 from slowest to fastest, in which case the slowest rates (corresponding to the longest coherence times) can only be determined rather inaccurately from our data.

To get the steady state distribution in the two-level system form by $|g\rangle$ and $|e\rangle$ and estimate a qubit temperature, we assume the $|f\rangle$ population is negligible and set $dP_g(t)/dt = dP_e(t)/dt = 0$ to find the usual relationship:

$$\frac{P_g(\infty)}{P_e(\infty)} = \frac{\tau_{ge}}{\tau_{eg}}. \tag{VI.7}$$

Single pump result

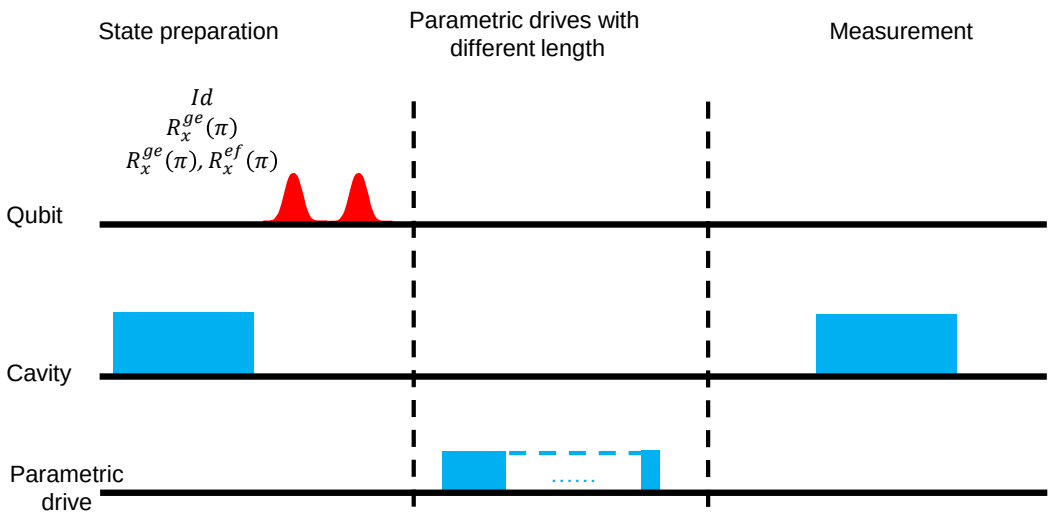

Figure 59: **Pulse sequence for chemical potential experiment.** This pulse sequence consists three stages of qubit, cavity and parametric drive manipulation. The first stage is state preparation, during which the qubit is first projected to the state $|g\rangle$ by a strong measurement (blue box) and post-selection, and then rotated to the state ($|g\rangle$, $|e\rangle$ *or* $|f\rangle$) as required by the protocol with no pulse (Identity), $R_x^{ge}(\pi)$ or a $R_x^{ge}(\pi)$ pulse followed by a $R_x^{ef}(\pi)$ pulse, respectively. The second stage is of qubit relaxation, during which the system is parametrically driven (or not) by the signals through the 'SNAIL' port with different frequencies. We vary the length of this stage which corresponds to the 'time' parameters in the following measurements. In the third and final stage a strong measurement is performed to readout the state of the qubit.

We first show the result of the heating '$\Sigma_{ge,s}$' drive. In Fig. 60, we plot the population of the lowest three levels of the transmon as a function of time for different $\Sigma_{ge,s}$ drive strengths. Figure 60(a) shows a particular case where we set the drive strength so that the 'heating' rate matches the nature decay rate of the qubit. If the bath engineering process is working as desired, the un-driven rates (for the example of $\Sigma_{ge,s}$ driving this would be all rates except Γ_{ge} (and time τ_{ge}) while remain unchanged. If the two rates are close to each other, we will end up with a steady state with a similar population of ground and excited state, as we have

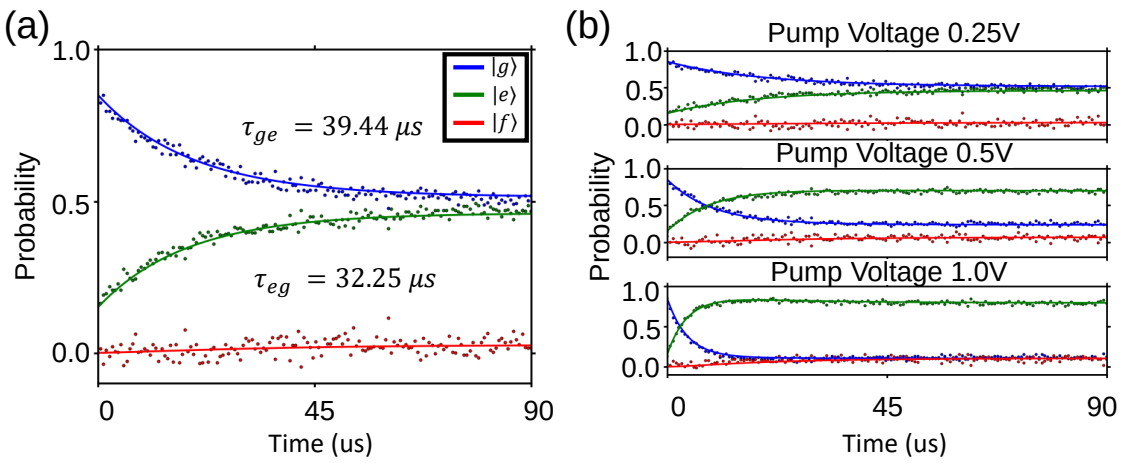

Figure 60: **Experiment result for '$\Sigma_{ge,s}$ drive'.** Qubit population number for different energy level as a function of time with different pump conditions. The qubit is prepared in ground state. (a) As we turn on the drive, the $|e\rangle$ state population is gradually increased, indicating a 'heating' process for the qubit. We adjust the driving strength so that the qubit 'heating' rate is close to its natural decay rate, which result in a steady state with population distribution close to 50/50 between $|g\rangle$ and $|e\rangle$ state. (b) Result for the same drive with different strength. As the driving strength becomes stronger, the qubit thermalizes to its equilibrium faster and also the excited state population is larger, indicating a 'hotter' qubit. And as we keep increasing the drive strength, we reach a population inversion state for the qubit, which is non-achievable by thermalizing it to a natural heat bath. The experimental data is consistent with the simulation result in the previous chapter.

seen in Fig. 60(a), and the effective temperature (if we pretend that the transmon has no higher states, an assumption that is well supported by the very low population of the $|f\rangle$ state) is very nearly infinite. In Fig. 60(b) we show the result of the same protocol with different pumping strengths. It is clear that as this strength gets stronger, the system reaches the steady state faster with final population distribution that is consistent with Eq. VI.7. We are also getting more $|f\rangle$ population as the we drive the system harder. This is due to the finite anharmonicity of the qubit and also the increased population of $|e\rangle$ state, as we

expected from our numerical result in Fig. 36.

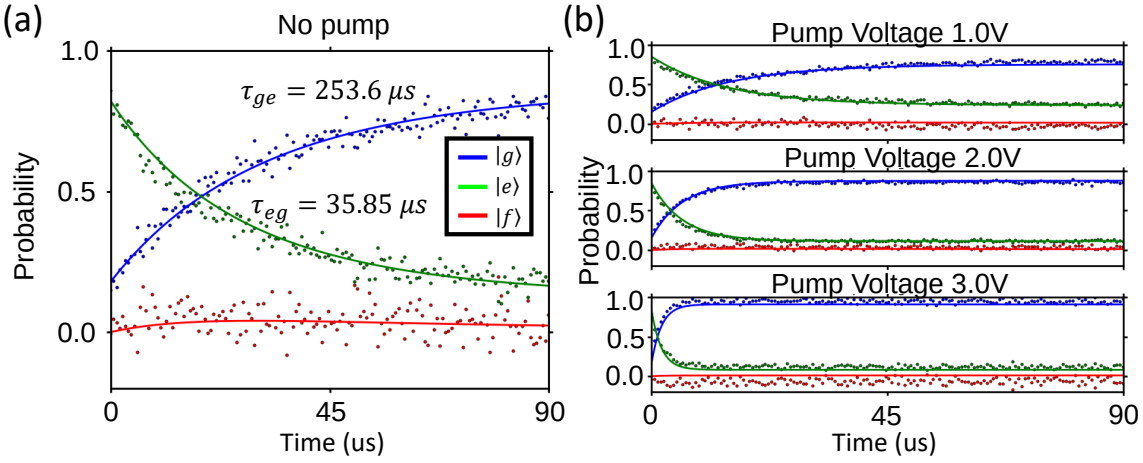

Figure 61: **Experiment result for '$\delta_{ge,s}$ drive'.** Qubit population number for different energy level as a function of time with different pump conditions. The qubit is prepared in excited state. (a) The natural energy relaxation process for the qubit. Note that due to the finite physical temperature of the system, there is a non-trivial population of $|e\rangle$ state at equilibrium. (b) Result for the '$\delta_{ge,s}$' drive with different strength. As the driving strength becomes stronger, the qubit thermalizes to its equilibrium faster and also the $|g\rangle$ state population is larger, indicating a 'cooler' qubit. The experimental data is consistent with the simulation result in the previous chapter.

We get a similar result for the '$\delta_{ge,s}$ drive'. In Fig. 61, we plot the population number of each state as a function of time for different pump strength. Figure. 61(a) shows the case where we apply no drive to the system so we are seeing nature decay of the qubit with the rate τ_{eg}. We note that due to the finite temperature, the system does not reset completely in the ground state, but with a non-zero population in the excited state. In Fig. 61(b) we show the result of the same measurement with different pumping strengths. As we expected, the system goes to a 'cooler' state with a faster rate when the pump strength gets stronger.

Kerr effect in the system

The result of '$\Sigma_{ge,s}$' and '$\delta_{ge,s}$' drive shows that with a single parametric drive, one can control the rate the system reaches to the equilibrium but the population distribution in the

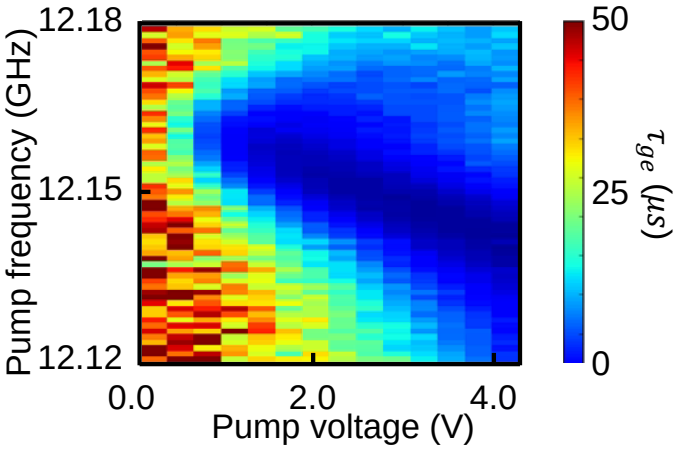

Figure 62: **Data for the Kerr effect with $\Sigma_{ge,s}$ drive.** The qubit upgoing time τ_{ge} as a function of different $\Sigma_{ge,s}$ pump conditions. The qubit is prepared in ground state and we apply a $\Sigma_{ge,s}$ pump to the system. We sweep the frequency and strength of the pump and record the states population as a function of time. The qubit $|g\rangle$ to $|e\rangle$ transition rate is calculated from Eq. VI.6.

steady state cannot be set independently. In order to control both the rate and steady state distribution we need to apply both drives at the same time. However, this requires us to consider the Kerr effect as there will be more pump photons that shifts the mode frequency. We can see the Kerr effect by sweeping the pump conditions and frequencies. The result is shown in Fig. 62. The qubit is prepared in $|g\rangle$ state. We then turn on the $\Sigma_{ge,s}$ pump with different drive frequencies and strengths. The qubit will then start to 'heat up' towards the $|e\rangle$ state, with a rate $1/\tau_{ge}$ that can be extracted from Eq. VI.6. As we increase the drive strength, the Kerr effect will start to shift the mode frequency negatively, result in a change of the optimal pump frequency. This effect can be seen in Fig. 62 as the optimal pump conditions for the fastest transition time is moving negatively in frequency as pump strength increases. Because the with a negative Kerr term and non-zero pump photons in the corresponding mode, we effectively create a negative frequency shift for the mode.

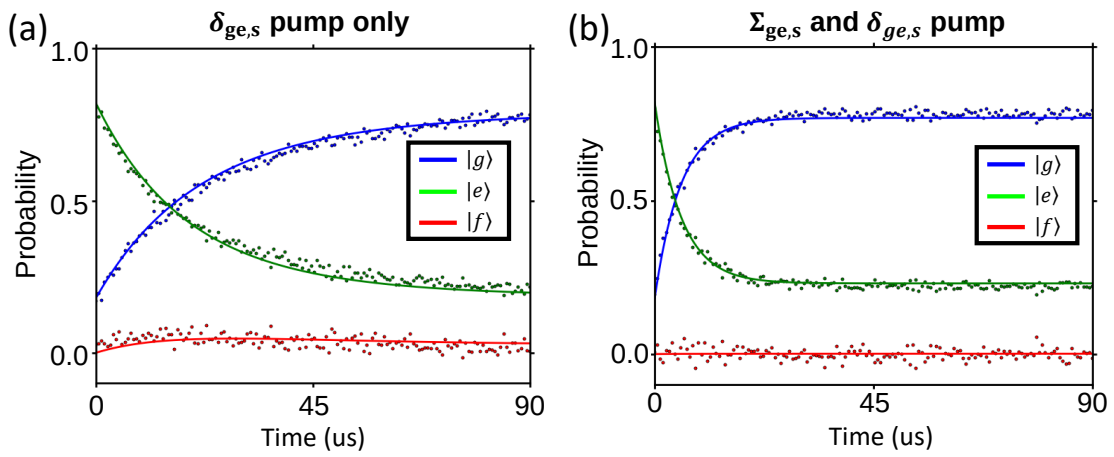

Figure 63: **Experiment result for single and multi-drives.** Qubit population number for different energy level as a function of time with different pump conditions. The qubit is prepared in excited state. (a) We apply a single $\delta_{ge,s}$ drive to the system with a strength of 0.1 MHz. The qubit starts 'cooling' as we turn on the drive. (b) We apply a '$\Sigma_{ge,s}$' pump and a '$\delta_{ge,s}$' pump at the same time. Now the system still thermalized to the state with the same population distribution, but at a much faster rate.

Multi-pump result

In order to operate the system with multiple pumps at the same time, we need to correct our pump pulses by considering this Kerr effect. In Fig. 63(b), we show the result for the case where we apply both $\Sigma_{ge,s}$ and $\delta ge, s$ drives at the same time with corrected pump parameters and compare it to a case where we only apply a single $\delta_{ge,s}$ pulse. For both pumping schemes, the qubit thermalizes to a steady state with the same population distribution, corresponding to the same chemical potential. It is also clear to see that with both pumps on, the system reaches the equilibrium faster than the single pump case showing that by carefully choosing the strengths of the 'heating' and 'cooling' processes. This faster thermalization rate is crucial if we want to use this qubit as 'bath' that will eventually couples to another system. However, we also need to note here that in order to operate the system with multi-pump on at the same time, we need to take into account the Kerr effects from all the pump drives.

That is, we need to carefully search for the optimal pump frequencies for all the pumps so that we can compensate the frequency shifts induced by the pump photons.

D. Conclusion and outlook

In this chapter, we introduced the experimental realization for the proposal that creates chemical potential for a transmon qubit.

The direct implementation of the original proposal with a low frequency JPC had a promising start but did not succeed in the end, as the low participation ratio of the low frequency idler mode limited the rate of the parametric processes and the large internal loss of the device further reduced the signal photon life time. Because of this, the transmon's photon will decay faster than the thermalization rate to our engineered bath. We next moved to the idea of coupling a transmon qubit to a lossy SNAIL. In this case, we no longer have a participation ratio problem, so the parametric process can be driven at a decent rate. And the life time of qubit is largely increased by placing the it in a high Q 3D cavity. So with this new design, we overcome the difficulties we encounter with the low frequency JPC, and are able to realize a controllable chemical potential for the photons in the qubit.

A chemical potential for light will allow the quantum systems to access a wide variety domains that are used to be forbidden. In addition to the application of the controllable bath itself, the setup we used in the experiment is also showing its potential of being a promising platform for new experiments.

VII. Conclusion

We have discussed two major experiments in this thesis: qubit measurement with two-mode squeezed light and a tunable chemical potential for photonic (qubit) system. Although very different in their aim and effect, they are both examples of what can be achieved with parametric driving. As stated in Ch. II, the term 'parametric' can be a bit confusing in superconducting quantum information, and so we have adopted in practice a definition which captures the essence of what we try to achieve with parametric drives, which we will try to define here. Our circuits are typically controlled entirely by microwave drive tones applied externally, and the terms we are interested in are often associated with the couplings among multiple modes, and it is hard to imagine our drives as physically dragging elements around as in simple physical examples. Instead, we adopt the following as a definition for parametric processes and drives. The simplest parametric process is one where a non-rotating term comprised of N raising and/or lower operators in the Hamiltonian is driven so as to produce an order $N-1$, rotating term. This definition is a bit broad, but we find it operationally useful in the lab as an engineering tool, because it teaches you how to produce evolution you desire from the 'hidden' non-rotating terms in the system, or alternately gives you guidance on which nonlinearities might be useful to build into a system for later use as controls.

If one wants to be even more general, we can extend this further to parametric processes which consume multiple pump photons/waves simultaneously. This would, for instance, be a process where two pumps are used simultaneously to take a 4th order term and produce a 2nd order interaction, as in the double-pumped JPA [87]. Then we could define an M-wave parametric process as using an Nth order non-RWA term and M pump photons (which can be produced from 1 to M drive tones) to produce an $(N-M)$th order rotating term. This perhaps begins to feel a little bit excessive, and it is certainly true that we are not eager to climb the ladder to higher values of M. However, this type of thinking is probably more important than we realize, as we are finding in our experiments across the laboratory, that things like amplifier saturation [81, 82, 89] are related to unintentionally activated, higher-order, parametric processes, and we suspect this may also play a role in qubit-qubit controls

and perhaps also the QNDness of qubit readout in circuit QED. Relevant examples of experiments which may be experiencing similar effects (though with different ways of viewing and explaining these issues) can be found in references [132, 133].

So, in short, we define a parametric drive as one which utilizes a drive applied to term which in the undriven system has negligible impact (or as is often states, is eliminated by the rotating wave approximation) to create a lower order rotating term. This new term need not respect energy or excitation conservation (the drive provides as source/sink of photons as required). Thus, parametric drives can be quite useful and flexible tools for manipulating quantum system. Much of the 'Hamiltonian engineering' which our laboratory is now pursuing is focused on making use of these drives in all aspects of quantum information. One final caveat: the ubiquitous fourth-order Kerr terms in circuit QED have both non-rotating and rotating terms, the former are regularly used to power parametric processes. This doesn't conflict with our definition above, but the tendency of Kerr-based nonlinearities to shift with drive frequency certainly adds additional complications we would prefer to avoid.

In the first project presented in this thesis, parametric drives are used to generate and manipulate two-mode squeezed light. One important result from this project is that we have demonstrated a new scheme for interferometric readout of a superconducting qubit with displaced two-mode squeezed vacuum and show a 44% improvement in power SNR compared to conventional coherent light plus phase-preserving amplification readout.

Another, more interesting, result appeared as we investigated the quantum readout efficiency of our TMS interferometer using weak measurement protocol. The data show that there are important effects on the ratio between z back-action and the concomitant qubit phase back-action of this measurement process relative to other known readout schemes. It appears that the increase in SNR of TMS readout which we demonstrated for projective readout comes at the cost of reducing the trackability of phase back-action in the presence of noise/inefficiency in the system. Conversely, if we perform the measurement at a point where the interferometer has the *lowest* achievable SNR, we instead see enhaced phase back-action trackability.

We believe that these weak measurement results help explain how the TMS interferometer exceeds the usual limits for SNR in qubit measurements with coherent state readout, namely

by deliberately paying a price in a quantity (the phase back-action). This effect seems to resemble a related tradeoff in phase-sensitive readout [87], in which a choice of amplifier phase can give perfect knowledge of one quadrature of a qubit's evolution by squeezing the other away, and we attribute the effect in TMS readout to the more complicated TMS squeezing process of the entangler and analyzer JPCs.

In the second project, parametric drives are used to create couplings between a qubit and the lossy bath mode, which allows us to control the drives and dissipation between the qubit and bath to perform desired bath engineering process. The important result from this project is that we have created a photonic system (trasmon qubit) with a chemical potential that can be tuned by the parametric drives we apply to the system. We started with a low-frequency JPC plan that was proposed in the origin proposal. Although it was not the final design for the experiment due to some technical problems, we still learned how to build a JPC with a such low frequency in both microstrip and lumped version. The experience we gained may find use in future work when such a JPC is needed for other applications.

The final design involves a transmon qubit couples to a lossy SNAIL mode, which provides a third order coupling between the system (qubit) and the bath (SNAIL). With the help of this coupling we can address the 'heating' and 'cooling' process for the system separately (which are controlled by a single pump in the original proposal), thus gives us more control of the system which lifts the requirement of the low frequency mode. By tuning the strengths of the drives, we can control the rate of each process to achieve a system with both a controllable chemical potential and independently tunable relaxation timescale. Our tunable chemical potential for light will allow quantum systems to access a wide variety of domains that are not achievable with present control schemes [67–69]. Further work in this direction is ongoing in the lab in collaboration with Houck's group at Princeton.

Outlook

In the TMS readout experiment, although we lack a full theory for our device in the presence of finite efficiency and amplifier bandwidth, we believe that we can find practical applications of this effect by adding a second qubit to the other arm of the interferometer and attempting to entangle the two qubits by measurement. A similar entanglement

generation protocol has been proposed in [115, 134], in which a single phase-preserving amplifier is used to entangle the photons from two different qubit-cavity systems. Then by performing a pseudo-parity measurement and post-selecting the result, we are able to create a measurement-based remote entanglement between the qubits. The implementation of this protocol requires a good projective measurement in the z direction to select out the desired parity result with high fidelity while keep a minimal measurement back-action and maintain a high measuremetn efficiency on the qubits so that we are indeed generating a entangled state instead of a mixed state. Now with our new discovery of relation between the z-projectiveness and phase trackability, we can make a trade-off that rebalance the measurement strength and the back-action *in-situ* to find the optimal operation point that gives the necessary improvement to overcome the losses and inefficiencies which currently limit these experiments.

In the bath engineering project, we introduce a new design that combines transmons and 3D cavities with 'SNAIL in tube' in our setup not only benefits us in this experiment, but also shows a large potential for other applications. The Schoelkopf and Devoret groups at Yale [130] have pioneered this architecture for fourth order couplings, here we adapt it admit flux for a SNAIL and its third order non-linearity. Our early results find that the third-order parametric couplings seem to have a natural advantage over fourth order couplings in that their pump frequencies are unambiguous, which has the disadvantage of giving the experimenter no wiggle room if two processes are nearby in frequency. However on the other hand, it brings a larger advantage that unwanted transitions are much easier to avoid (as they are, again, fixed in frequency). This will need further exploration, and applying multiple pumps to activate multiple parametric processes does create some difficulties. Primarily this is due to Kerr effects as shown above, which we believe are both due to static and dynamical effects as we have explored thoroughly in parametric amplifiers [82, 89, 120], but also the accidental activation of a fourth or higher order process with the combination of the multiple drives.

However, there are some existing issues that needs to be solved before we can better use the design for other projects. One major challenge is the loss of the seam where copper and aluminum (or aluminum and aluminum) connect [135]. Since the electromagnetic field

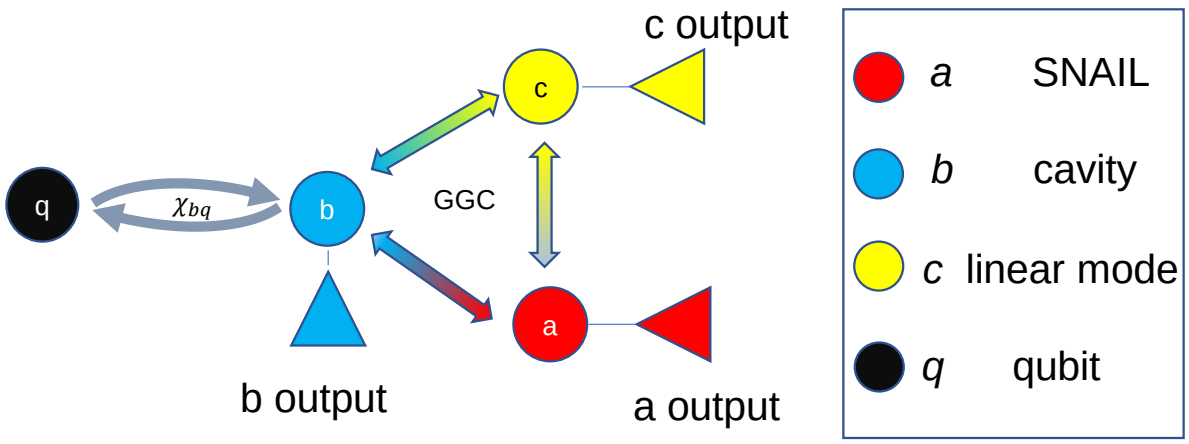

Figure 64: **Schematic of embedded amplifier.** Embedded amplifier design based on the platform inspired by the chemical potential project. We will have the transmon, cavity and SNAIL coupled the same way as in the chemical potential project and add another linear resonator and have it also coupled to the SNAIL mode. Then by driving a Gain-Gain-Conversion process between the SNAIL, resonator and cavity while still having the transmon dispersively coupled to the cavity, we can create a parametric amplification process that is sensitive to the state of the transmon.

can touch the seam, there will be currents flow through across it. Then, the loss of the seams will result in a lower internal Q for the corresponding mode. In our experiment we are primarily concerned about this lowering the lifetime of the transmon, unfortunately it is also the mode closest to the seam. This effect can be minimized by carefully design the the geometry of future samples, especially the placement of the copper-aluminum transition and avoiding any aluminum-aluminum joints with significant participation in high Q cavity modes. Also, this new design requires a longer chip with with multiple objects (resonators, SNAILs, transmons) on a single piece of sapphire, which needs extra writing time and no failure in any element, and therefore brings extra difficulties during the fabrication process. We are addressing this by adopting the Houck group's new tantalum fabrication method qubit [32], writing all large features optically without (hopefully) sacrificing coherence time

and leaving only junction failure as a significant issue which we can address with larger number of samples due to the vastly reduced ($\sim$ 5-10 hours to $\sim$ half an hour) of a set of $\sim$ 20 SNAILs and transmons.

We already have some plans of how to use the setup for other experiments. One interesting idea is the 'embedded amplifier'. As shown in the schematic in Fig. 64 we are trying to integrate a parametric amplifier directly with a qubit-cavity system. Then, we can perform a qubit measurement without using a lossy directional device like a circulator or isolator which can, in principle, increase the measurement efficiency. We have seen preliminary results where we apply a pump to the SNAIL mode in our existing sample and observed a 20 dB gain in that mode. This demonstrates that this device can operate in amplification mode, and thus gives us more confidence that the embedded amplifier can be realized in the same device.

Bibliography

[1] Richard P Feynman. Simulating physics with computers. *Int. J. Theor. Phys*, 21(6/7), 1982.

[2] David Deutsch. Quantum theory, the church–turing principle and the universal quantum computer. *Proceedings of the Royal Society of London. A. Mathematical and Physical Sciences*, 400(1818):97–117, 1985.

[3] Lov K Grover. A fast quantum mechanical algorithm for database search. In *Proceedings of the twenty-eighth annual ACM symposium on Theory of computing*, pages 212–219, 1996.

[4] Peter W Shor. Polynomial-time algorithms for prime factorization and discrete logarithms on a quantum computer. *SIAM review*, 41(2):303–332, 1999.

[5] David G Cory, Mark D Price, and Timothy F Havel. Nuclear magnetic resonance spectroscopy: An experimentally accessible paradigm for quantum computing. *Physica D: Nonlinear Phenomena*, 120(1-2):82–101, 1998.

[6] Boris B Blinov, Dietrich Leibfried, C Monroe, and David J Wineland. Quantum computing with trapped ion hyperfine qubits. *Quantum Information Processing*, 3(1-5):45–59, 2004.

[7] Jean-Michel Raimond, M Brune, and Serge Haroche. Manipulating quantum entanglement with atoms and photons in a cavity. *Reviews of Modern Physics*, 73(3):565, 2001.

[8] Yu Nakamura, Yu A Pashkin, and Jaw Shen Tsai. Coherent control of macroscopic quantum states in a single-cooper-pair box. *Nature*, 398(6730):786–788, 1999.

[9] Frank Arute, Kunal Arya, Ryan Babbush, Dave Bacon, Joseph C Bardin, Rami Barends, Rupak Biswas, Sergio Boixo, Fernando GSL Brandao, David A Buell, et al. Quantum supremacy using a programmable superconducting processor. *Nature*, 574(7779):505–510, 2019.

[10] Bruce E Kane. A silicon-based nuclear spin quantum computer. *Nature*, 393(6681):133–137, 1998.

[11] Charles D Hill, Eldad Peretz, Samuel J Hile, Matthew G House, Martin Fuechsle, Sven Rogge, Michelle Y Simmons, and Lloyd CL Hollenberg. A surface code quantum computer in silicon. *Science Advances*, 1(9):e1500707, 2015.

[12] J Randall, S Weidt, ED Standing, K Lake, SC Webster, DF Murgia, T Navickas, K Roth, and WK Hensinger. Efficient preparation and detection of microwave dressed-state qubits and qutrits with trapped ions. *Physical Review A*, 91(1):012322, 2015.

[13] CJ Ballance, TP Harty, NM Linke, MA Sepiol, and DM Lucas. High-fidelity quantum logic gates using trapped-ion hyperfine qubits. *Physical Review Letters*, 117(6):060504, 2016.

[14] Shantanu Debnath, Norbert M Linke, Caroline Figgatt, Kevin A Landsman, Kevin Wright, and Christopher Monroe. Demonstration of a small programmable quantum computer with atomic qubits. *Nature*, 536(7614):63–66, 2016.

[15] Xi-Lin Wang, Luo-Kan Chen, Wei Li, H-L Huang, Chang Liu, Chao Chen, Y-H Luo, Z-E Su, Dian Wu, Z-D Li, et al. Experimental ten-photon entanglement. *Physical Review Letters*, 117(21):210502, 2016.

[16] Xiaogang Qiang, Xiaoqi Zhou, Jianwei Wang, Callum M Wilkes, Thomas Loke, Sean O'Gara, Laurent Kling, Graham D Marshall, Raffaele Santagati, Timothy C Ralph, et al. Large-scale silicon quantum photonics implementing arbitrary two-qubit processing. *Nature Photonics*, 12(9):534–539, 2018.

[17] Jerry M Chow, Jay M Gambetta, Antonio D Corcoles, Seth T Merkel, John A Smolin, Chad Rigetti, S Poletto, George A Keefe, Mary B Rothwell, John R Rozen, et al. Universal quantum gate set approaching fault-tolerant thresholds with superconducting qubits. *Physical Review Letters*, 109(6):060501, 2012.

[18] Michel H Devoret and Robert J Schoelkopf. Superconducting circuits for quantum information: an outlook. *Science*, 339(6124):1169–1174, 2013.

[19] John Preskill. Quantum computing in the nisq era and beyond. *Quantum*, 2:79, 2018.

[20] Matthias Steffen, David P DiVincenzo, Jerry M Chow, Thomas N Theis, and Mark B Ketchen. Quantum computing: An ibm perspective. *IBM Journal of Research and Development*, 55(5):13–1, 2011.

[21] Mary A Rowe, David Kielpinski, Volker Meyer, Charles A Sackett, Wayne M Itano, Christopher Monroe, and David J Wineland. Experimental violation of a bell's inequality with efficient detection. *Nature*, 409(6822):791–794, 2001.

[22] Jens Koch, M Yu Terri, Jay Gambetta, Andrew A Houck, DI Schuster, J Majer, Alexandre Blais, Michel H Devoret, Steven M Girvin, and Robert J Schoelkopf. Charge-insensitive qubit design derived from the cooper pair box. *Physical Review A*, 76(4):042319, 2007.

[23] Antonio D Córcoles, Easwar Magesan, Srikanth J Srinivasan, Andrew W Cross, Matthias Steffen, Jay M Gambetta, and Jerry M Chow. Demonstration of a quantum error detection code using a square lattice of four superconducting qubits. *Nature Communications*, 6(1):1–10, 2015.

[24] Rami Barends, Julian Kelly, Anthony Megrant, Andrzej Veitia, Daniel Sank, Evan Jeffrey, Ted C White, Josh Mutus, Austin G Fowler, Brooks Campbell, et al. Superconducting quantum circuits at the surface code threshold for fault tolerance. *Nature*, 508(7497):500–503, 2014.

[25] John M Martinis, S Nam, J Aumentado, and C Urbina. Rabi oscillations in a large josephson-junction qubit. *Physical Review Letters*, 89(11):117901, 2002.

[26] Matthias Steffen, M Ansmann, R McDermott, Nadav Katz, Radoslaw C Bialczak, Erik Lucero, Matthew Neeley, Eva M Weig, Andrew N Cleland, and John M Martinis. State tomography of capacitively shunted phase qubits with high fidelity. *Physical Review Letters*, 97(5):050502, 2006.

[27] Jonathan R Friedman, Vijay Patel, Wei Chen, SK Tolpygo, and James E Lukens. Quantum superposition of distinct macroscopic states. *Nature*, 406(6791):43–46, 2000.

[28] Douglas A Bennett, Luigi Longobardi, Vijay Patel, Wei Chen, Dmitri V Averin, and James E Lukens. Decoherence in rf squid qubits. *Quantum Information Processing*, 8(2-3):217–243, 2009.

[29] Vladimir E Manucharyan, Jens Koch, Leonid I Glazman, and Michel H Devoret. Fluxonium: Single cooper-pair circuit free of charge offsets. *Science*, 326(5949):113–116, 2009.

[30] Ioan M Pop, Kurtis Geerlings, Gianluigi Catelani, Robert J Schoelkopf, Leonid I Glazman, and Michel H Devoret. Coherent suppression of electromagnetic dissipation due to superconducting quasiparticles. *Nature*, 508(7496):369–372, 2014.

[31] Peter Groszkowski, A Di Paolo, AL Grimsmo, A Blais, DI Schuster, AA Houck, and Jens Koch. Coherence properties of the 0-π qubit. *New Journal of Physics*, 20(4):043053, 2018.

[32] Alex PM Place, Lila VH Rodgers, Pranav Mundada, Basil M Smitham, Mattias Fitzpatrick, Zhaoqi Leng, Anjali Premkumar, Jacob Bryon, Sara Sussman, Guangming Cheng, et al. New material platform for superconducting transmon qubits with coherence times exceeding 0.3 milliseconds. *arXiv preprint arXiv:2003.00024*, 2020.

[33] Alexandre Blais, Steven M Girvin, and William D Oliver. Quantum information processing and quantum optics with circuit quantum electrodynamics. *Nature Physics*, pages 1–10, 2020.

[34] Felix Motzoi, Jay M Gambetta, Patrick Rebentrost, and Frank K Wilhelm. Simple pulses for elimination of leakage in weakly nonlinear qubits. *Physical Review Letters*, 103(11):110501, 2009.

[35] Simon Gustavsson, Olger Zwier, Jonas Bylander, Fei Yan, Fumiki Yoshihara, Yasunobu Nakamura, Terry P Orlando, and William D Oliver. Improving quantum gate fidelities by using a qubit to measure microwave pulse distortions. *Physical Review Letters*, 110(4):040502, 2013.

[36] Sarah Sheldon, Lev S Bishop, Easwar Magesan, Stefan Filipp, Jerry M Chow, and Jay M Gambetta. Characterizing errors on qubit operations via iterative randomized benchmarking. *Physical Review A*, 93(1):012301, 2016.

[37] Jerry M Chow, AD Córcoles, Jay M Gambetta, Chad Rigetti, BR Johnson, John A Smolin, JR Rozen, George A Keefe, Mary B Rothwell, Mark B Ketchen, et al. Simple all-microwave entangling gate for fixed-frequency superconducting qubits. *Physical Review Letters*, 107(8):080502, 2011.

[38] Atsushi Noguchi, Alto Osada, Shumpei Masuda, Shingo Kono, Kentaro Heya, Samuel Piotr Wolski, Hiroki Takahashi, Takanori Sugiyama, Dany Lachance-Quirion, and Yasunobu Nakamura. Fast parametric two-gubit gates with suppressed residual interaction using a parity-violated superconducting qubit. *arXiv preprint arXiv:2005.02630*, 2020.

[39] David P. DiVincenzo. Fault-tolerant architectures for superconducting qubits. *Physica Scripta T*, T137, 2009.

[40] Peter Brooks, Alexei Kitaev, and John Preskill. Protected gates for superconducting qubits. *Physical Review A*, 87(5):052306, 2013.

[41] K Serniak, M Hays, G de Lange, S Diamond, S Shankar, LD Burkhart, L Frunzio, M Houzet, and MH Devoret. Hot nonequilibrium quasiparticles in transmon qubits. *Physical Review Letters*, 121(15):157701, 2018.

[42] Peter W Shor. Scheme for reducing decoherence in quantum computer memory. *Physical Review A*, 52(4):R2493, 1995.

[43] John Preskill. Reliable quantum computers. *Proceedings of the Royal Society of London. Series A: Mathematical, Physical and Engineering Sciences*, 454(1969):385–410, 1998.

[44] Emanuel Knill, Raymond Laflamme, and Wojciech H Zurek. Resilient quantum computation. *Science*, 279(5349):342–345, 1998.

[45] Daniel Gottesman. Theory of fault-tolerant quantum computation. *Physical Review A*, 57(1):127, 1998.

[46] P Campagne-Ibarcq, A Eickbusch, S Touzard, E Zalys-Geller, NE Frattini, VV Sivak, P Reinhold, S Puri, S Shankar, RJ Schoelkopf, et al. A stabilized logical quantum bit encoded in grid states of a superconducting cavity. *arXiv preprint arXiv:1907.12487*, 2019.

[47] Alexandre Blais, Jay Gambetta, Andreas Wallraff, David I Schuster, Steven M Girvin, Michel H Devoret, and Robert J Schoelkopf. Quantum-information processing with circuit quantum electrodynamics. *Physical Review A*, 75(3):032329, 2007.

[48] Ling Hu, Yuwei Ma, Weizhou Cai, Xianghao Mu, Yuan Xu, Weiting Wang, Yukai Wu, Haiyan Wang, YP Song, C-L Zou, et al. Quantum error correction and universal

gate set operation on a binomial bosonic logical qubit. *Nature Physics*, 15(5):503–508, 2019.

[49] P Oscar Boykin, Tal Mor, Matthew Pulver, Vwani Roychowdhury, and Farrokh Vatan. On universal and fault-tolerant quantum computing: a novel basis and a new constructive proof of universality for shor's basis. In *40th Annual Symposium on Foundations of Computer Science (Cat. No. 99CB37039)*, pages 486–494. IEEE, 1999.

[50] Vladimir B Braginsky, Yuri I Vorontsov, and Kip S Thorne. Quantum nondemolition measurements. *Science*, 209(4456):547–557, 1980.

[51] MD Reed, L DiCarlo, BR Johnson, L Sun, DI Schuster, L Frunzio, and RJ Schoelkopf. High-fidelity readout in circuit quantum electrodynamics using the jaynes-cummings nonlinearity. *Physical Review Letters*, 105(17):173601, 2010.

[52] John R Klauder. The action option and a feynman quantization of spinor fields in terms of ordinary c-numbers. *Annals of Physics*, 11(2):123–168, 1960.

[53] Carlton M Caves. Quantum limits on noise in linear amplifiers. *Physical Review D*, 26(8):1817, 1982.

[54] M Hatridge, S. Shankar, M Mirrahimi, F Schackert, K Geerlings, T Brecht, K M Sliwa, B Abdo, L Frunzio, S M Girvin, R J Schoelkopf, and M H Devoret. Quantum back-action of an individual variable-strength measurement. *Science*, 339(January):178–182, 2013.

[55] JI Cirac, AS Parkins, R Blatt, and P Zoller. "dark"squeezed states of the motion of a trapped ion. *Physical Review Letters*, 70(5):556, 1993.

[56] JF Poyatos, J Ignacio Cirac, and P Zoller. Quantum reservoir engineering with laser cooled trapped ions. *Physical Review Letters*, 77(23):4728, 1996.

[57] Martin B Plenio, SF Huelga, A Beige, and PL Knight. Cavity-loss-induced generation of entangled atoms. *Physical Review A*, 59(3):2468, 1999.

[58] MB Plenio and SF Huelga. Entangled light from white noise. *Physical Review Letters*, 88(19):197901, 2002.

[59] Kurtis Geerlings, Zaki Leghtas, Ioan M Pop, Shyam Shankar, Luigi Frunzio, Robert J Schoelkopf, Mazyar Mirrahimi, and Michel H Devoret. Demonstrating a driven reset protocol for a superconducting qubit. *Physical Review Letters*, 110(12):120501, 2013.

[60] Clement H Wong, Chris Wilen, Robert McDermott, and Maxim G Vavilov. A tunable quantum dissipator for active resonator reset in circuit qed. *Quantum Science and Technology*, 4(2):025001, 2019.

[61] Yao Lu, Srivatsan Chakram, Nelson Leung, Nathan Earnest, Ravi K Naik, Ziwen Huang, Peter Groszkowski, Eliot Kapit, Jens Koch, and David I Schuster. Universal stabilization of a parametrically coupled qubit. *Physical Review Letters*, 119(15):150502, 2017.

[62] S Shankar, M Hatridge, Z Leghtas, KM Sliwa, A Narla, U Vool, SM Girvin, L Frunzio, M Mirrahimi, and MH Devoret. Stabilizing entanglement autonomously between two superconducting qubits. *arXiv preprint arXiv:1307.4349*, 2013.

[63] ME Kimchi-Schwartz, L Martin, E Flurin, C Aron, M Kulkarni, HE Tureci, and I Siddiqi. Stabilizing entanglement via symmetry-selective bath engineering in superconducting qubits. *Physical Review Letters*, 116(24):240503, 2016.

[64] Nissim Ofek, Andrei Petrenko, Reinier Heeres, Philip Reinhold, Zaki Leghtas, Brian Vlastakis, Yehan Liu, Luigi Frunzio, SM Girvin, Liang Jiang, et al. Extending the lifetime of a quantum bit with error correction in superconducting circuits. *Nature*, 536(7617):441–445, 2016.

[65] Eliot Kapit. Hardware-efficient and fully autonomous quantum error correction in superconducting circuits. *Physical Review Letters*, 116(15):150501, 2016.

[66] Yehan Liu, Shyam Shankar, Nissim Ofek, Michael Hatridge, Anirudh Narla, KM Sliwa, Luigi Frunzio, Robert J Schoelkopf, and Michel H Devoret. Comparing and combining measurement-based and driven-dissipative entanglement stabilization. *Physical Review X*, 6(1):011022, 2016.

[67] Ruichao Ma, Brendan Saxberg, Clai Owens, Nelson Leung, Yao Lu, Jonathan Simon, and David I Schuster. A dissipatively stabilized mott insulator of photons. *Nature*, 566(7742):51–57, 2019.

[68] Alicia J Kollár, Mattias Fitzpatrick, and Andrew A Houck. Hyperbolic lattices in circuit quantum electrodynamics. *Nature*, 571(7763):45–50, 2019.

[69] Matteo Biondi, Gianni Blatter, and Sebastian Schmidt. Emergent light crystal from frustration and pump engineering. *Physical Review B*, 98(10):104204, 2018.

[70] M Hafezi, P Adhikari, and JM Taylor. Chemical potential for light by parametric coupling. *Physical Review B*, 92(17):174305, 2015.

[71] John Clarke and Alex I Braginski. *The SQUID handbook: Applications of SQUIDs and SQUID systems*. John Wiley & Sons, 2006.

[72] Edward L Wolf, Gerald B Arnold, Michael A Gurvitch, and John F Zasadzinski. *Josephson Junctions: History, Devices, and Applications*. CRC Press, 2017.

[73] BD Joesphson. Possible new effects in superconductive tunneling. *Phys. Lett*, 1(7):251, 1962.

[74] Steven M Girvin. Circuit qed: superconducting qubits coupled to microwave photons. *Quantum machines: measurement and control of engineered quantum systems*, 113:2, 2011.

[75] John Kerr. Xl. a new relation between electricity and light: Dielectrified media birefringent. *The London, Edinburgh, and Dublin Philosophical Magazine and Journal of Science*, 50(332):337–348, 1875.

[76] John Kerr. Liv. a new relation between electricity and light: Dielectrified media birefringent (second paper). *The London, Edinburgh, and Dublin Philosophical Magazine and Journal of Science*, 50(333):446–458, 1875.

[77] GJ Dolan. Offset masks for lift-off photoprocessing. *Applied Physics Letters*, 31(5):337–339, 1977.

[78] Wikipedia contributors. Parametric oscillator.

[79] Ananda Roy and Michel Devoret. Introduction to parametric amplification of quantum signals with josephson circuits. *Comptes Rendus Physique*, 17(7):740–755, 2016.

[80] Baleegh Abdo, Archana Kamal, and Michel Devoret. Nondegenerate three-wave mixing with the josephson ring modulator. *Physical Review B*, 87(1):014508, 2013.

[81] T-C Chien, O Lanes, C Liu, X Cao, P Lu, S Motz, G Liu, D Pekker, and M Hatridge. Multiparametric amplification and qubit measurement with a kerr-free josephson ring modulator. *Physical Review A*, 101(4):042336, 2020.

[82] Chenxu Liu, Tzu-Chiao Chien, Michael Hatridge, and David Pekker. Optimizing josephson-ring-modulator-based josephson parametric amplifiers via full hamiltonian control. *Physical Review A*, 101(4):042323, 2020.

[83] Flavius Dietrich Octavian Schackert. *A practical quantum-limited parametric amplifier based on the Josephson ring modulator*. Yale University, 2013.

[84] N. Bergeal, F. Schackert, M. Metcalfe, R. Vijay, V. E. Manucharyan, L. Frunzio, D. E. Prober, R. J. Schoelkopf, S. M. Girvin, and M. H. Devoret. Phase-preserving amplification near the quantum limit with a Josephson ring modulator. *Nature*, 465(7294):64–68, 2010.

[85] N. Bergeal, R. Vijay, V. E. Manucharyan, I. Siddiqi, R. J. Schoelkopf, S. M. Girvin, and M. H. Devoret. Analog information processing at the quantum limit with a Josephson ring modulator. *Nature Physics*, 6(4):296–302, 2010.

[86] Crispin Gardiner, Peter Zoller, and Peter Zoller. *Quantum noise: a handbook of Markovian and non-Markovian quantum stochastic methods with applications to quantum optics*. Springer Science & Business Media, 2004.

[87] Katrina Sliwa. *Improving the quality of Heisenberg back-action of qubit measurements made with parametric amplifiers*. Yale University, 2016.

[88] N. E. Frattini, U. Vool, S. Shankar, A. Narla, K. M. Sliwa, and M. H. Devoret. 3-wave mixing Josephson dipole element. *Applied Physics Letters*, 110(22):1–5, 2017.

[89] Gangqiang Liu, T-C Chien, X Cao, Olivia Lanes, Edan Alpern, D Pekker, and M Hatridge. Josephson parametric converter saturation and higher order effects. *Applied Physics Letters*, 111(20):202603, 2017.

[90] Aashish A Clerk, Michel H Devoret, Steven M Girvin, Florian Marquardt, and Robert J Schoelkopf. Introduction to quantum noise, measurement, and amplification. *Reviews of Modern Physics*, 82(2):1155, 2010.

[91] Carlton M. Caves. Quantum-mechanical noise in an interferometer. *Physical Review D*, 23(8):1693–1708, 1981.

[92] Carlton M Caves and Bonny L Schumaker. New formalism for two-photon quantum optics. i. quadrature phases and squeezed states. *Physical Review A*, 31(5):3068, 1985.

[93] Bonny L Schumaker and Carlton M Caves. New formalism for two-photon quantum optics. ii. mathematical foundation and compact notation. *Physical Review A*, 31(5):3093, 1985.

[94] Christopher C. Gerry. Two-mode squeezed pair coherent states. *Journal of Modern Optics*, 42(3):585–606, 1995.

[95] R. Loudon and P. L. Knight. Squeezed Light. *Journal of Modern Optics*, 34(6-7):709–759, 1987.

[96] Christopher Eichler and Andreas Wallraff. Controlling the dynamic range of a josephson parametric amplifier. *EPJ Quantum Technology*, 1(1):2, 2014.

[97] N. Bergeal, F. Schackert, L. Frunzio, and M. H. Devoret. Two-mode correlation of microwave quantum noise generated by parametric down-conversion. *Physical Review Letters*, 108(12):1–5, 2012.

[98] E. Flurin, N. Roch, F. Mallet, M. H. Devoret, and B. Huard. Generating Entangled Microwave Radiation Over Two Transmission Lines. *Physical Review Letters*, 109(18):1–5, 2012.

[99] Sh Barzanjeh, D. P. Divincenzo, and B. M. Terhal. Dispersive qubit measurement by interferometry with parametric amplifiers. *Physical Review B - Condensed Matter and Materials Physics*, 90(13), 2014.

[100] NE Frattini, U Vool, S Shankar, A Narla, KM Sliwa, and MH Devoret. 3-wave mixing josephson dipole element. *Applied Physics Letters*, 110(22):222603, 2017.

[101] VV Sivak, NE Frattini, VR Joshi, A Lingenfelter, S Shankar, and MH Devoret. Kerr-free three-wave mixing in superconducting quantum circuits. *Physical Review Applied*, 11(5):054060, 2019.

[102] Emmanuel Flurin. *The Josephson mixer: a Swiss army knife for microwave quantum optics*. PhD thesis, Ecole normale supérieure-ENS PARIS, 2014.

[103] Baleegh Abdo, Katrina Sliwa, S Shankar, Michael Hatridge, Luigi Frunzio, Robert Schoelkopf, and Michel Devoret. Josephson directional amplifier for quantum measurement of superconducting circuits. *Physical Review Letters*, 112(16):167701, 2014.

[104] KM Sliwa, M Hatridge, A Narla, S Shankar, L Frunzio, RJ Schoelkopf, and MH Devoret. Reconfigurable josephson circulator/directional amplifier. *Physical Review X*, 5(4):041020, 2015.

[105] Alexander Grimm, Nicholas E Frattini, Shruti Puri, Shantanu O Mundhada, Steven Touzard, Mazyar Mirrahimi, Steven M Girvin, Shyam Shankar, and Michel H Devoret. The kerr-cat qubit: stabilization, readout, and gates. *arXiv preprint arXiv:1907.12131*, 2019.

[106] Alexander N Korotkov. Quantum bayesian approach to circuit qed measurement with moderate bandwidth. *Physical Review A*, 94(4):042326, 2016.

[107] Bernard Yurke, Samuel L. McCall, and John R Klauder. SU(2) and SU(1,1) interferometers. *Physical Review A*, 33(6):4033–4054, 1986.

[108] Nicolas Roch, Mollie E Schwartz, Felix Motzoi, Christopher Macklin, Rajamani Vijay, Andrew W Eddins, Alexander N Korotkov, K Birgitta Whaley, Mohan Sarovar, and Irfan Siddiqi. Observation of measurement-induced entanglement and quantum trajectories of remote superconducting qubits. *Physical Review Letters*, 112(17):170501, 2014.

[109] Andreas Wallraff, David I Schuster, Alexandre Blais, Luigi Frunzio, R-S Huang, Johannes Majer, Sameer Kumar, Steven M Girvin, and Robert J Schoelkopf. Strong coupling of a single photon to a superconducting qubit using circuit quantum electrodynamics. *Nature*, 431(7005):162–167, 2004.

[110] Theodore Walter, Philipp Kurpiers, Simone Gasparinetti, Paul Magnard, Anton Potočnik, Yves Salathé, Marek Pechal, Mintu Mondal, Markus Oppliger, Christopher Eichler, et al. Rapid high-fidelity single-shot dispersive readout of superconducting qubits. *Physical Review Applied*, 7(5):054020, 2017.

[111] Johannes Heinsoo, Christian Kraglund Andersen, Ants Remm, Sebastian Krinner, Theodore Walter, Yves Salathé, Simone Gasparinetti, Jean-Claude Besse, Anton Potočnik, Andreas Wallraff, et al. Rapid high-fidelity multiplexed readout of superconducting qubits. *Physical Review Applied*, 10(3):034040, 2018.

[112] Alexander N. Korotkov. Quantum bayesian approach to circuit qed measurement with moderate bandwidth. *Phys. Rev. A*, 94:042326, Oct 2016.

[113] KW Murch, SJ Weber, Christopher Macklin, and Irfan Siddiqi. Observing single quantum trajectories of a superconducting quantum bit. *Nature*, 502(7470):211–214, 2013.

[114] S. Shankar, M. Hatridge, Z. Leghtas, K. M. Sliwa, A. Narla, U. Vool, S. M. Girvin, L. Frunzio, M. Mirrahimi, and M. H. Devoret. Autonomously stabilized entanglement between two superconducting quantum bits. *Nature*, 504(7480):419–422, 2013.

[115] Matti Silveri, Evan Zalys-Geller, Michael Hatridge, Zaki Leghtas, Michel H. Devoret, and S. M. Girvin. Theory of remote entanglement via quantum-limited phase-preserving amplification. *Physical Review A*, 93(6):1–10, 2016.

[116] Christian Dickel, JJ Wesdorp, NK Langford, S Peiter, Ramiro Sagastizabal, Alessandro Bruno, Ben Criger, F Motzoi, and L DiCarlo. Chip-to-chip entanglement of transmon qubits using engineered measurement fields. *Physical Review B*, 97(6):064508, 2018.

[117] Alicia J Kollár, Mattias Fitzpatrick, Peter Sarnak, and Andrew A Houck. Line-graph lattices: Euclidean and non-euclidean flat bands, and implementations in circuit quantum electrodynamics. *Communications in Mathematical Physics*, pages 1–48, 2019.

[118] Tanay Roy, Suman Kundu, Madhavi Chand, Sumeru Hazra, N Nehra, R Cosmic, A Ranadive, Meghan P Patankar, Kedar Damle, and R Vijay. Implementation of pairwise longitudinal coupling in a three-qubit superconducting circuit. *Physical Review Applied*, 7(5):054025, 2017.

[119] Tanay Roy, Sumeru Hazra, Suman Kundu, Madhavi Chand, Meghan P Patankar, and R Vijay. A programmable three-qubit superconducting processor with all-to-all connectivity. *arXiv preprint arXiv:1809.00668*, 2018.

[120] Tzu-Chiao Chien. *Creating directional quantum-limited amplification using multiple parametric drives*. PhD thesis, University of Pittsburgh, 2020.

[121] Paul R Berman and Vladimir S Malinovsky. *Principles of laser spectroscopy and quantum optics*. Princeton University Press, 2011.

[122] Simon E Nigg, Hanhee Paik, Brian Vlastakis, Gerhard Kirchmair, Shyam Shankar, Luigi Frunzio, MH Devoret, RJ Schoelkopf, and SM Girvin. Black-box superconducting circuit quantization. *Physical Review Letters*, 108(24):240502, 2012.

[123] Ronald M Foster. A reactance theorem. *Bell System Technical Journal*, 3(2):259–267, 1924.

[124] Zlatko K Minev, Zaki Leghtas, Shantanu O Mundhada, Lysander Christakis, Ioan M Pop, and Michel H Devoret. Energy-participation quantization of josephson circuits. *arXiv preprint arXiv:2010.00620*, 2020.

[125] Firat Solgun, David P DiVincenzo, and Jay M Gambetta. Simple impedance response formulas for the dispersive interaction rates in the effective hamiltonians of low anharmonicity superconducting qubits. *IEEE transactions on microwave theory and techniques*, 67(3):928–948, 2019.

[126] Nicholas T Bronn, Yanbing Liu, Jared B Hertzberg, Antonio D Córcoles, Andrew A Houck, Jay M Gambetta, and Jerry M Chow. Broadband filters for abatement of spontaneous emission in circuit quantum electrodynamics. *Applied Physics Letters*, 107(17):172601, 2015.

[127] Yanbing Liu and Andrew A Houck. Quantum electrodynamics near a photonic bandgap. *Nature Physics*, 13(1):48–52, 2017.

[128] Nicholas A Masluk, Ioan M Pop, Archana Kamal, Zlatko K Minev, and Michel H Devoret. Microwave characterization of josephson junction arrays: Implementing a low loss superinductance. *Physical Review Letters*, 109(13):137002, 2012.

[129] Pinlei Lu, Saeed Khan, Tzu-Chiao Chien, Xi Cao, Olivia T Lanes, Chao Zhou, Hakan E Türeci, and Michael J Hatridge. Nearly quantum-limited josephson-junction frequency comb synthesizer. *arXiv preprint arXiv:2005.10193*, 2020.

[130] Christopher Axline, Matthew Reagor, R Heeres, Philip Reinhold, Chen Wang, Kevin Shain, Wolfgang Pfaff, Yiwen Chu, Luigi Frunzio, and Robert J Schoelkopf. An architecture for integrating planar and 3d cqed devices. *Applied Physics Letters*, 109(4):042601, 2016.

[131] Matthew Reagor, Hanhee Paik, Gianluigi Catelani, Luyan Sun, Christopher Axline, Eric Holland, Ioan M Pop, Nicholas A Masluk, Teresa Brecht, Luigi Frunzio, et al.

Reaching 10 ms single photon lifetimes for superconducting aluminum cavities. *Applied Physics Letters*, 102(19):192604, 2013.

[132] Luke D Burkhart, James Teoh, Yaxing Zhang, Christopher J Axline, Luigi Frunzio, MH Devoret, Liang Jiang, SM Girvin, and RJ Schoelkopf. Error-detected state transfer and entanglement in a superconducting quantum network. *arXiv preprint arXiv:2004.06168*, 2020.

[133] Yaxing Zhang, Brian J Lester, Yvonne Y Gao, Liang Jiang, RJ Schoelkopf, and SM Girvin. Engineering bilinear mode coupling in circuit qed: Theory and experiment. *Physical Review A*, 99(1):012314, 2019.

[134] E Zalys-Geller, A Narla, S Shankar, M Hatridge, MP Silveri, K Sliwa, Z Leghtas, and MH Devoret. Generation of discord through a remote joint continuous variable measurement. *arXiv preprint arXiv:1803.01275*, 2018.

[135] Teresa Brecht, Matthew Reagor, Yiwen Chu, Wolfgang Pfaff, Chen Wang, Luigi Frunzio, Michel H Devoret, and Robert J Schoelkopf. Demonstration of superconducting micromachined cavities. *Applied Physics Letters*, 107(19):192603, 2015.